STRUCTURE IN THE 557.7nm OXYGEN AIRGLOW

A Thesis for the degree of Doctor of Philosophy

in the University of Adelaide

submitted by

John Terence Freund B.Sc. (Hons)

The Mawson Institute for Antarctic Research

March 1976

CONTENTS

SUMMARY

An image intensifier-film system and a 4-field-of-view photometer, constructed in the Mawson Institute for Antarctic Research, were used in the observation of the λ 557.7nm atomic oxygen emission in the night airglow.

Details of the construction of the image intensifier-film system are provided along with examples of the sky pictures of the 557.7nm and 630nm airglow intensity observed with this system. It was found that in its present form, this sytem is not suitable for the direct visual observation of detail in the airglow because of spatial transmission variations within the filters and gain variations within the image intensifier. However it is shown that with relatively minor modification, which includes the optimisation of the filter-optics combination and ensuring that a good proportion and a sufficient number of the photo-electrons are recorded within a sky picture, the system is capable of providing parameters relating to the dynamic variations in the airglow intensity of the type observed with the 4-field photometer. These parameters include the drift velocity and spatial spectra of the airglow variations.

With respect to the 4-field-of-view photometer which sequentially observes the airglow at four closely spaced circular areas, parameters which must be considered in designing such an instrument are derived or inferred. An outline of the design of the present 4-field photometer is provided and details of the method of calculation of the drift velocity and power spectra from the six nights of observation on the 557.7nm airglow are included.

The following characteristics were observed and assertions made with respect to the 4-field photometer results. Typically a decrease in spectral power occured at frequencies near 4×10^{-3} Hz with little spectral

power at higher frequencies although on one night substantial spectral power extended to 10^{-2} Hz. The drift velocities on most nights exhibited a marked degree of anisotropy with little correlation existing between the drift velocities and the background wind velocities. The intensity variations included wave-like structure periodic over several cycles at periods less than 15 minutes and the presence of longer period waves was also noted. It was concluded that the major component of the intensity variations were caused be internal gravity waves. It was assessed that the gravity waves observed were dissipating energy into the atmosphere at a rate of at least 10^{-7} watts-m^{-3} if they were in a state approximating zero amplitude growth. By considering the direction of the drift velocities and the frequency of the longer period waves, there was evidence that cold fronts were a possible source for the gravity waves observed.

This thesis contains no material which has been accepted for the award of any other degree or diploma in any University and, to the best of the author's knowledge and belief, it contains no material previously published or written by another person, except when due reference is made in the text.

(J.T. Freund)

ACKNOWLEDGEMENTS

The author is greatly appreciative of the support and cooperation received from the personnel of the Mawson Institute for Antarctic Research, and is particularly indebted to Dr F. Jacka, Director of the Mawson Institute for his understanding, constant encouragement and guidance given in his supervision of the project. Much credit is due to Dr F. Jacka for the initiation of the projects and for much of the optical and mechanical design. Similarly to Dr P. Seymour for his constructive criticism of a draft of this thesis and his aid with some mathematics, particularly in Appendix B.

Mr D. Creightion was responsible for much of the mechanical and electrical design of the image-intensifier system and assisted with much of the electronic design. His advice on many aspects of the work was of immeasurable value. The provision of data concerning winds obtained by measuring the Doppler Shift of the 557.7nm oxygen airglow by Dr A. Bower and Dr P. Wilksh is acknowledged. The mechanical construction work was carried out by Mr P. Hull, Mr F. Koltai and Mr F. Fone and their cheerful assistance with many technical problems is also acknowledged.

The author is grateful to Mrs B.M. Geary for typing this thesis and to Mrs E. Sawyer for her assistance with the diagrams. Finally this would not be complete without thanking his wife Margaret for her encouragement and patience.

CHAPTER 1

THE USE OF THE [OI] λ 557.7nm NIGHT AIRGLOW FOR THE MEASUREMENT OF CERTAIN DYNAMICAL PROPERTIES OF THE NEUTRAL ATMOSPHERE

1.1 Introduction

Hines (1965) commented that airglow observations may be useful in determining certain dynamical characteristics in the upper atmosphere. Sears (1973) noted that for a thin emitting layer, the statistical analysis of the intensity variations from three closely spaced fields or areas of sky allows the determination of their size and drift velocities in the atmosphere. Sears and Evans (1974) have already reported on observations with a three field of view photometer carried out at Chatanika, Alaska in 1972 where the intensity variations, which were most likely auroral induced phenomena, appeared to be attributable to the superposition of waves with periods ranging from 10 to 100 seconds. This chapter will initially be concerned with a discussion of the green oxygen line with respect to midlatitudes where the relative thinless of its vertical emission profile and seeming dependence only on neutral atmospheric parameters make it ideal for a study of certain dynamical properties of the atmosphere. A review of previous work on this emission line and also an outline of possible experimental techniques will also be included.

1.2.1 [OI] λ 557.7nm Mechanism

The forbidden line of atomic oxygen at λ 557.7nm results from the transition from the 1S energy level to the 1D energy level as described in equation (1.1)

$$O(1S) \rightarrow O(1D) + \lambda\ 557.7nm \qquad (1.1)$$

where the probability of this reaction is 1.28 sec^{-1}.

This emission arises in two separate regions, one in the F-region, with the other from around a height of 100 km tending to dominate the higher altitude component in midlatitudes. Chiplonkar and Tillu (1970) report from observations taken at Poona that by calculating the average van Rhijn ratios, the two components of intensity have a ratio varying around 2 : 1.

The E-region emission component is usually attributed to the Chapman reaction although some authors have proposed that a significant contribution may result from other reactions. (Hendricksen, 1973.)

The Chapman reaction is

$$O(3P) + O(3P) + O(3P) \rightarrow O_2^* + O(1S) \ . \qquad (1.2)$$

Taking into account the possibility of quenching of O[1S] by some species M_i and neglecting the transition $1S \rightarrow 3P$, one obtains Q, the volume emission rate resulting from the Chapman Reaction.

$$Q = \frac{k_1[O(3P)]^3}{1 + \sum_{i=1}^{3} q_i[M_i]/A} \qquad (1.3)$$

where k_1 is the reaction rate of equation (1.2), M_i is the number density of the quenching species N_2, O_2, O(3P) having respective quenching coefficients q_i and A is the probability for the transition of O(1S) to lower levels and has a value of 1.36 sec^{-1} according to Garstang (1951).

Barth and Hilderbrant (1961) proposed that the airglow excitation was also produced by a variation of the Chapman Reaction involving a precursor in the form of excited molecular oxygen:-

$$O(3P) + O(3P) + O(3P) \rightarrow O_2^* + O(3P) \qquad (1.4)$$

$$O_2^* + O(3P) \rightarrow O_2 + O(1S) \ . \qquad (1.5)$$

However neither laboratory nor theoretical studies have confirmed the existence of any such precursor. (Donohue et al 1973.) Qualitative arguments against any other of the mechanisms described by Hendricksen will be presented in the next section.

1.2.2 Vertical Profile of 557.7nm Emission

This section will be restricted to comparing a profile deduced from equation (1.3) using recent density and rate co-efficients and that obtained in a rocket flight in mid-latitudes. In an attempt to measure atomic oxygen profiles, Offerman and Drescher (1973) obtained a 557.7nm volume emission rate profile during a rocket flight from Sardinia and this is shown in Figure 1.1. Using $k_1 = 4.8 \times 10^{-33} cm^6/sec$ as proposed by Schiff (1972), quenching co-efficients for q_2 and q_3 as deduced by Slanger and Black (1973) and Jacchia's (1973) model of the O(3P) and O_2 density profiles in equation (1.3) one arrives at a volume emmission rate profile resulting from the Chapman reaction with allowances for quenching. From this profile the integrated emission rate in the 90 → 100 km region is over 2000 Rayleighs and in Figure 1.1 purely to aid comparison, this profile has been modified to the extent that the integrated emission rate is set equal to that obtained from the Offerman and Drescher profile. Equality of the integrated emission rate may be obtained by setting $k_1 = 10^{-34} cm^6/sec$. Alternatively Jacchia (1971) may over-estimate atomic oxygen densities and the other parameters may contain discrepancies. Slanger and Black (1973) are of the opinion that the kinetic co-efficients are not sufficiently refined to produce reliable O(3P) vertical profiles from 557.7nm airglow measurements.

Of interest is the thinness of the layer and a way of quantitatively

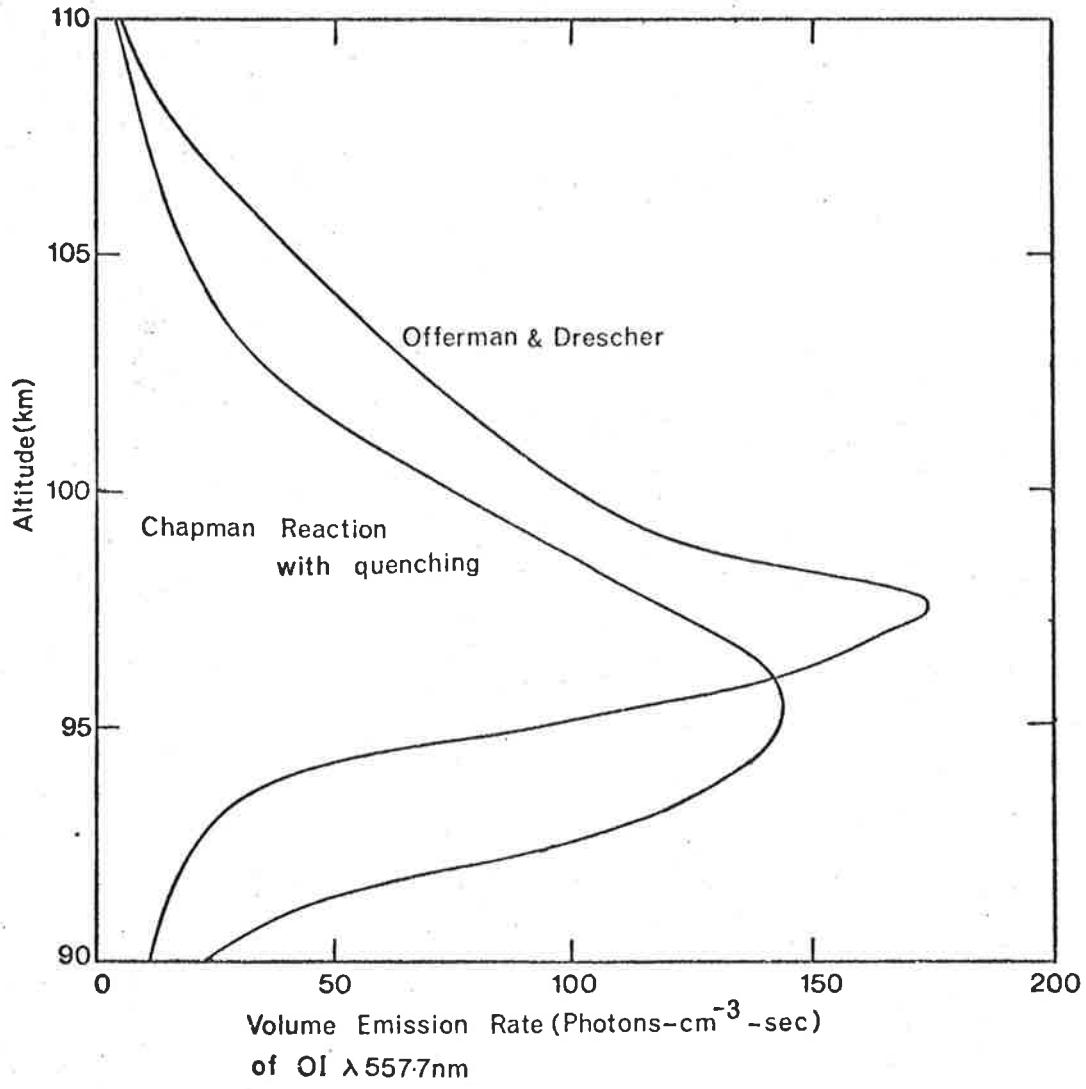

Figure 1.1 Altitude profiles of the volume emission rate of [OI] λ 557.7 nm obtained by Offerman & Drescher [1973] and determined from the Chapman Reaction with quenching using $k_1=10^{-34}$ cm^6 -sec^{-1}, Jacchia's [1971] model of the O [3p] and O_2 density profiles and the quenching co-efficients of Slanger and Black [1972].

defining it is in terms of a half-width $I_{\frac{1}{2}}$, where $I_{\frac{1}{2}}$ is the vertical width in which 50% of the total emission of the airglow layer is confined. The value of $I_{\frac{1}{2}}$ for the Offerman-Drescher (1973) profile is 5 km and for the profile resulting from the Chapman Reaction with quenching, $I_{\frac{1}{2}}$ is 7 km. In all future discussions the layer will be considered to have a vertical half thickness of 6 km.

1.2.3 The Density Sensitivity of 557.7nm Emission

Short period fluctuations excepting those experiencing severe thermal dissipation will be nearly adiabatic requiring that density or pressure fluctuations be accompanied by temperature fluctuations. However as the temperature dependence of k_1 is not known and the dependence on temperature of the quenching co-efficients is not large when only small temperature variations are considered (Slanger and Black 1973), the effect of temperature will be ignored.

For some perturbation $\Delta\rho$ in density ρ, Q as defined in equation (1.3) would be related to ρ by:-

$$\frac{\Delta Q}{Q} = n \frac{\Delta \rho}{\rho} \tag{1.6}$$

where ΔQ represents the intensity change produced by the density perturbation and n, defined by the above equation, can be calculated from equation (1.3) and is

$$n = 3 - \frac{1}{1+A/\sum_{i=1}^{3} q_i [M_i]} . \tag{1.7}$$

From equation (1.7) it is apparent that n has limits of 2 and 3 depending on the quenching co-efficients and the densities of atomic and molecular oxygen and therefore will be height dependent. This equation

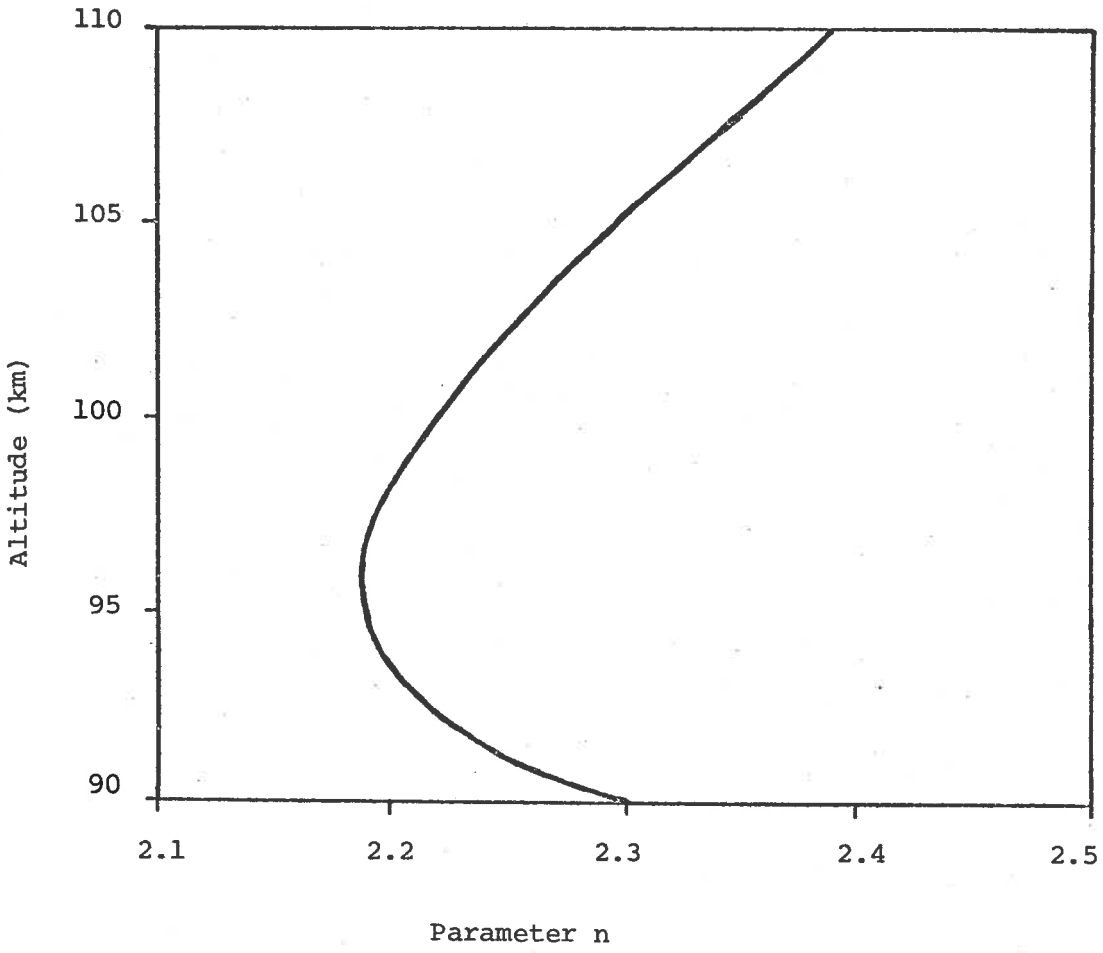

Figure 1.2 Vertical profile of the parameter n (defined by equation 1.7) using the quenching co-efficients of Slanger and Black (1973) and the Jacchia (1971) O_2 and O(3P) density profiles.

is used to construct Figure 1.2 using the quenching rate co-efficients of Slanger and Black (1973) and Jacchia's (1971) density model. In this figure n has a minimum value of 2.185 at 96 km and the value on n when the 90-110 km layer is considered is 2.234.

A consequence of this dependence of n on height is that if a uniform relative density perturbation occurs at levels throughout the layer, then the relative change in the volume emission rate will vary with n as described in equation (1.7). This effect would result in ΔQ having larger values at the edges of the layer in comparison to ΔQ at the centre of the layer thus effectively making the layer appear vertically broader when subjected to density changes than the vertical emission in Figure 1.1 suggests. The magnitude of this "broadening" on $I_{\frac{1}{2}}$ can be shown to be only 0.2 km → 0.3 km and thus its effect on the layer thickness is marginal.

Finally the volume emission rate profile of Offerman and Drescher in Figure 1.1 appears to indicate a larger value of the power index n of atomic oxygen density than that for the Chapman Reaction with quenching. Hence from all suggested mechanisms for 557.7nm emission from this layer as outlined by Hendricksen (1973) only the Chapman Reaction and the Barth Reaction can be taken seriously as major contributers to the 557.7nm line from the E-region since the other reactions would give rise to broader volume emission rate profiles due to values of n less than 2.

1.3.1 A Review of Some 557.7nm Studies

Studies of 557.7nm night glow have been central in many observational programs, but many of the fluctuations observed in space and time have yet to be fully explained. Roach et al (1958) obtained values for the speed of drift of the isophotes in their study of airglow-cell movement where they noted the existance of large cellular patterns of scale sizes of

around 2500 km. They found that this isophote drift velocity had an average velocity of 93 m/s and from consideration of the scale size of this irregularity or cell, they concluded that the velocities were that of the background wind. Danekar (1965) also arrived at very similar results. Baltanar and Pardo (1972) found no correlation of any characteristics of these cells with the Kp index although a cell with a northward motion was noted when Kp was 7^+ in contradiction to the usual southward motion which had been noted by Roach et al (1958). Of 7 cellular type structures observed at Mt. Torrens during 1968-1969 five showed no detectable component of the velocity in the North-South direction while the other two appeared to be moving towards the North. An example of this cellular structure observed at Mt. Torrens is given in Figure 1.3 where the variation of intensity with time at three different zenith angles along a North-South axis is shown. The average northerly velocity in the example shown is 87.5 m/s.

On a global scale Roach et al (1967), reporting on the median intensity of 557.7nm as a function of magnetic latitude, found a small peak in median intensity in mid-latitudes and also that the median intensity has a large semi-annular variation of these latitudes.

Korobeynikova and Nasirov (1972) report that patches in the 557.7nm morphology may vary in a rapidly pulsating manner with periods of the order of 5 minutes. They also found that the lunar tide affects intensity such that an amplitude of 35 Rayleighs occurs 4 hours 10 minutes after local midnight and the existence of a correlation between 557.7nm intensity and sporadic E. Barat et al (1972) have also reported the presence of short period intensity fluctuations with periods of 3-5 minutes and by viewing two fields of view it was found they originated in a region near 96 km and also there was a lag in time in the structure when there existed a spatial distance of several

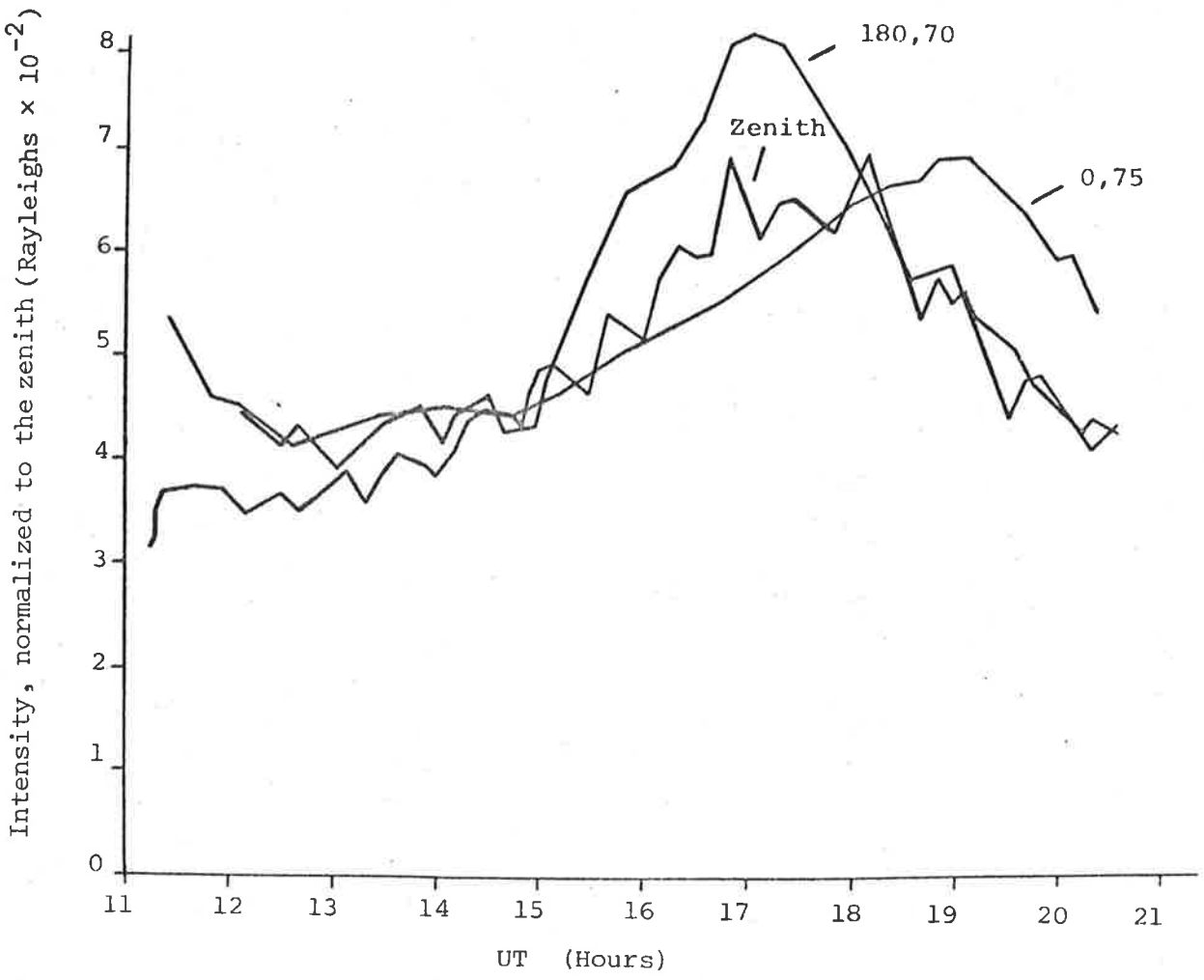

Figure 1.3 Plot of λ557.7 [OI] intensities observed on 29 April 1969 at Mt Torrens for 3 different positions in a North-South plane. 180,70 refers to a point of observation of 180° azimuth angle and 70° zenith angle. The structure exhibits a cellular structure estimated to be moving northwards with a velocity of 87.5 $m\text{-}s^{-1}$.

kilometers between the two fields of view at 96 km.

By examining the spectroscopic details of the 557.7nm line it is possible to calculate the neutral wind velocity from the Doppler shift and the temperature at the neutral gas at the height of the airglow layer from the Doppler broadening. Armstrong (1968) reviews the studies which have been carried out and reports on temperature measurements of 150° K to greater than 210° K. However very few wind measurements have been reported. Bower and Wilksch (1974) have succeeded in finding values for the neutral winds and comments on their results will be found in Chapter 4. Temperature measurements by the above mentioned workers have been found to fluctuate by up to 100° K on the same night although this may be due to contamination by the F-region component of 557.7nm emission.

1.3.2 The Analysis of Moving Patterns in Geophysics

As will become apparent in the discussion on the 4-field photometer results the method of analysis must be tailored to suit the nature of the fluctuations being observed. However a brief review of techniques outlined by Briggs (1968) will serve as a convenient launching platform. Briggs comments that methods used for the determination of the drift velocities of ionsospheric irregularities may have parallel applications to "moving patterns of light emissions from the night sky".

The two basic techniques are that one may observe at several spaced points and monitor temporal changes in the signal or alternatively a spatial picture of the pattern is obtained at successive intervals of time. By correlation techniques, in the first case a "time shift" may be determined and in the second case a "space shift". In a spatial one dimensional case a "space time" correlation function $\rho(\xi,\tau)$ may be computed, where the two patterns are separated in space by ξ and in time

by τ . Briggs assumed that the contours $\rho(\xi,\tau)$ = constant are in the form of concentric ellipses and in the frame of reference of the observer, $\rho(\xi,\tau)$ will be in the form

$$\rho(\xi,\tau) = f\left[(\xi-v\tau)^2 + \frac{\tau^2 d^2}{b^2}\right] \tag{1.8}$$

where d is a "characteristic length", and b a "characteristic time". More generally, equation (1.8) can be written in the form:-

$$\rho(\xi,\tau) = f\left[(\xi-v\tau)^2+g(\tau^2)\right] \tag{1.9}$$

where the function $g(\tau^2)$ is a measure of changes with time in the pattern.

In the first case if the pattern is observed temporally at two points separated by a fixed distance ξ_0, the two records can be cross-correlated to give the function $\rho(\xi_0,\tau)$ and its maximum will be defined by $\frac{\partial\rho}{\partial\tau} = 0$ at some time lag τ^1 and from equation (1.8)

$$\tau^1 = \frac{\xi_0 v}{v^2+d^2/b^2} . \tag{1.10}$$

Hence to find the true velocity v of the pattern a knowledge of changes in the pattern with respect to time are required.

In the second case where two "snapshots" of the pattern are separated by a time interval τ_0, one obtains the function $\rho(\xi,\tau_0)$ by cross-correlating the two frames and the condition $\frac{\sigma\rho}{\sigma\xi} = 0$ is used to find its maximum value for some space shift ξ^1 and gives:-

$$\xi^1 = v\tau_0 . \tag{1.11}$$

It appears that the second method is superior in that no assumptions about the nature of changes in the pattern are required and in fact it also offers a method for gathering information concerning $g(\tau_0^2)$ since

$$\rho(\xi^1,\tau_0) = f(g(\tau_0^2)) . \tag{1.12}$$

In the 4-field photometer, temporal changes in the airglow are monitored at four regions. As this instrument provided the only significant results, only the technique concerned with obtaining the lag time between the temporal patterns at these four regions will be considered further within the thesis. However, the potential for the use of the spatial analysis technique on airglow patterns of the type observed will become apparent. Here, the Fourier Transform of the cross-correlation function of successive frames of the airglow pattern will provide the velocity of each spatial Fourier Component.

1.4 Summary

In section 1.3.1 the literature reveals the great diversity in 557.7nm airglow features ranging in time scales from semi-annual variations to periods of the order of minutes. Scale sizes of characteristics on a particular night vary from the large cellular structure to irregularity sizes corresponding to time variations of the order of minutes and must be representative of atmospheric features at this altitude of 96 km. The next chapter will describe an image intensifier system for airglow observation and later chapters will describe the development of a four-field of view photometer and its application to night glow studies.

CHAPTER 2

AN IMAGE INTENSIFIER SYSTEM AND ITS APPLICATION TO AIRGLOW STUDIES

2.1 Introduction

An image intensifier system was constructed to observe the morphology of the λ 557.7nm and 630nm nightglow. The system was constructed around an EMI type 9694 image intensifier tube and to reduce the dark current, a refrigeration system capable of maintaining the image intensifier tube temperature at -25°C was used. The output was recorded on 16mm film. This chapter provides details of the instrument, examples of night glow observations and some modifications to the system which would result in the system being useful for observing detail in the night glow such as that identified with internal gravity waves and travelling ionispheric disturbances.

2.2.1 Image Intensifier Tube

The main feature of the system was the EMI type 9694 image intensifier tube which is a magnetically-focussed four-stage phosphor-photocathode sandwich tube utilizing S20 photo cathodes and P11 phosphors. From the maker's data, the tube has a uniformity in gain of ±5%, a gain of 10^5 at 27 kV and of 10^6 at 36 kV, no background features visible on the output phosphor, a dark count rating of 500 counts/cm^2/sec and a resolution of 25 line-pairs/mm. Visually the resolution was assessed to be 15-20 line-pairs/mm over the central 25 mm region.

2.2.2 Optics

The optical system, illustrated in Figure 2.1, was provided with

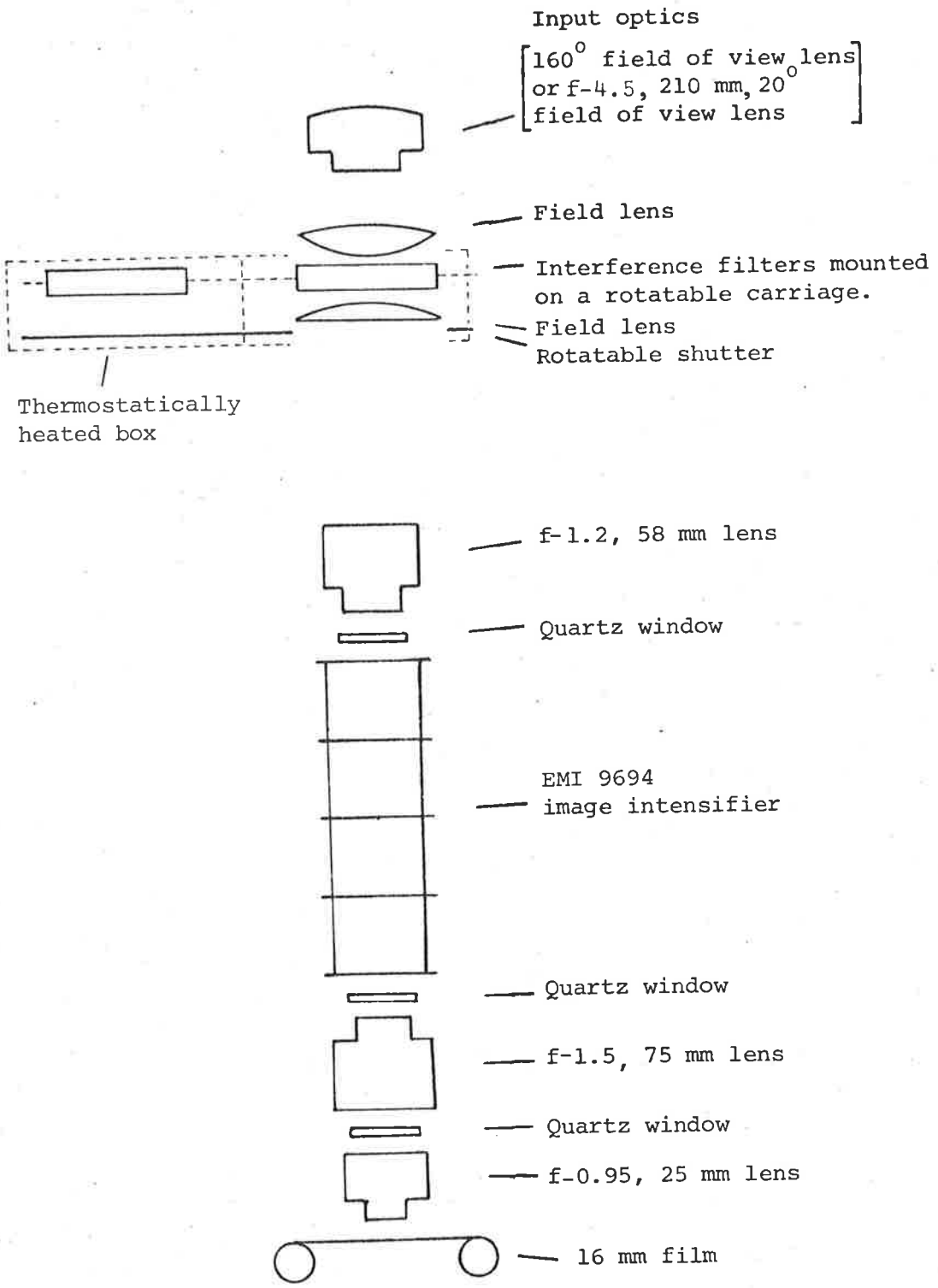

Figure 2.1 Schematic sketch of the image intensifier optical system.

two removable input systems, one a fish-eye or all-sky lens with a 160° field of view and the other a 20° field of view system which included as the objective a f-4.5, 210 mm focal length Schneider-Kreuznach Xenar lens. This latter system also included a mirror-periscope viewing arrangement with the zenith angle adjustable from 0° to 90° and the azimuth angle adjustable through 360°.

Each system was provided with a field lens situated above a common focal plane with an interference filter situated in the intervening space. Each cone of rays defining an image point was therefore focussed in such a way that the central ray of each cone was normal to the focal plane. This provided the smallest angular distribution of light rays through the interference filter. Initially a graticule was to be positioned at this focal plane but this was not done in the final form. The filters, mounted in a rotatable carriage with provision for four filters, a further field lens below the focal plane and a rotable shutter below this further field lens were contained within a thermostatically heated box. A f-1.2, 58 mm, Canon FL lens served as the objective lens to focus the image onto the photo-cathode. This lens was situated approximately 230mm below the focal plane adjacent to the filter and reduced the image size to 25.4mm. The upper optical system was focussed by adjusting the position of this lens and this could be carried out externally without the need to dismantle any components. Chromatic aberration in this optical system was compensated for by focussing the system at 630nm and placing a 3.5mm perspex plate adjacent the 557.7nm filter.

A f-1.5, 75mm Carl Zeiss Jena Bioter lens acted as a collimating lens at the output end of the image intensifier and a f-0.95 25mm Pierre Argenieux lens was used as a camera lens, therefore providing a three-times reduction in image size.

A periscope to view the image intensifier output included a front surface coated mirror which reflected the light through 90°, a f-2 55mm Gelios lens and a 22mm focal length 10X Olympus eye-piece. The periscope and the camera could be alternately moved into the viewing position.

The optical system also included 2mm thick quartz windows and these isolated the image intensifier tube and also the f-1.5 75mm lens.

2.2.3 Filters

The wavelength λ of the transmission peak of the optimum interference filter for an optical system such as the present one is (Eather and Reasoner, 1969)

$$\lambda \simeq \lambda_0 + \tfrac{1}{2}\,\delta\lambda_\theta \qquad (2.1)$$

where λ_0 is the wavelength of the emission line and $\delta\lambda_\theta$ is given by

$$\delta\lambda_\theta = \frac{\theta^2}{2\mu^{*2}}\,\lambda_0 \qquad (2.2)$$

with θ being the semi-angle of a cone of light rays at the filter and μ^* the effective refractive index of the central spaces layer for the filter. More generally $\delta\lambda_\theta$ is the negative wave length shift of the transmission peak of the filter for off-axis light-rays and λ_0 is the wave length of the transmission peak for rays normal to the filter.

This angle for the 20° field of view system was 6° and $\delta\lambda_{6^\circ}$ was $\sim$ 1.5nm. For both optical systems this angle could be reduced by reducing the aperture of the f-1.2 58mm focal length objective lens. Therefore it is possible to a certain extent to tailor the optics to suit

the filter although at the expense of the light intensity.

The original filters provided were single period with transmission peaks centred at 629.9nm and 557.7nm and having respective half-widths or bandwidths of 3.0nm and 2.6nm. The ratio of the transmission of the background light compared to the relevant airglow was high, due to the broad bandwidths of the filters and the fact that their transmission peak was not positioned according to equation (2.1). It was estimated that for the green filter, the background light contribution equalled the 557.7nm airglow component when the airglow intensity was 50 Rayleighs. Further these filters exhibited significant spatial variation of the wavelength of the transmission peak.

The filters used in the final system had the following specifications when tested at 30°C using an optical system with a 2° field of view - the wavelengths of the transmission peaks were at 630.45nm and 557.75nm and the wavelengths where the transmission profile was half the value of the peak transmission were 629.98, 630.97nm and 557.22, 558.32nm respectively. Due to edge deterioration in these filters only the central areas with respective diameters of 63mm and 67mm were used. The filters were operated at 35°C and the aperture of f-1.2, 58mm lens was set to f-1.5.

2.2.4 16mm Camera, Film

A camera for the present system was built in the Mawson Institute and was capable of taking 100 ft spools of 16mm film. Two solenoids were used to open and close the camera shutter and the film was also wound on during the latter operation. Control circuitry using 1 second and 10 second pulses from a crystal controlled electronic clock was constructed and exposure times of 1, 2, 4, 8, 16, 32 seconds and 1, 2, 4, 8, 16, 32 minutes were available.

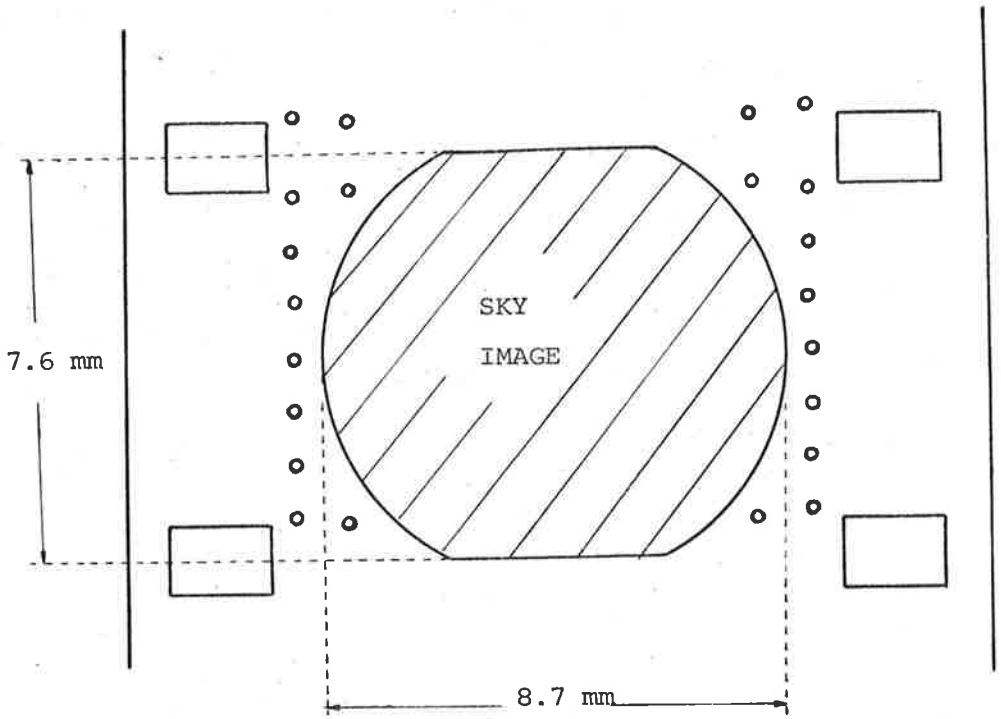

Figure 2.2 Sketch of an individual 16 mm film frame showing the position of the image and also the position of the coded signals which are represented by the small circles.

The camera was interfaced to the clock to provide coded time signals on the film with fibre optics and used to transmit light from miniature incandescent globes to the film surface. Figure 2.2 is a sketch of an individual film frame according to this system and indicates the dimension of the image at the film and also shows the position of the code marks. In addition to the code marks provided to indicate the hour and minute in a binary sense, four further code marks were used to indicate additional information such as the filter used and doubtful weather conditions.

The film used was Kodak 4-X Reversal Film and this film offers the properties of high speed, fine grain with a dense anti-halation layer between the emulsion and the film base. Its resolving power is superior to Plus-X negative film and equivalent to Plus-X reversal film.

It is possible to adjust the overall light gain of the system to suit the film characteristics by changing the gain of the image intensifier and also by adjusting the aperture setting of the camera lens. Maximising the contrast on the film for a given intensity change was the criterion used to establish the gain. This was carried out by positioning a density graduation chart calibrated in density steps of 0.2 in in the image plane adjacent to the filter. The EHT applied to the image intensifier tube was varied over a range of 26 kV to 33 kV for various settings of the aperture and the exposure times. Although one would expect the contrast to be similar when the combination of the intensifier gain and the aperture setting provide an equal gain at the film, nevertheless it was found that an EHT setting of 27 kV and an aperture setting of f-2.0 for the camera lens at an exposure time of 30 seconds provided the maximum contrast without repricocity failure of the film being evident. Increasing the gain through increasing the EHT by 2 to 3 kV however did not decrease the contrast to any appreciable degree.

The exposure times used for the airglow varied from 1-4 minutes depending upon the intensity of the emission line and the optical system used.

2.2.5 High Voltage Supply, Voltage Divider

A Brandenburg Model 905 power supply was used and this model provides an output current of up to 400 μA with the voltage continuously adjustable from 6 kV to 60 kV. According to the makers specifications the output voltage ripple is 100 v peak to peak and the regulation for zero to full load is better than 0.25% at full voltage.

A voltage divider necessary to supply the correct potentials to the 13 dynodes of the image intensifier was built in the Mawson Institute using the resistance values recommended by EMI. The voltage applied to the 3 intermediate phosphor-cathode dynodes could be varied by up to ±3% in three switched steps of 1.5% plus 1.5% continuous fine adjustment.

2.2.6 Focussing Solenoid, Solenoid Current Supply

The solenoid, supplied by EMI, included helical water-cooling tubes cast in epoxy resin running along the inside of the solenoid. The solenoid had a room temperature resistance of 11 ohms and produced a field of 49.8 Gauss/Amp.

The solenoid current supply used was a Roband Power Supply Type No P1912. This unit supplies a current of 2-10 amps DC, continuously variable at a 100 V max., and according to the manufacturer's specifications exhibits a ripple of less than 0.5% peak to peak and a current stability of less than 0.5% for periods of 30 minutes, ambient temperature changes of 5°C and mains changes of ±10% Volts. The current required for three-loop focussing of the image intensifier was 7.5 amps when the E.H.T. was set to 30 kV.

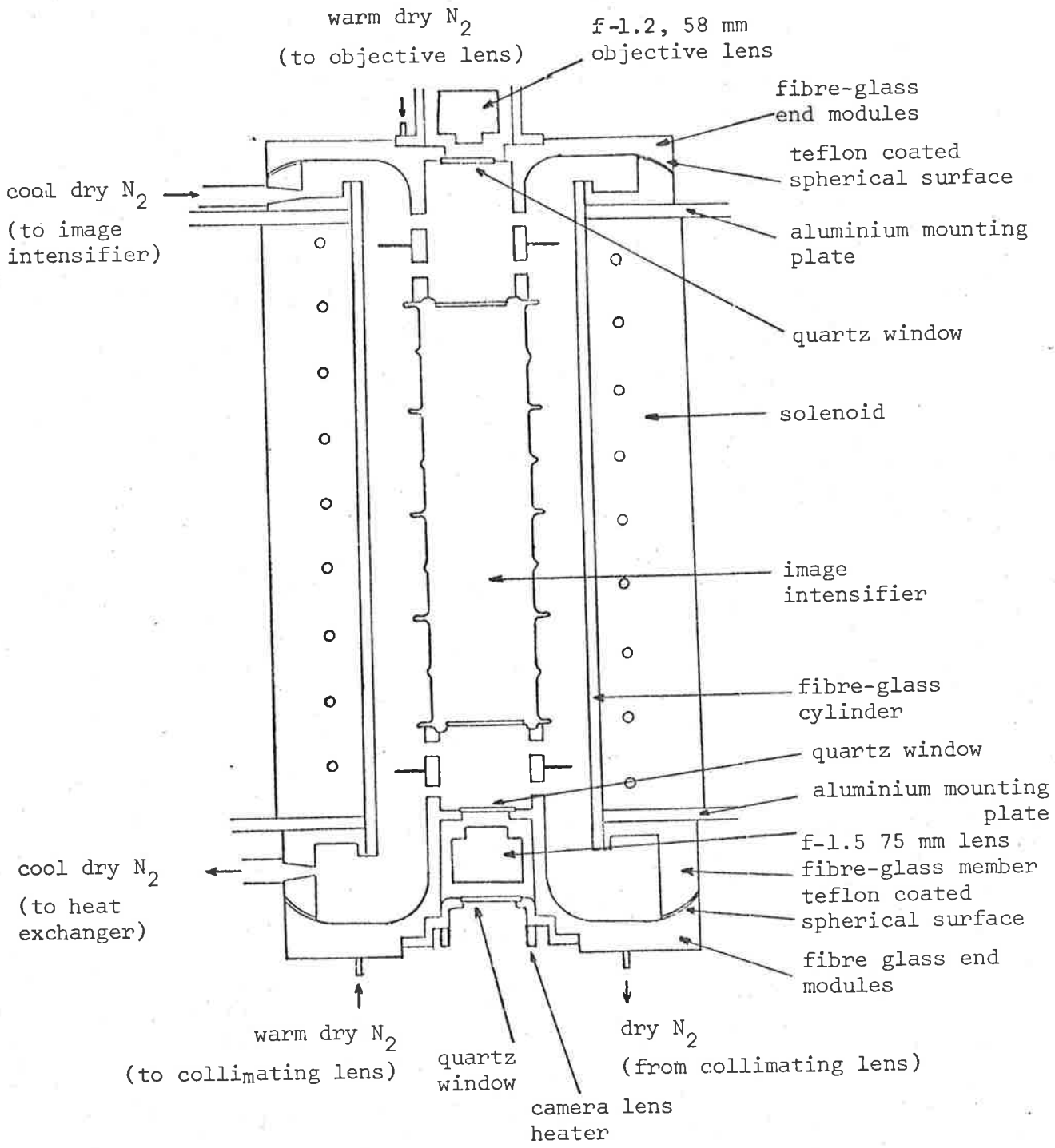

Figure 2.3. Schematic sketch of the mounting of the image intensifier tube within the solenoid.

2.2.7 General Mechanical Design

For efficient cooling, the image intensifier tube was mounted within the solenoid such that air could be directed onto the photo-cathode and circulated between the solenoid and the image intensifier. A schematic sketch of the mounting of the image intensifier tube within the solenoid appears in Figure 2.3. Essentially the system consisted of a fibre-glass cylinder mounted within the solenoid and two-fibre-glass end modules between which the image intensifier tube was "sandwiched" in place. These end modules included spherical teflon-coated mounting surfaces for mating with surfaces on the fibre-glass cylinder and by using silicon grease as a gasket cement, efficient sealing could be obtained. The spherical shape of these surfaces enabled the image intensifier tube to be accurately alligned with the optical axis. The whole assembly was mounted vertically on an aluminium frame.

Other features included the air ducting into the image intensifier chamber, a compartment in the bottom end module for mounting the f-1.5, 75mm lens through which a separate flow of air could be directed, 2mm quartz windows for insulation purposes mounted within the end modules and a recess in the bottom module for insertion of the camera lens or periscope to maintain the system light tight.

2.2.8 The Cooling System

The cooling system for the image intensifier essentially cooled the solenoid by circulating a brine solution consisting of 50% methanol and 50% de-ionized water through the solenoid and by directing dry nitrogen around the image intensifier tube. Figure 2.4 provides a block diagram of the arrangement of the cooling system. A Kelvinator Accessible Hermetic A 6330 3hp compressor using R 502 as a refridgerant cooled the methanol-

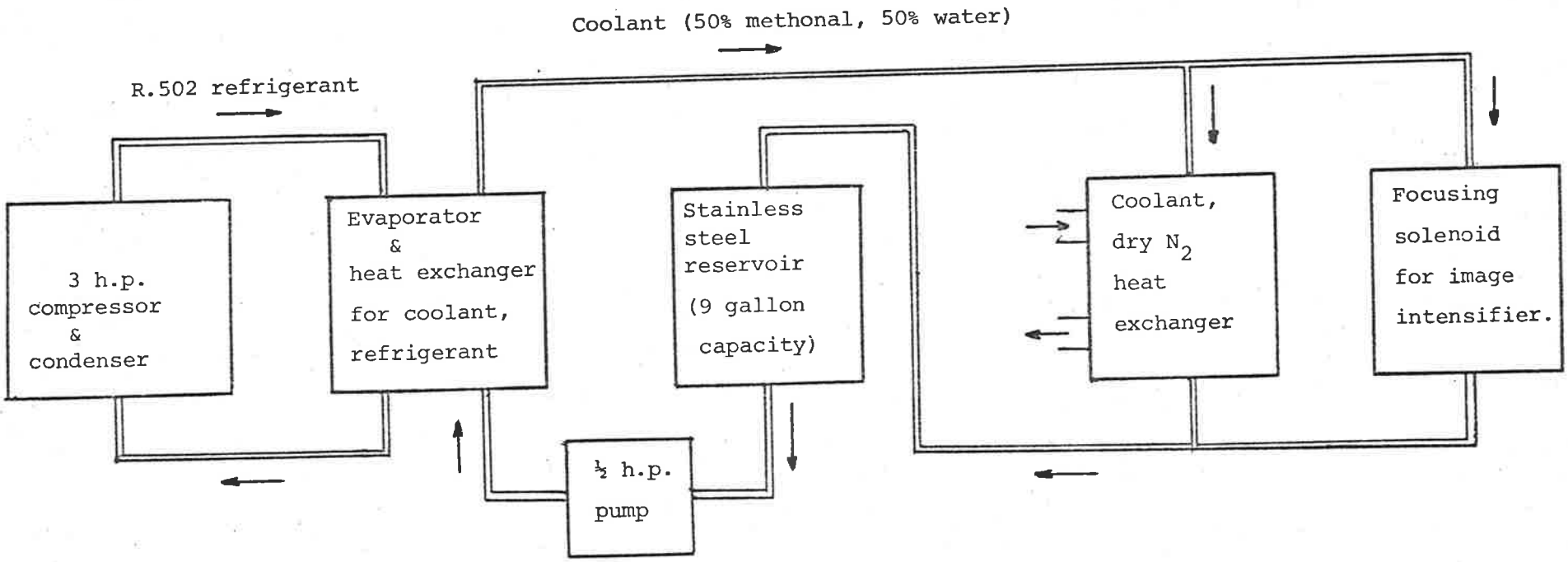

Figure 2.4 Block diagram of the cooling system for the image intensifier system.

brine coolant in an evaporator-heat exchanger unit. The methonal-brine coolant initially stored in a 9 gallon stainless steel reservoir was pumped through the heat exchanger to the solenoid and an additional heat exchanger connected in parallel. This additional heat exchanger cooled the dry-nitrogen which was circulated through the image intensifier chamber, and consisted of a vehicle heater unit. Additional features included a pressure sensitive switch which shut down the solenoid current supply, compressor and pump if the coolant flow stopped and a filter to remove any foreign matter in the coolant.

The system on a winters night could maintain the coolant temperature at the input to the solenoid at -39°C and the dry nitrogen temperature adjacent to the photo-cathode at -29°C when the solenoid current was set to 7.7 A.

Initially problems were encountered with fogging of the lenses and the quartz windows. This was overcome with the camera lens by positioning a heating coil around the lens and maintaining the lens at room temperature. Dry nitrogen heated to the order of 70°C was circulated through the sealed compartment containing the f-1.5 75 mm lens. With a gas flow such that a 220 cu ft capacity gas cylinder lasted for 20 hours, the air temperature in this lens compartment was maintained at 0°C. The exhausted air was then reheated and circulated through the space between the upper quartz window and the f-1.2, 58 mm objective lens.

2.3.1 Observations

Observations on moonless nights, weather permitting were carried out through 1972 and early 1973. Examples of observations from these nights are to be found in Figures 2.5, 2.6 and 2.7 and consist of negative prints enlarged on Ilfobrom 1B4.1P paper (a fairly high contract paper) from the original positive film. To aid comparison the print

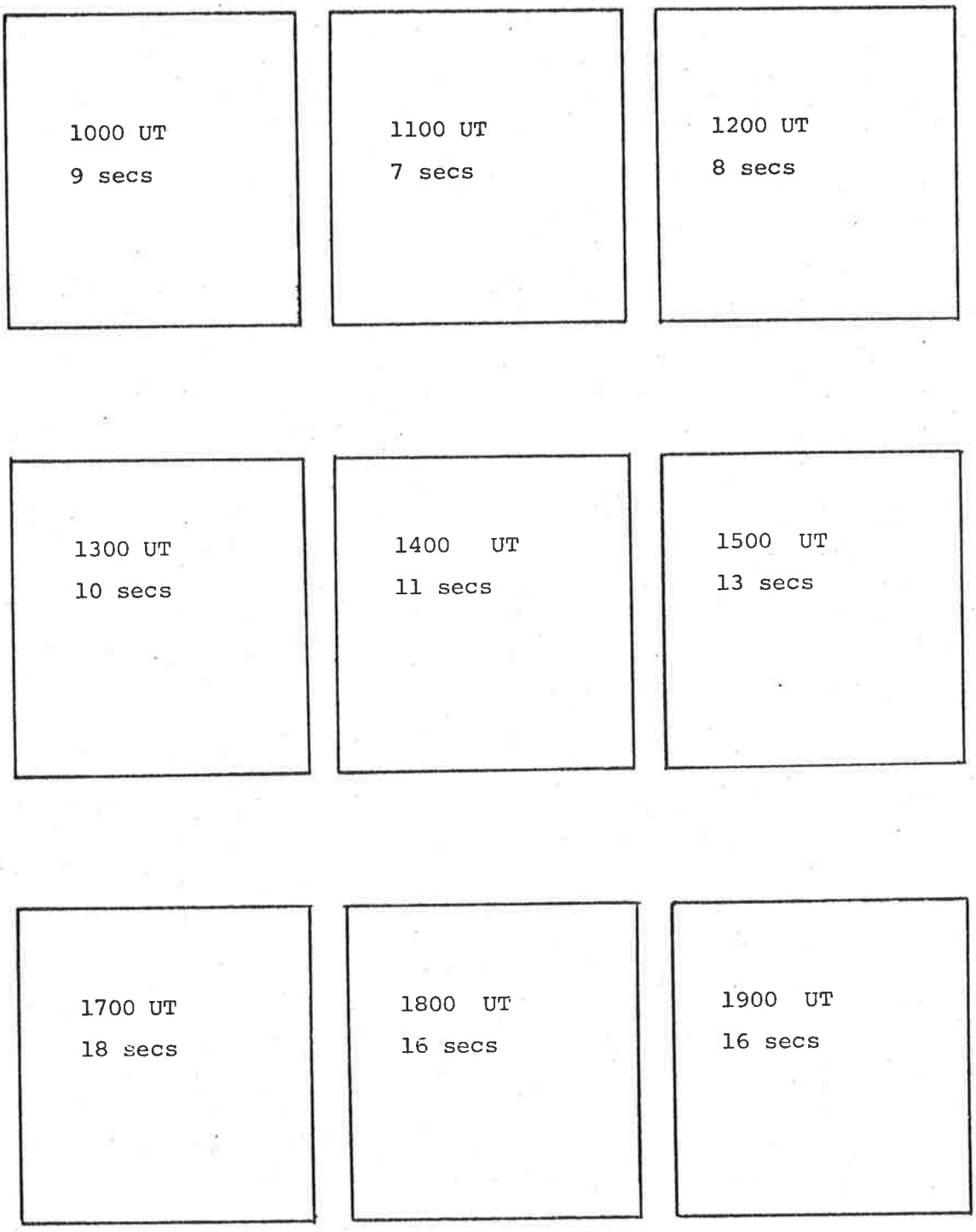

Figure 2.5 Prints (next page) of the sky pictures taken on the 3rd September 1972, using the 557.7nm filter and the "all sky" optics. The film exposure time was 1 minute, the EHT was 30 kV and the solenoid current set to 7.6A Indicated above are the times at which the pictures were taken and the print exposure time.

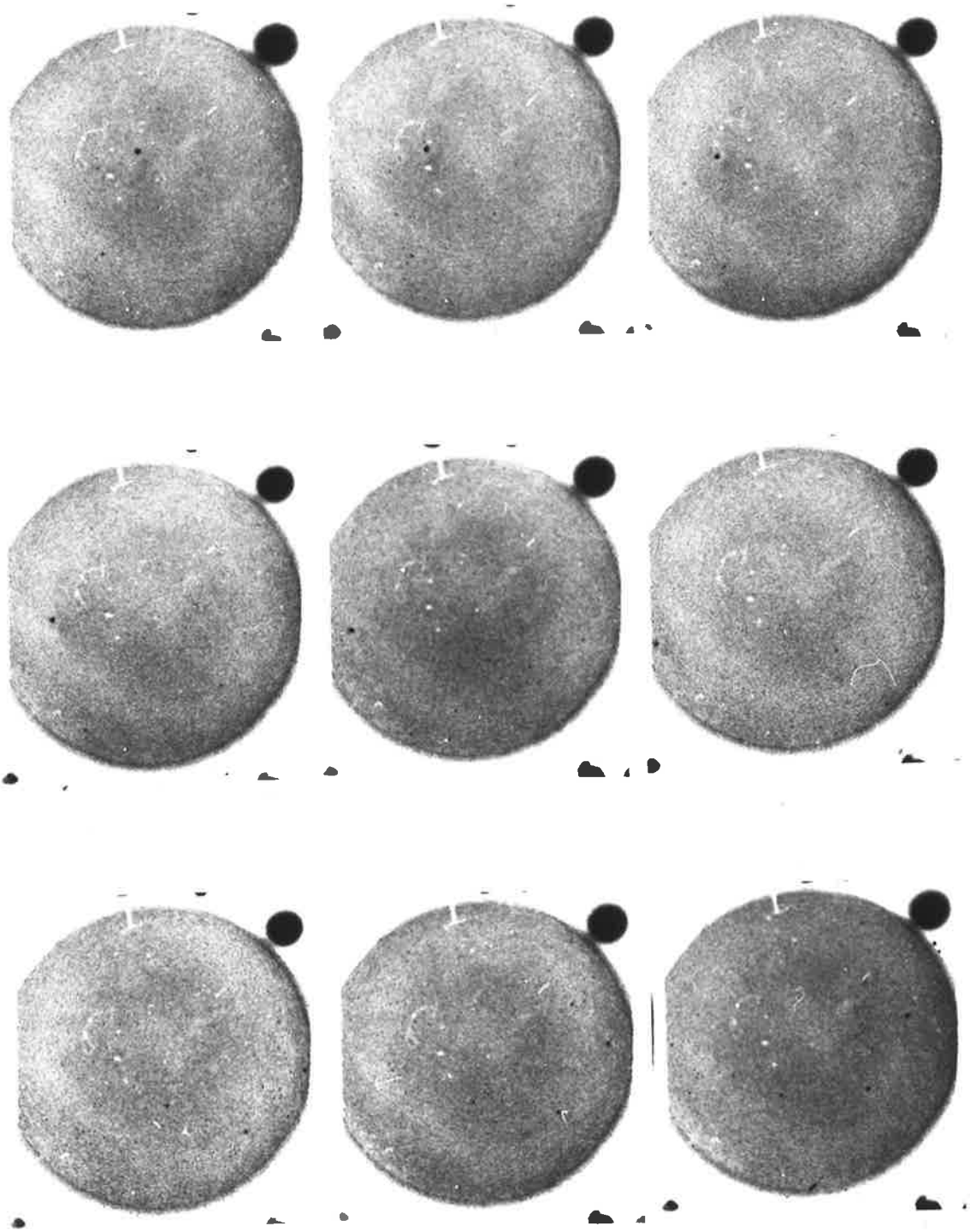

exposure times have been adjusted such that the nine sky pictures appearing in each figure have approximately equal density. Details such as the time in UT when the sky pictures were taken, print exposure time, EHT and solenoid current appear on the page preceding the figures.

In Figure 2.5, sky pictures taken using the 557.7nm filter and the "all sky" optics on 3 September 1973 appear with the film exposure time set to 1 minute, the EHT to 29 kV and the solenoid tc 7.5 A. An added refinement was the use of a "Van Rijhn" filter which consisted of photographic film characterized by decreasing transmission with increasing radius. This transmission filter was positioned below the interference filter and its object was to balance out the Van Rijhn effect in the airglow and thereby produce sky pictures with a more even density. The pictures are orientated such that north is towards the top of the page and east to the right. The cross, positioned slightly to the left of top of each picture, was due to an electric light pole and wires leading to this pole are also resolved. Stars moving from east to west appear as black dots and the white dots are throught to be photocathode "burns" produced previously by the brighter stars. No detail which cannot be attributed to the uneven transmission of the optics or to sky background is visually apparent. However, there was an overall decrease in airglow intensity on this night which is evidenced by the increasing print exposure time.

Sky pictures taken on the 8 June 1972 using the 630nm filter and the "all sky" optics appear in Figure 2.6. No "Van Rijhn" filter was used on this occasion and darkening in the sky pictures in areas corresponding to high zenith angles is apparent. Other features attributable to the [OI] λ 630nm airglow include the decreasing overall intensity from 1000 UT to 1430 UT and increasing intensity from there-on, as apparent from the print exposure times. This increase in overall intensity from 1600 UT onwards is due to predawn enchancement, and the

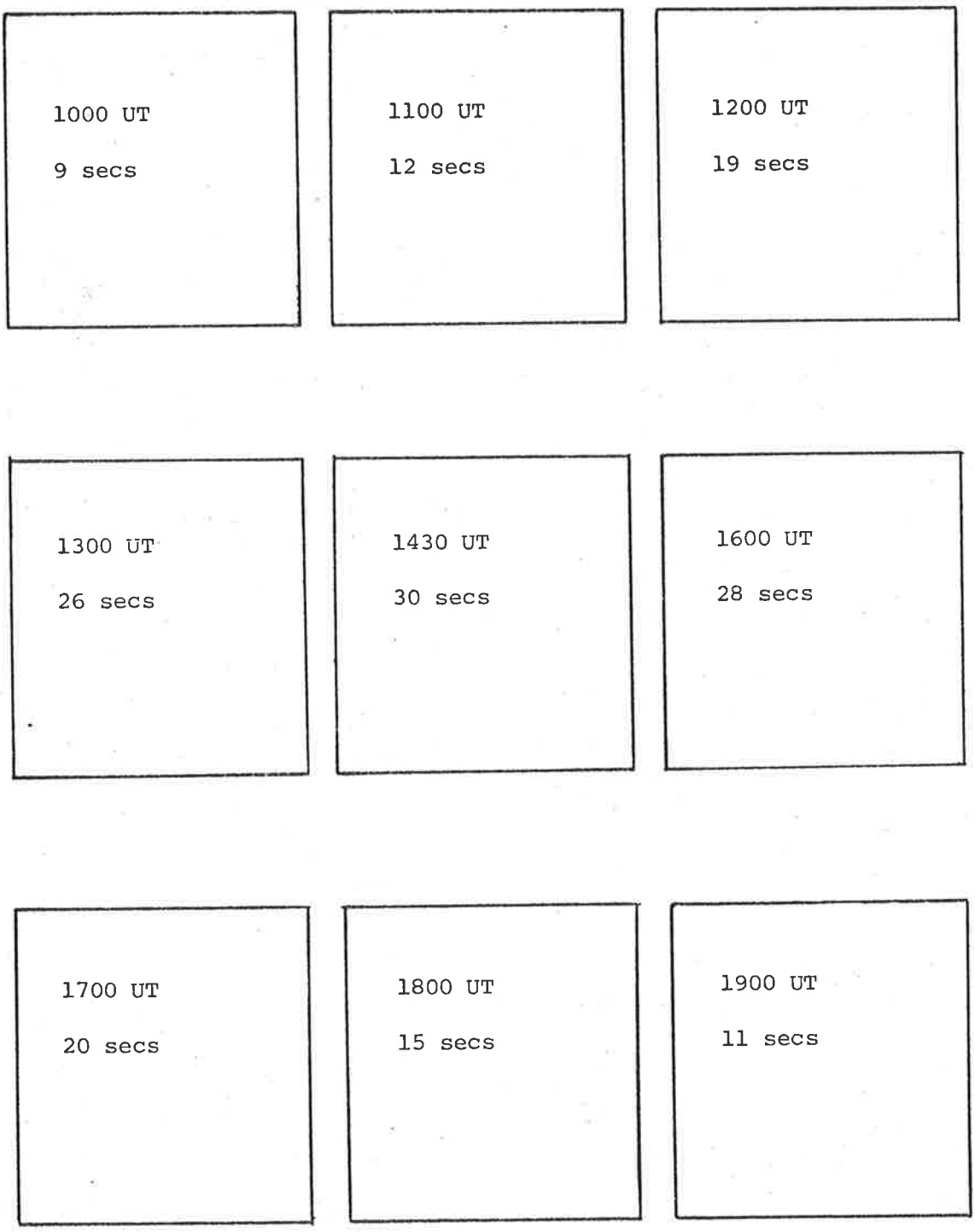

Figure 2.6 Prints (next page) of the sky pictures taken 8 June 1972 using the 630 mm filter and "all sky" optics. The film exposure time was 1 minute, the EHT was 29 kV and the solenoid current set to 7.5A. Indicated above are the times at which the pictures were taken and also the print exposure time.

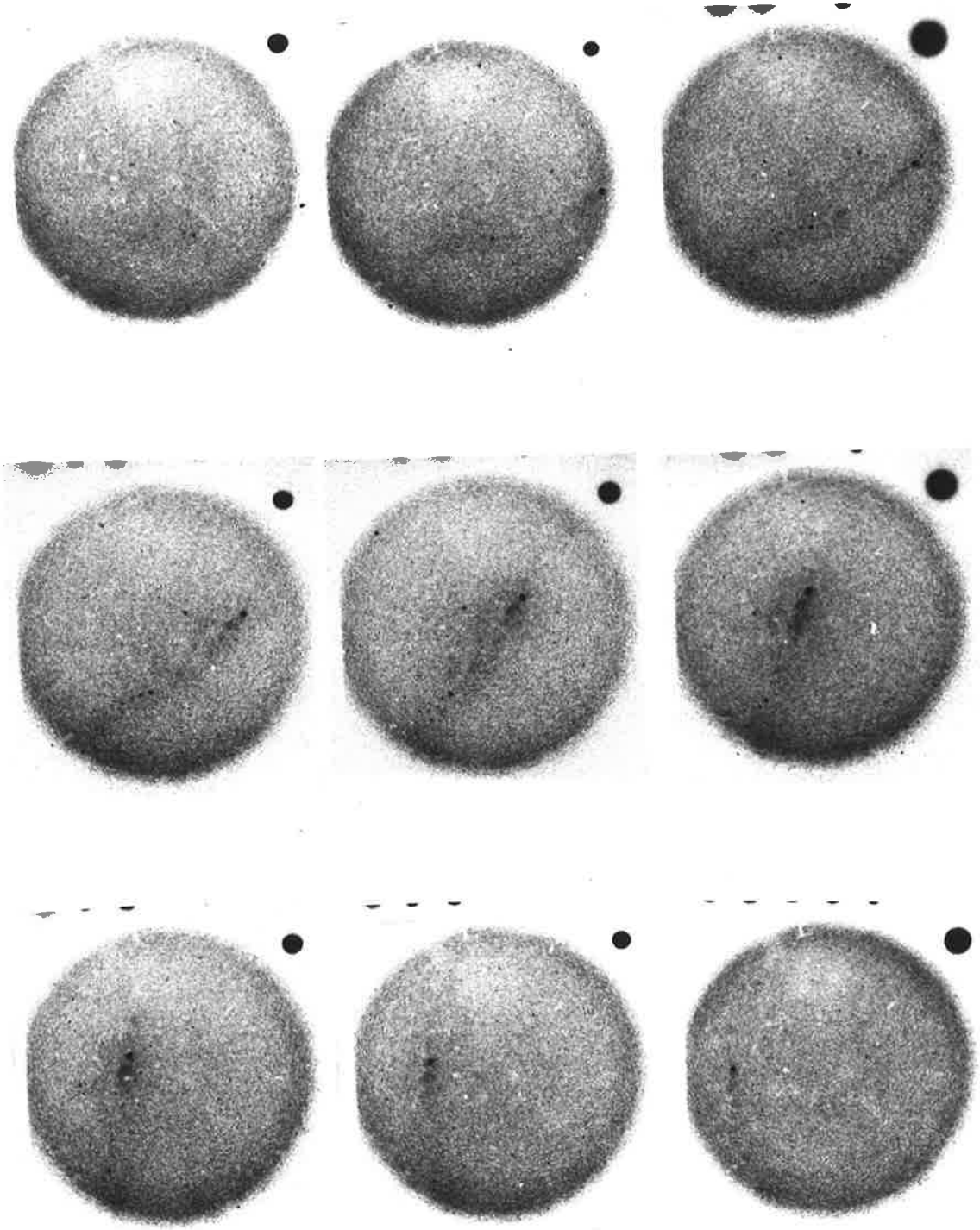

increased darkening in the east in the 1700 UT and the 1800 UT sky pictures compared to the 1000 UT and the 1100 UT sky pictures is also attributable to predawn enhancement. A comprehensive report on predawn enhancement as observed at Adelaide has been produced by Schaeffer (1970).

Finally, sky pictures taken with the 20° field of view optics and the 557.7nm filter appear in Figure 2.7. The exposure time for each frame was 1 minute with 4 minute intervals separating the frames pictured. There are no visually apparent features which can be attributed to the 557.7nm airglow.

2.3.2 Processing the Sky Pictures

The sky pictures for most nights were enlarged onto Ilfobrom 35.1P paper (a high contrast paper) and for some nights when the exposure time was 1 minute, their total number amounted to 700. However they visually revealed no more features that could be attributed to the airglow than that already reported. Copying the sky pictures onto Agfa-Contour film and Kodalith film and thereby enhancing the contrast also failed to reveal any significant airglow structure. Non-uniformities in the sky pictures produced by the irregular transmission characteristics of the optics, e.g. caused by the filter, tended to mask the airglow features.

Spatial filtering was also carried out by positioning an opaque spot at the centre of the Fraunhoffer diffraction pattern of the sky picture. This, according to the size of the spot, removes the D.C. background signal and low frequency components. However the problem remains of structure in the sky pictures whose scale size is similar to the expected airglow features. A more sophisticated filtering technique in which a hologram of the transparency is made has been outlined by Cutrona (1965) but this has not been tried.

In the light of the 4-field photometer results, useful information

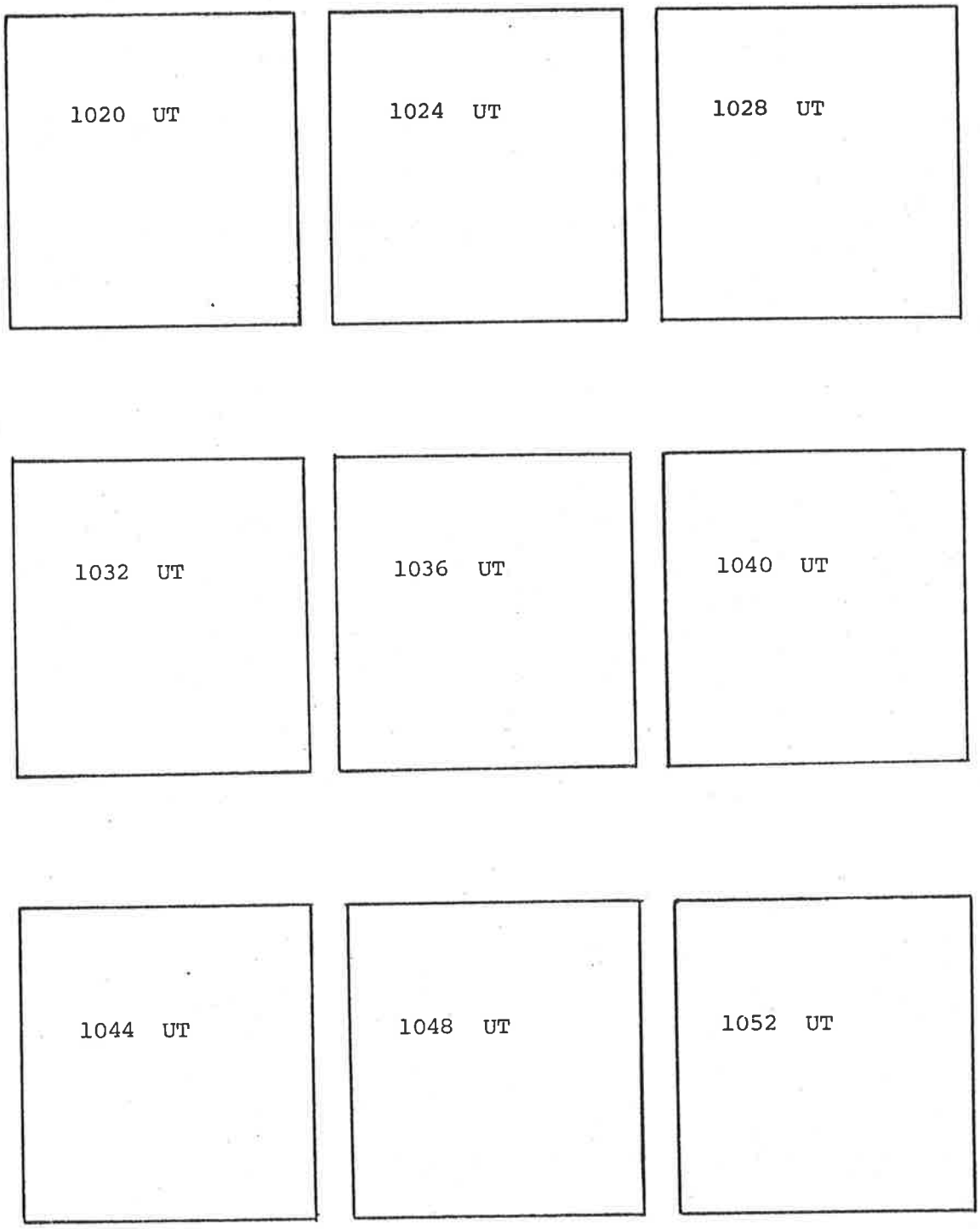

Figure 2.7 Prints (next page) of the sky pictures taken on the 2nd September 1972 using the 557.7 nm filter and the 20^0 field of view optics. The film exposure time was 1 minute, the EHT was 29 kV and the solenoid current was set to 7.5A. Indicated above are the times at which the pictures were taken. The print exposure time was the same for each picture.

relating to the airglow pattern could be obtained by cross-correlating different transparencies as outlined by Cutrona. This could only be carried out in the present case using the 20° field of view optics since the larger field of view optics produces image distortion. Therefore as one will be concerned with structure whose amplitude is only 1 or 2% of the total signal, it is necessary to ensure that sufficient information is contained in each transparency such that useful data may be extracted and it is therefore necessary to consider the statistics of an image intensifier-film system and the volume of information required in each sky picture.

2.4.1 Statistical Considerations

In Section 1.3.2 the possibility of finding the velocity of moving patterns in the airglow is discussed. In Appendix A, the error in determining the lag time between signals from two spaced receivers is related to the total number of photons counted in a certain time interval and in an analogous manner, the error in the space shift determined from two sky pictures may be related to the total number of stored photons within each sky picture.

Equations A.14 and A.15 may be written in the form

$$\sigma x \approx \frac{X}{\pi\alpha(\overline{N}n)^{\frac{1}{2}}} \qquad (2.3)$$

where σx is the error in the space shift, X is the scale size of the sky pattern e.g. the wave length of a gravity wave, $\overline{N}n$ is the number of stored photons and α, defined in Appendix A, is the relative amplitude of the intensity variation. Equation (2.3) provides a satisfactory estimate of the error in space shift only if the scale sizes of the intensity variations are less than the diameter of the field of view. The error in space shift σx is related to the error in the velocity σv by

$$\sigma x = \sigma v \, \tau_0 \, . \qquad (2.4)$$

Using the numbers X = 35 km, V = 70 m-s^{-1}, α = 0.01 and τ_0 = 1 minute in equations (2.3) and (2.4), one finds that to determine the velocity of the pattern to the accuracy such that

$$\frac{\sigma v}{v} \leq 0.1,$$

the number of stored photons within a sky picture must exceed $\sim 10^7$. The number of expected photo-electrons per minute from the present system using the 20° field of view and an ideal filter is $\sim 3 \times 10^7$. With the filter used this number is $\sim 1.5 \times 10^7$. Therefore the image intensifier coupled to an efficient recording system where most photo-electrons are stored has the potential to find the velocity of moving patterns in the [OI] λ 557.7nm airglow.

2.4.2 Image Intensifier-Film Statistics

Iredale and Ryden (1969) have theoretically considered the quality of images obtained with an image intensifier-film system and Hinder and Iredale (1972) have carried out measurements on the granularity of Tri-X film exposed directly and via an EMI 9694 image intensifier tube. In this section deductions relating to airglow studies will be made by utilizing results appearing in these two papers.

Iredale and Ryden concluded that when an intensifier is used to give a high light gain, the quality of the image is determined primarily by statistical variations in the number of photo-electrons representing the signal and the effects of the statistical variations independent of location in the multiplication process. McGee (1971) has indicated that these variations are greater than what would be expected from Poissonian

statistics only. They also concluded that when the light gain is small, the granularity is determined primarily by that of the film alone and image quality should be that equivalent to when the film is exposed directly.

However Hinder and Iredale found that spatial gain variations in the image intensifier were a further source of granularity and the magnitude of the granularity was several times the limiting granularity of the film in their particular system. In the present case when cross-correlation techniques are applied to the sky pictures, spatial gain and transmission variations in the system are not a source of noise provided that these variations are common to all sky pictures.

In these two papers a parameter S, designated the number of stored photons, is used and this parameter is directly related to the granularity of the film and also to the equivalent or effective quantum efficiency ϵ such that

$$S = N \epsilon \tag{2.5}$$

where N corresponds to a signal of N photons. The equivalent quantum efficiency of the system ϵ_{IF} is given by

$$\frac{1}{\epsilon_{IF}} = \frac{1}{\epsilon_{Ilim}} + \frac{1}{G'\epsilon_F} \tag{2.6}$$

where ϵ_{Ilim} is the equivalent quantum efficiency of the image intensifier and cannot be expected to be greater than 0.75 of that of the photo-cathode efficiency due to the characteristics of the multiplication process, ϵ_F is the equivalent quantum efficiency of the film and G' is the brightness gain at the film.

For Tri-X film directly exposed the number of stored photons is $\sim 10^7$ per cm^2. In the present system it is not desirable to have the equivalent quantum efficiency much less than the photo-cathode

efficiency. According to the previous section, the maximum reduction that could be tolerated would be a factor of 3. For an equivalent quantum efficiency of 1/3 of that the photo-cathode efficiency, it is estimated that the number of stored photons would decrease from 10^7 per cm^2 to 5×10^6 per cm^2 due to increased granularity. Using 16mm film as in the present case, the film area amounted to only 0.4 cm^2 and taking into account background light, the effective number of stored photons from the airglow cannot be expected to exceed 10^6.

In conclusion to provide sky pictures usable in cross-correlation analysis, it is necessary to use film with a useable area exceeding 4 cm^2 and to also use a filter tailored to suit the optics as outlined in Section 2.2.3. In these circumstances with the gain optimised, each sky picture should contain the required number of stored photons.

CHAPTER 3

A SCANNING FIELD-STOP PHOTOMETER

3.1 Introduction

This chapter will be concerned with some technical considerations involved in designing a 4-field of view photometer suitable for obtaining the drift velocities of small scale, small amplitude fluctuations in the night airglow. Initially a study of noise characteristics will be carried out with emphasis on the possible sources of errors involved in calculating values of the drift velocity. Parameters involved with these errors along with the scale size and the intensity amplitude of λ 557.7nm(OI) features will be taken into account in the instrument design.

3.2.1 Noise Consideration

In section 1.3.2 the velocity of a one-dimensional pattern moving across two spaced receivers is determined by finding the peak of the cross correlation function of the two signals at some time τ'. With a spacing ξ_0, the velocity V' is given by

$$V' = \xi_0/\tau'. \tag{3.1}$$

It is evident in equation (1.10) that with the pattern changing in a random fashion with time this velocity V', sometimes called the "apparent velocity", will have a larger value than the true velocity.

The time shift τ' and an associated standard deviation $\sigma\tau'$ will be related to the standard deviation $\sigma v'$ in velocity V' by

$$\frac{\sigma\tau'}{\tau'} = \frac{\sigma v'}{v'} \quad . \tag{3.2}$$

The uncertainty in the time lag may be accounted for by two independent factors. One results from the finite sampling of photon events by the photometer while the other is due to change in the observed pattern. Thus the standard deviation $\sigma\tau'$ may be expressed as

$$\sigma\tau'^2 = \sigma tP^2 + \sigma tR^2 \tag{3.3}$$

where σtP is the standard deviation introduced by Poisson statistics due to resolution limits in the photometer while σtR is due to changes in the airglow pattern as it moves across the fields of view.

3.2.2 Estimation of σtR

In the estimation of the standard deviation σtR the airglow fluctuations will be assumed to be Gaussian in nature whereas they are more likely to be due to a superposition of waves whose form will change as scattering and dissipation occurs. Also one will be observing a two dimensional cross-section only of a three-dimensional pattern and hence at best the result obtained will be only true in a qualitative sense with respect to airglow patterns.

Buckley (1971) has estimated that the root-mean square value of deviations in time lag for the Gaussian form of the correlation function is

$$\sigma tR = \sqrt{\frac{1}{\rho_m^2} - 1}\ \sqrt{\frac{T_c}{T_L}}\ T_c \tag{3.4}$$

where ρ_m is the maximum value of the cross-correlation function, T_L is the time-length of the data and T_c is the width of the corss-correlation function. The Gaussian form of the correlation function discussed in section 1.3.2 is (Fedor and Plywaski, 1972)

$$\rho(\xi,\tau) = \exp\left[-\tfrac{1}{2}\left\{\left(\frac{\xi-V\tau}{d}\right)^2 + \tau^2/b^2\right\}\right] \quad (3.5)$$

The parameters of this equation are defined in section 1.3.3. The maximum value ρ_m of $\rho(\xi, \tau)$ is

$$\rho_m = \exp\left[-\frac{\xi_0{}^2\beta^2}{2d^2(1+\beta^2)}\right] \quad (3.6)$$

and the characteristic width is

$$T_c{}^2 = \frac{2b^2}{(1/\beta^2)+1} \quad (3.7)$$

where $\beta = d/bv$ and is a measure of the importance of random changes in the pattern (Fooks, 1965).

The relative error in time lag $\sigma tR/\tau'$ has been plotted against the ratio of the distance between receivers or fields of view ξ_0 to the "characteristic size" d of the pattern in Figure 3.1 for a true velocity v of 50m/s, a characteristic scale size of 5 km, and a length of data T_L of 600 secs. Values of b have been chosen, corresponding to values of β of $\frac{1}{4}$, $\frac{1}{2}$, 1. Also the points where the maximum of the cross-correlation function ρ_m has a value of a $\frac{1}{2}$ are indicated.

There are two features which require comment. Firstly, the curves in figure 3.1 asymptote to a minimum value in relative error for smaller spacings of the receivers. This limit is given by

$$\left(\frac{\sigma tR}{\tau'}\right)_{min} = \frac{2^{3/4}\beta^{3/2}}{(1+\beta^2)^{\frac{1}{4}}}\left(\frac{b}{T_L}\right)^{\frac{1}{2}} . \quad (3.8)$$

Therefore the only method for increasing the accuracy of the velocity measurement would be to increase T_L, but T_L is limited to values where the drift velocity does not change significantly. This limit in the accuracy of the velocity imposed by the rate of random changes in the pattern may very well be the main source of error in drift velocities determined by the use of partially reflected radio waves where the instrumental noise contribution would be small. Stubbs (1973) calculated

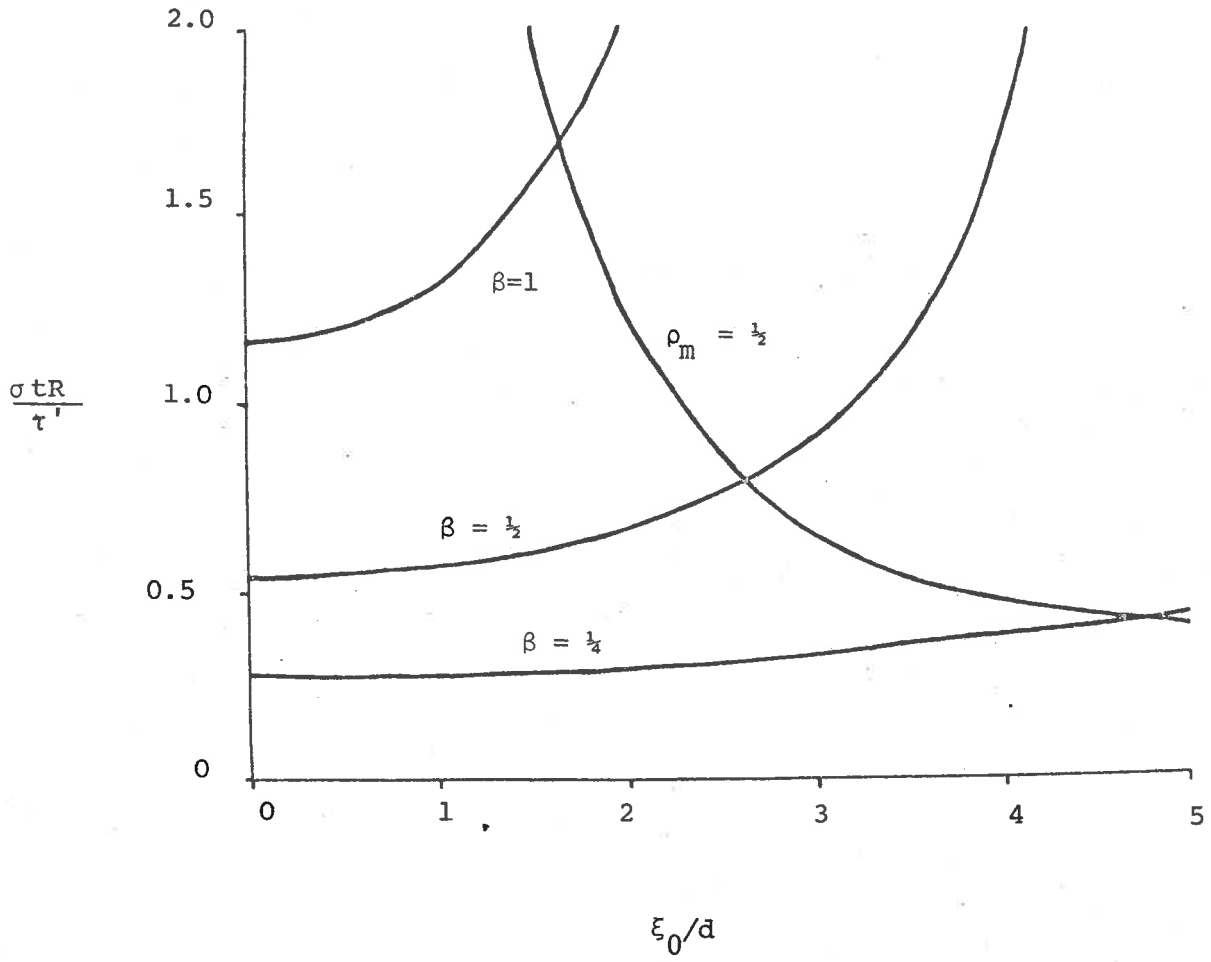

Figure 3.1 Plot of $\sigma tR/\tau'$, the relative error in time lag against ξ_0/d, the ratio of the distance between receivers ξ_0 and the "characteristic size" d of the pattern for various values of β, a measure of the importance of random changes. Also a plot of points corresponding to where the maximum of the cross-correlation function $\rho_m = 0.5$.

that the standard deviation of velocities found by this technique to be 10 ms^{-1} for the magnitude of the velocity and 14° for the direction. It would not be unexpected if a significant proportion of the error was due to random changes in the pattern.

The relative error in velocity due to σtR will vary inversely as the receiver spacing ξ_0 whereas the error resulting from σtP increases with ξ_0. Hence for a given instrument, a compromise value of ξ_0 for which the relative error is a minimum must exist. Golley and Rossiter (1970) experimentally determined that the optimum value of ξ_0 corresponds to a value of ρ_m of 0.5 and it is of interest to note that this, as seen in Figure 3.1, corresponds to values of ξ_0/d where values of $\sigma tR/\tau'$ start to increase appreciably. This adjusting of ξ_0 in photometer design to values such that ρ_m is of the order of 0.5 should also be relevant to airglow studies.

3.2.3 Estimation of σtP

Although an absolute estimate of σtR and ξ_0 where $\rho_m \simeq 0.5$ remains undetermined for airglow patterns, nevertheless σtP must be restricted to values such that errors in velocity due to instrumental limitations are acceptable. An error in magnitude of less than 10% for a significant range of data would be considered satisfactory. Typical characteristics of the short term fluctuations in data collected from Mt. Torrens (to be reported in chapter 4) consisted of variations with periods from 2 to 15 minutes and relative amplitudes from 5% down to less than the noise level. Although increasing velocities lead to progressively decreasing lag times as can be seen from equation (3.2), causing the relative error in velocity to increase, parameters governing this error will be considered

for a compromise velocity of 70 m/s.

In Appendix A it is shown that for a wave type structure σtP is given by

$$\sigma tP \simeq \frac{T}{\pi\alpha(\overline{N}n)^{\frac{1}{2}}} \tag{3.9}$$

where T is the period of the wave, $\overline{N}$ is the mean number of signal counts in a sampling interval, n is the number of sampling intervals which, when multiplied by the sampling interval, would equal the period of observation, and α is the relative amplitude of the signal. The period of observation should be less than the time scale over which the velocity does not change significantly in speed or direction. The signal count rate $\overline{N}$ is given by

$$\overline{N} = \frac{\varepsilon A\Omega}{4\pi} \times 10^{10} \times \text{Intensity in Rayleighs} \tag{3.10}$$

where ε is the efficiency of the photometer (transmission of the optics × efficiency of the photocathode), A is the area of the entrance pupil of the photometer in meters^2 and Ω is the field of view. Typically the intensity of λ 557.7nm airglow is near 100 Rayleighs and the efficiency ε near 10^{-1}.

3.2.4 Dimensions of the Fields of View

In Appendix B it is shown that a circular field of view with a diameter d at the height of observation will be sensitive to a propagating wave-type structure of wavelength λ only when $\lambda > 1.2d$.

With respect to structural scale sizes at the height of the λ 557.7nm emissions, Vincent (1972) reports of ionospheric irregularities near 95 km with periods of 5 to 10 minutes which in relation to the phase velocity measurements would indicate horizontal scale sizes of 5 to 100 km.

In the results to be reported in chapter 4, periodic variations of 2 minutes and greater and velocities of 40 ms^{-1} were observed in the λ 557.7nm airglow indicating scale sizes of upwards of 5 km. Also limitations are imposed by the thickness of the emitting layer as one could not logically expect to observe structure whose scale size is greatly exceeded by the thickness of the layer. In section 1.2.1 a value of 6 km is associated with the thickness of the 557.7nm airglow layer. From such considerations, a photometer whose field of view at 96 km height is 2 km in diameter is suggested thus allowing for the possibility for the detection of irregularities of scale size greater than 2.5 km.

3.2.5 Size of the Entrance Pupil

From equations (3.2), (3.9) and (3.10) it is possible to quantitatively estimate the size of the entrance pupil required for drift velocity measurements. In this estimate, no contributions due to changes in the airglow pattern are included. On combining the above mentioned equations and setting the period T of the fluctuations equal to the period of observation or time length of data, one obtains the equation

$$d \sim 1.8 \times 10^{-5} \frac{V}{\alpha \xi_0} \frac{V}{\sigma V} \left(\frac{T}{\varepsilon I_R \Omega} \right) \qquad (3.11)$$

where d is the diameter of the entrance pupil in metres. If the two fields of view are viewed sequentially, the intensity I_R will be effectively reduced by a factor of 2. Setting the relative error in velocity $\frac{\sigma v}{v} = 0.1$, velocity = 70 ms^{-1}, the relative amplitude $\alpha = 0.01$ the period T = 600 seconds, the photometer efficiency $\varepsilon = 0.1$, the effective intensity I_R = 50 Rayleighs, Ω determined from a field of view of 2 km at 96 km and the spacing ξ_0 between the fields of view of 2.5 km, the required diameter of the entrance pupil would be

$$d \sim 0.30 \text{ metres.}$$

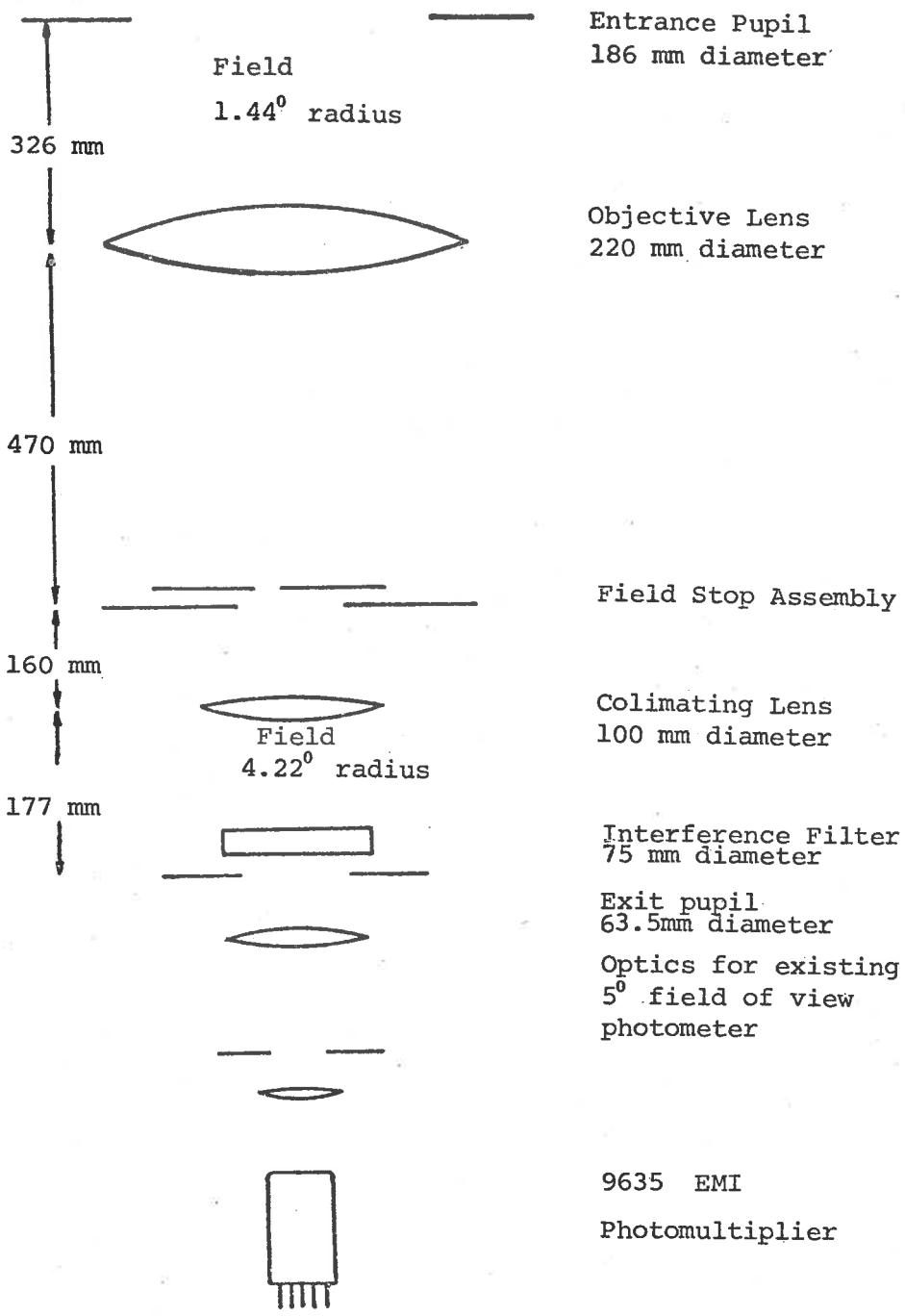

Figure 3.2 Schematic sketch of the optical system in the Mt. Torrens 4-field photometer

3.3 Mt. Torrens Four-field Photometer

It must be emphasized at this stage that the Mt. Torrens photometer was originated specifically for testing the feasibility of obtaining drift velocities from airglow patterns and when set up initially, little was known about the nature of the patterns. The photometer consisted of an existing 5° field of view photometer with a 3" aperture of the type described by Schaeffer (1970) and onto this an additional optical system was added. A moving field stop capable of sequentially observing four fields of view completed the modifications.

3.3.1 OPTICS AND FILTER

The details of the optical system used in the Mt. Torrens 4-field photometer are shown in Figure 3.2. To the original 5° field of view system an objective lens of diameter 220 mm and focal length of 470 mm, a field stop assembly and a collimating lens of 100 mm diameter and 177 mm focal length were added. The exit pupil of the added optical system was situated at the position of the interference filter and due to edge deteriation in the filter, only a central area of diameter 63.5 mm was used. Thus the entrance pupil situated 326 mm above the objective lens had a diameter of 186 mm.

The angular size and spacing of the fields of view were limited by lens and filter considerations. For interference filters, increasing the angle of incidence results in the peak value of the wave length of the pass band being shifted to shorter wave lengths, while increasing the temperature of the filter results in the peak value of the wave length being shifted to longer wave lengths. In Figure 3.3a the fields of view arrangement is illustrated with the field of view spacing at 96 km being 2.26 km and the diameter of each field of view being 1.62 km. The angle of incidence of the central ray of each field of view was 2.81° and the

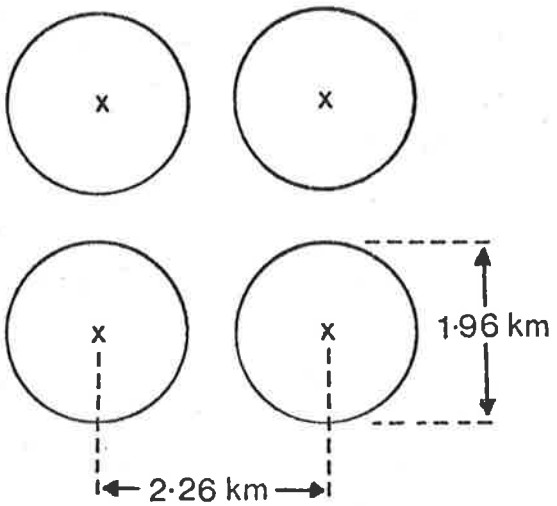

Figure 3.3a Dimensions of the fields of view at an altitude of 96 km for the 4-field photometer.

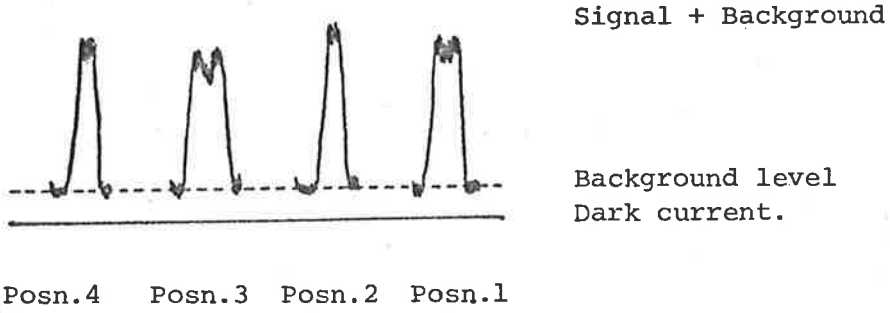

Figure 3.3b Example of the ratio of the signal to background light level of the 4-field scanning photometer obtained by tilting the filter.

wave length of the pass band peak at this angle was 557.7nm when the filter temperature was 40°C. The pass band of the filter at normal incidence was 0.9nm and tilting the filter by 3° resulted in an increase of 0.2nm. The contribution of background was estimated by tilting the filter to where 557.7nm lies outside the band pass hence allowing an estimate of the background. Figure 3.3b shows an example of the variation of light intensity as the band pass is moved in and out of the emission line for each field of view. Typically on a moonless night the 557.7nm airglow line was five times more intense than the background contribution being transmitted through the filter. In observational mode the background component was not removed since a constant background would not affect the results. However stars brighter than approximately magnitude 4 moving across the field of view presented problems due to the changing background.

Finally, the four different fields of view were obtained by moving the field stop with respect to the rest of the optics. This was achieved by two spring-solenoid mechanisms, the respective off-off, off-on, on-off and on-on modes of the solenoids providing the four recording positions. The time of viewing of each position was 2.5 seconds followed by a "dead time" of 0.25 seconds therefore allowing the field stop to arrive at the next position and resulting in the cycle being repeated every 11 seconds.

3.3.2 DETECTING AND RECORDING SYSTEM

The photomultiplier used was a EMI 9635 B tube which has a Bi-alkali (K-Cs) photocathode and a quantum efficiency of 10% at 557.7nm. As the signal count rate is large it was decided that there was little to be gained in developing a pulse counting circuit for the photomultiplier and its output was fed into a low current amplifier and this provided a 0 to 1 volt output. Due to the proximity of a heater for the filters, some measure of cooling the photomultiplier was found necessary and this was

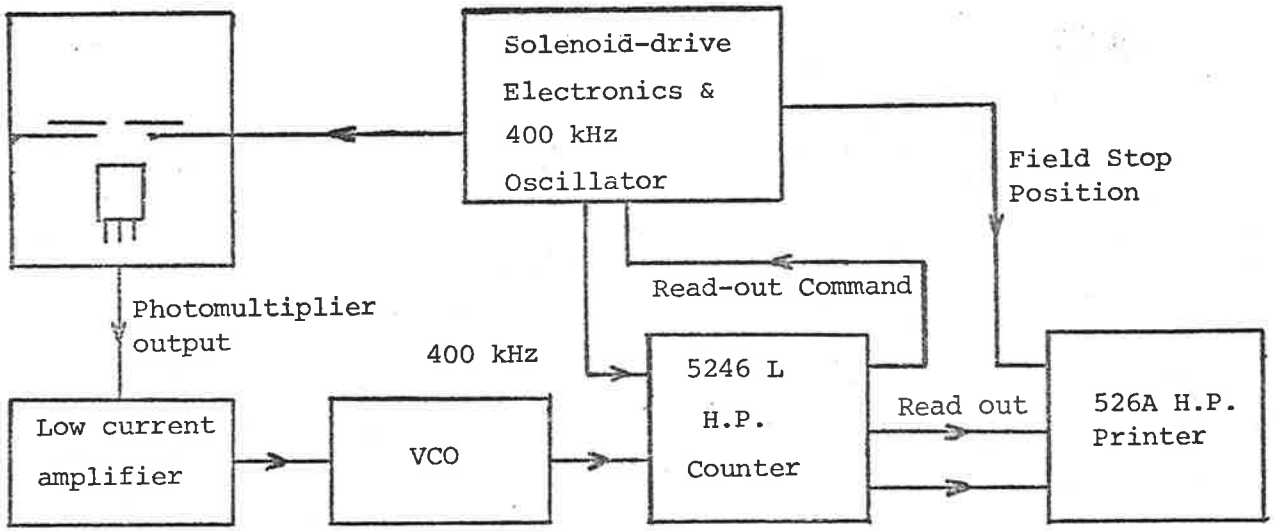

Figure 3.4 Flow chart of the electronics used in the 4-field photometer.

achieved by blowing the external night air (which is normally in the range 2°C to 15°C) through the photomultiplier chamber. Under these circumstances the dark current was typically two orders of magnitude less than the signal.

Figure 3.4 is a flow chart from which the sequence of each operation can be traced. The low current amplifier output was converted to a pulse-type form by a VCO and this was fed to a 5246 L H.P. counter. The gating time of this counter was set to 2.5 sec by an external oscillator and the read-out command provided by this gate also controlled the position of the field stop through the solenoid-drive electronics. The read out mode of the counter, which is the time delay between the end of one measurement and the commencement of a new measurement, was set to 0.25 sec during which the digitized intensity provided by the counter and the field stop position provided by the solenoid drive circuitry were printed out by a 526A H.P. printer.

A 5° field of view tilting photometer of the type described by Schaeffer (1970) was run concurrently and also monitored the 557.7nm emission. A schematic sketch of the photometer system is given in Figure 3.5.

3.3.3 SENSITIVITY

Equation (3.11) can now be used to estimate α for the Mt. Torrens 4-field photometer, i.e. the limiting value of relative intensity of the fluctuation for which values of drift velocity can be calculated with reasonable certainty. The value of α is 0.032, but as will be pointed out in the results, the relative error in velocity magnitude was relaxed to 20% and the data length was extended to 18 minutes allowing velocity estimates to be given when α was as small as 0.01.

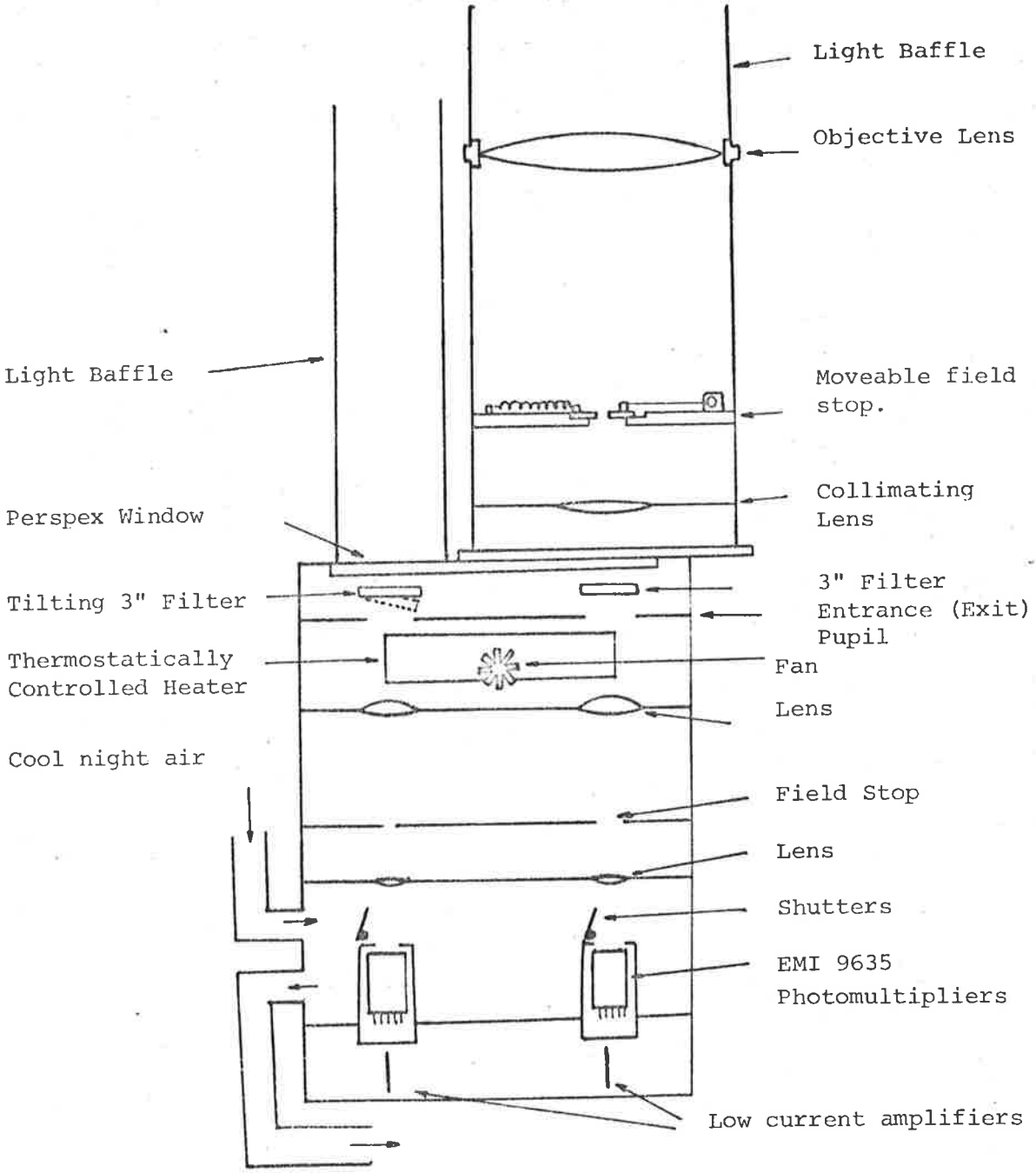

Figure 3.5 Schematic diagram for scanning field-stop photometer and tilting filter photometer.

3.4 Design Suggestions for Future Multiple-Field Photometers

Economically, the viewing of each field sequentially by a scanning method incorporated in one photometer would be superior to a system where each field is viewed continuously. For each to be equivalent, the first system would be required to collect four times the light intensity and a low cost Fresnel Lens or parabolic mirrors would make this a viable proposition.

The problem of the central rays of each field of view being at non-normal incidence with respect to the interference filter could be alleviated either by synchronously tilting the filter as the field-stop changes position in such a manner these central rays remain normal for all field stop positions or by employing a different system for multiple field viewing. One suggestion is to use a scanning coelostat system. Another refinement would be to remove the background for every observation by again using the variation of band pass wave length with the angle of incidence property of interference filters.

In an observational program, collecting data at the rate of a 4-5 figure number every 2-3 seconds would result in a large volume of data, but efficient and inexpensive data handing systems of the required capacity are now available. In summary the cost of a 4-field photometer is not high by modern standards while the scientific value of the data may be high, as suggested by the results already obtained.

CHAPTER 4

RESULTS FROM THE 4-FIELD PHOTOMETER

4.1 Introduction

This chapter will be concerned with the method used in analysing the results from the 4-field photometer, and also a description of the results which were obtained from observations on λ 557.7nm (OI) intensities. From the data, drift velocities of the intensity fluctuations and their power spectra were deduced.

The results will be reported in two sections. In the first section, interesting examples of λ 557.7nm intensity fluctuations along with related drift velocities and power spectra will be given while in the second, scatter plots of the drift velocities for a particular night along with a mean power spectrum for that night will be reported. Also for two nights, wind velocities, measured by finding the Doppler Shift of the λ 557.7nm (OI) line, were available and this will be compared with the drift velocities.

4.1.1 DETERMINATION OF THE DRIFT VELOCITIES

The drift velocity or horizontal trace speed was determined from the lag time in structure viewed from the four fields of view. The data were not examined spectrally in which technique a horizontal trace speed appropriate to each frequency is found as the S/N ratio was usually only adequate to determine the velocity with any confidence for only the most dominant feature existing in the airglow pattern at that time. Also as pointed out by Hines (1974), a problem still exists in a full spectral analysis since several patterns, at a given frequency, propagating in different directions would yield a meaningless velocity.

To determine the most suitable time-lengths of data, blocks of 55 minute duration (corresponding to 300 data points for each field of view) were divided into lengths of 55/n minutes and overall, n = 3 gave the most reliable values of drift velocities. This record length of 18 minutes probably represents a compromise where the drift velocity on most occasions does not change appreciably in this interval and σtP, defined by equation (3.9), is within reasonable limits. Although long period structure and trends were not removed, the value of the drift velocity obtained will apply mainly for structure whose period is less than the length of data (18 minutes).

The cross-correlation function $\rho_{ij}(\tau)$ was found by correlating the blocks of data $F_i(t)$ and $F_j(t)$ from the two fields of view i and j respectively using the lagged products method defined by the following equation

$$\rho_{ij}(\tau) = \frac{F_i(t) \cdot F_j(t+\tau)}{\left(\Sigma F_i(t)^2 \cdot \Sigma F_j(t)^2\right)^{\frac{1}{2}}} \,. \qquad (4.1)$$

It is then necessary to find the value of the time lag τ defined as t_{ij} when $\rho_{ij}(\tau)$ is a maximum. Since the width of the cross-correlation function $\rho_{ij}(\tau)$ was large compared to the shift of the maximum value of $\rho_{ij}(\tau)$ from the zero lag point ($\tau = 0$), a fourth order polynomial was fitted to $\rho_{ij}(\tau)$ adjacent to $\tau = 0$. The time displacement t_{ij} was then found by differentiating the polynomial and finding the appropriate numerical root using the Newton-Raphson iterative method.

If (x_i, y_i) and (x_j, y_j) are the horizontal co-ordinates of the two fields of view i, j then the polar difference vectors d_{ij}, θ_{ij} between the two fields are defined as follows

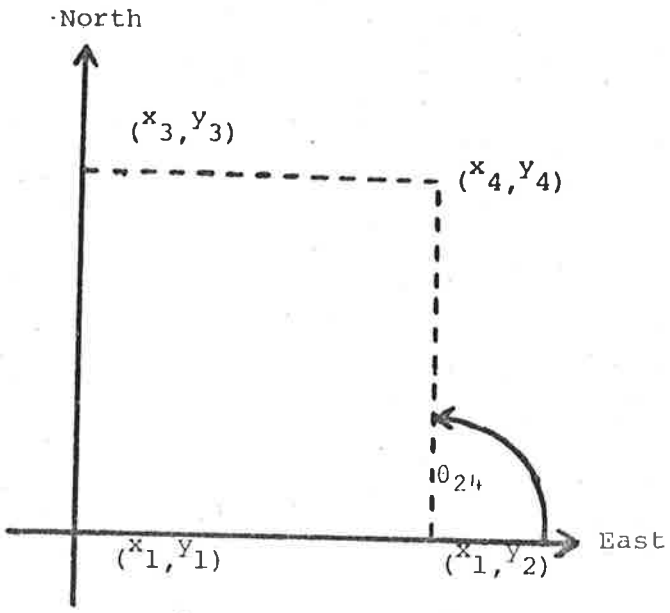

Figure 4.1a Configuration of the horizontal coordinates of the four fields of view.

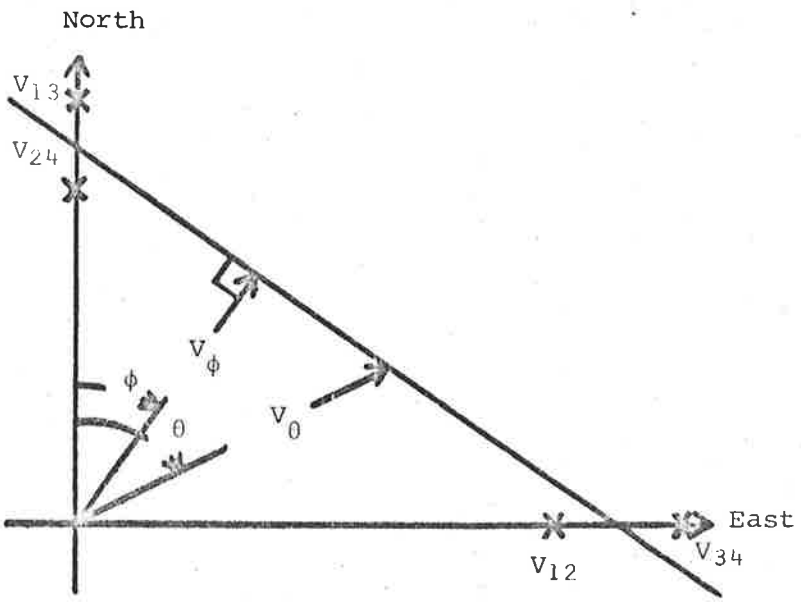

Figure 4.1b Geometric relation of the drift velocity (V_ϕ, ϕ) to the best fit straight line for the trace velocities V_{12}, V_{13}, V_{24}, V_{34}. Also included is a trace velocity (V_θ, θ).

$$d_{ij} = \left[(x_j - x_i)^2 + (y_j - y_i)^2\right]^{\frac{1}{2}} \tag{4.2a}$$

$$\theta_{ij} = \arctan\left(-\frac{x_j - x_i}{y_j - y_i}\right) . \tag{4.2b}$$

A value for the trace velocity V_{ij} along a line joining two fields is then given by

$$V_{ij} = \left(\frac{d_{ij}}{t_{ij}}, \theta_{ij}\right) . \tag{4.3}$$

Although four points of observations allow six cross-correlation combinations and hence six trace velocity values, there are only 3 degrees of freedom and hence some values can be considered redundant. Use of adjacent points to obtain four trace velocities, which according to the configuration in Figure 4.1a would be V_{12}, V_{13}, V_{24}, V_{34} result in each point having equal weight and no data loss. The drift velicity V_ϕ, as shown in Figure 4.1b, is now given by the perpendicular from the origin to a best-fit straight line of the four points defined by the trace velocities. The direction of drift ϕ is measured clockwise from the North. However, one needs to be wary in the choice of the method used in the line-fitting procedure.

Equation (3.2) may be written in the form

$$\sigma V_{ij} = \frac{\sigma t_{ij}\, d_{ij}}{t_{ij}^2} \tag{4.4}$$

Assuming that the standard error σt_{ij} of the lag time t_{ij} is independent of the value of t_{ij}, the standard error σv_{ij} in the trace velocity V_{ij} will be large for small time lags.

Use can be made of the relation between the drift velocity V_ϕ and some trace velocity V_θ. From the geometry in Figure 4.1b it can be shown that

$$\frac{1}{V_\theta} = \frac{1}{V_\phi} \cos(\theta-\phi) \ . \qquad (4.5)$$

The reciprocal of the trace velocity $\frac{1}{V_{ij}} = \frac{t_{ij}}{d_{ij}}$ and hence the standard error $\sigma\left(\frac{1}{V_{ij}}\right) = \frac{\sigma t_{ij}}{d_{ij}}$. The fitting of the trace velocities in "reciprocal mode" to the function defined by equation (4.5) is reasonable since the standard error $\sigma\left(\frac{1}{V_{ij}}\right)$ is then independent of the value of t_{ij} . It must be pointed out that it is still assumed that σt_{ij} is independent of the value of t_{ij} and also of the direction of the trace velocity in relation to the drift velocity.

Subroutine Curfit (Bevington, p. 237), which makes a least squares fit to non-linear functions, was used to fit the four trace velocities V_{ij} to the function defined by equation (4.5) thus providing estimates to the magnitude of the drift velocity V_ϕ and its direction ϕ. This subroutine also provides the standard errors in the output parameters $\left(\frac{1}{V_\phi}, \phi\right)$ and these along with consistancy in the lag times were used in assessing the "genuineness" of the drift velocity. Velocities for which the ratio of the standard deviation of the velocity magnitude to the velocity magnitude exceeded 0.2 were, in the main, discarded and this generally corresponded to regions of the data where the amplitude of the short period structure were small.

4.1.2 DETERMINATION OF THE POWER SPECTRA

The power spectra of the 557.7nm (OI) intensity fluctuations are presented in this chapter and the next. In this chapter the power spectra were calculated from data blocks of 512 points corresponding to 95 minutes

of record length therefore providing a frequency resolution of 1.77×10^{-4} Hz.

The Discrete Fourier Transform was used to estimate the power spectra and details of this technique may be found at numerous places in the literature, e.g. Hunich and Clay (1968). In outline the mean of the data was set to zero, linear trends were removed and the data was then treated with a Hanning Window to remove spectral leakage. The Fourier Transform was calculated using FFT and the sum of the squares of the real and imaginary Fourier components provided the spectral power estimates at that particular frequency.

The spectral power component due to Poisson-type noise fluctuations can also be estimated. In the relation

$$y_n' = \sum_n y_n \exp \frac{(2\pi i n n')}{N} , \qquad (4.6)$$

y_n represents a data point which has variance p, y_n' represents a discrete non-normalized Fourier transform of data y_n and N is the number of data points.

As the mean value of y_n is set to zero

$$\sum_n y_n^2 = Np . \qquad (4.7)$$

Also the expected value of the spectral power $|y_n'|^2$ according to equation (4.6) is given by

$$|y_n'|^2 = \sum_n \sum_k y_n \, y_k = Np \qquad (4.8)$$

since

$$\sum_{\substack{n \\ n \neq k}} \sum_k y_n \, y_k = 0 .$$

From equation (4.8) and estimates of the standard deviations of the

data, the contribution of "white noise" due to photon noise was of the order of 10^{-2} on the scale used in the power spectra diagrams appearing in this chapter.

The standard deviation of each spectral power estimate is comparable to the value of the spectral power estimate itself. This results in the power spectra being noisy for individual records and to reduce this, the power spectra obtained from records of each of the four fields of view were averaged together at each frequency. However the reduction in the standard deviation will be something less than a factor of 2 since the records are highly correlated. This was the limit of smoothing for the power spectra of individual records to be given in section 4.2 but the degree of smoothing for the mean nightly power spectra to be reported in section 4.3 will be greater.

Also there were occasions when it was necessary to determine whether structure in a power spectrum was due to variations in the airglow intensity at that frequency or due to noise. The mean value of the spectral peak was determined and since spectral values are very poorly correlated (Buckley, 1971), the standard deviation in this region was determined from

$$\sigma s^2 \approx \frac{1}{N} \sum_{K=K'}^{K'+N} \left(S_{FK}-S_{FK+1}\right)^2 \qquad (4.9)$$

where S_{FK} and S_{FK+1} are adjacent spectral estimates at frequences $\frac{K}{T}$, $\frac{K+1}{T}$ respectively with T the record length and N the number of spectral values in the region of interest. For equation (4.9) to give a reasonable estimate to σs where the contribution due to genuine structure is small, one must assume that the width of the spectral peak is several times that of the frequency resolution. In any case, contributions other than noise can only decrease the estimate of the standard deviation. The criterion

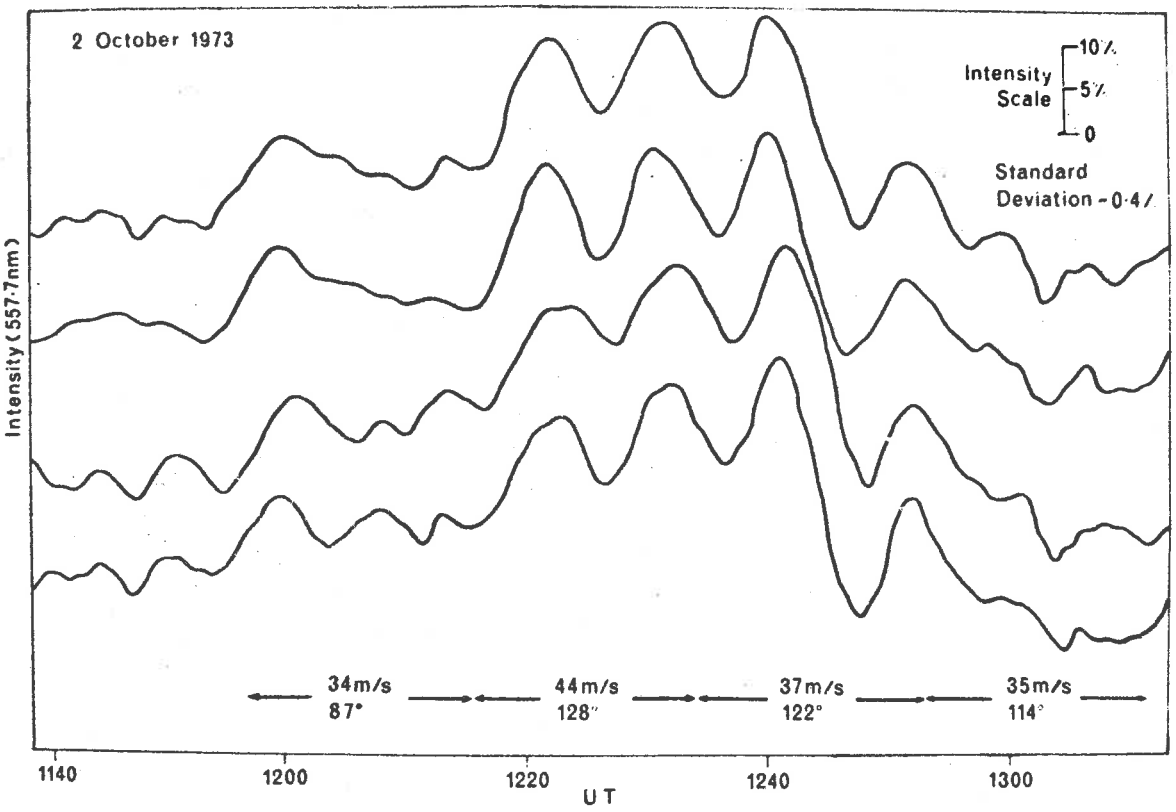

Figure 4.2a Intensity variations of the λ557.7 nm [OI] airglow observed on 2 October 1973 from 1138 UT to 1314 UT and associated drift velocities.

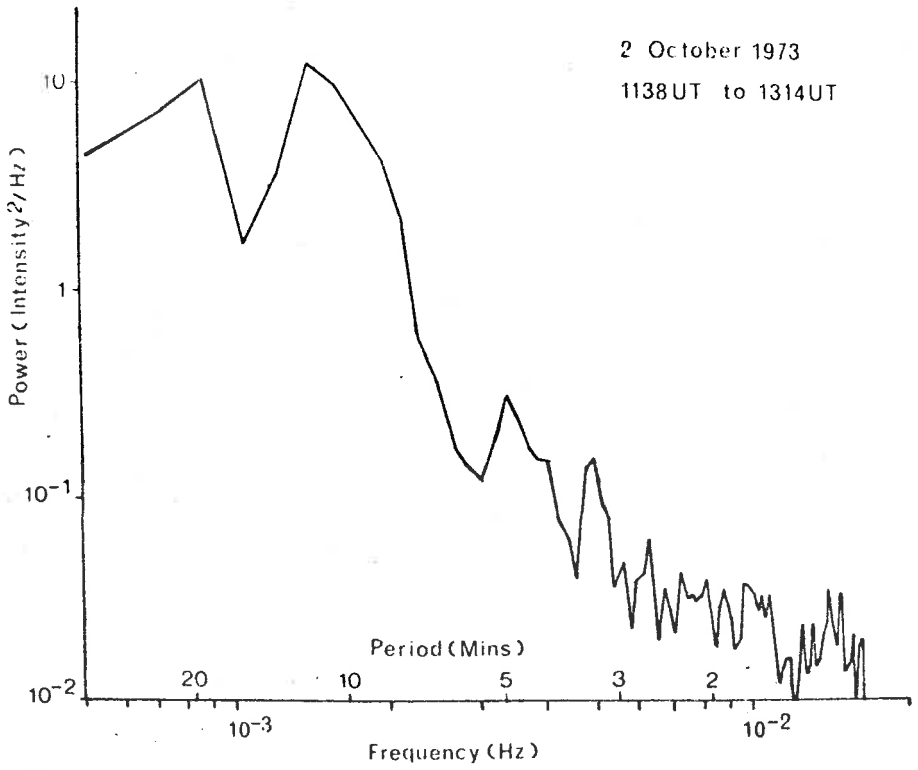

Figure 4.2b Power Spectrum of the intensity variations shown in Figure 4.2a

adopted to establish the "genuineness" of the peak was that if the spectral peak exceeds the mean value by more than 3 standard deviations and adjacent values of S_{FK} exceed the mean by 1 to 2 standard deviations, then it was inferred that the spectral peak had a high probability of being due to observed structure in the airglow.

The units of the spectral values will be $(\text{intensity})^2$ per Hertz where the units of intensity remain arbitrary.

4.2 Some Intensity Variations from the 4-Field Photometer

In this section, examples of short period intensity structure from the 4-field Photometer, along with their respective drift velocities will be presented. Using the criterion outlined in section 4.1.1, the velocity for certain lengths of data will be omitted where it is assessed to be of doubtful reliability. The intensity profiles have been smoothed to remove high frequency noise and the high frequency cut-off is around 44 seconds. The standard deviation will be given and this was estimated from the R.M.S. value of the deviations of the data points from the fitted curve with a factor of 2 due to smoothing (the sampling rate was 11 seconds). The power spectrum of these intensity variations will be also given.

4.2.1 VARIATIONS OF 2 October, 1973, 1138 UT to 1314 UT

Figures 4.2a and 4.2b provide the intensity variations along with the respective drift velocities and the power spectrum of variations observed on the 2 October, 1973 for the time interval 1138 UT to 1314 UT. A significant feature in Figure 4.2a, chacterized by a periodic variation extending over 4 cycles, a period of about 11 minutes and a relative amplitude of 5%, occurred between 1215 UT and 1255 UT. The drift velocity of this wave was 44 m/s in a direction of 128°. Other spectral features appearing in Figure 4.2b are spectral peaks at 3½, 5 and 19 minutes.

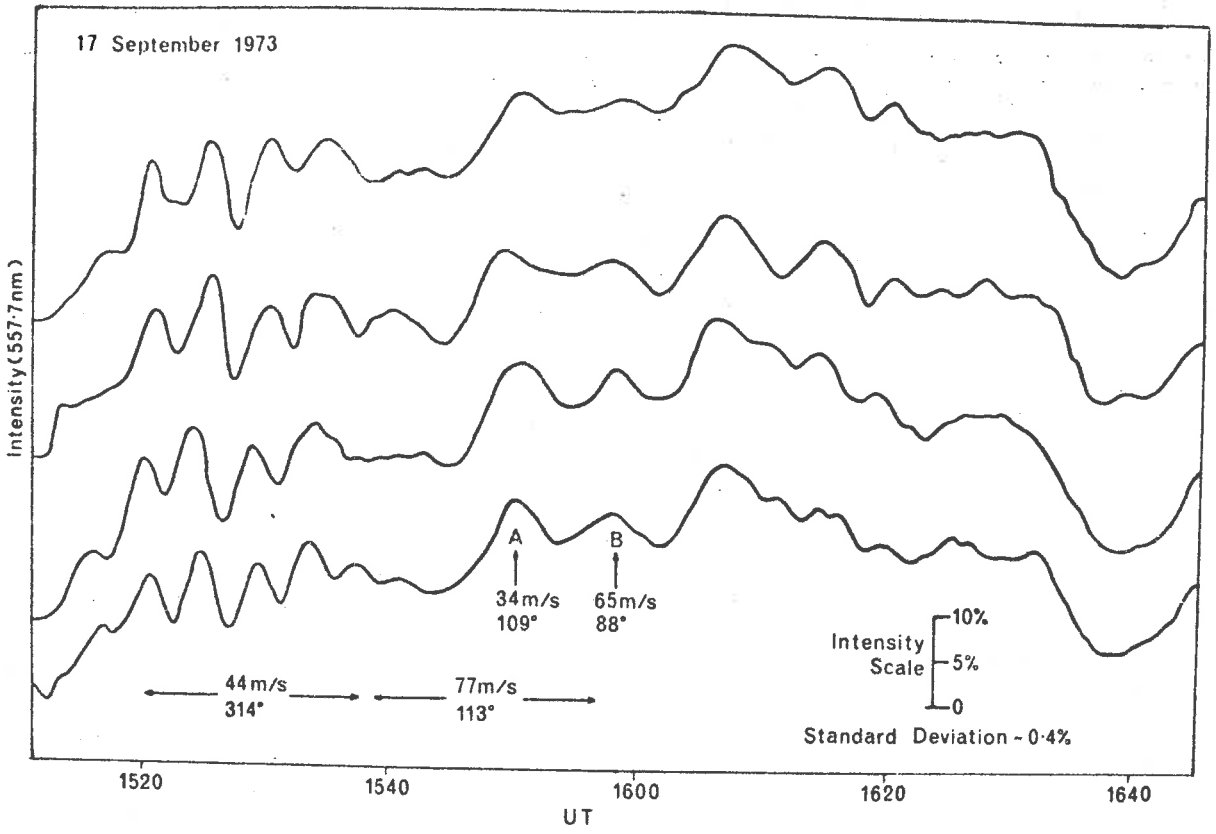

Figure 4.3a Intensity variations of the λ557.7 nm [OI] airglow observed on 17 September 1973 for 1512 UT to 1647 UT and associated drift velocities.

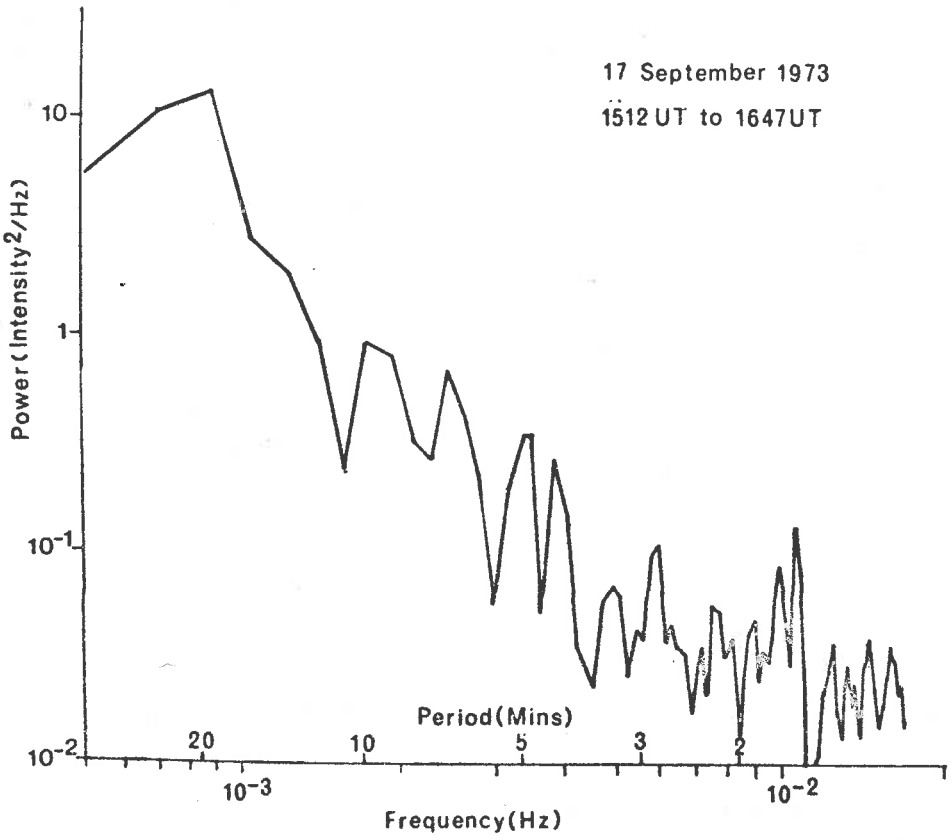

Figure 4.3b Power Spectrum of the intensity variations shown in Figure 4.3a

4.2.2 VARIATIONS FOR 17 September, 1973, 1512 UT to 1637 UT

Figures 4.3a and 4.3b provide the intensity variations with drift velocities and the power spectrum of the variations observed on 17 September, 1973 during the interval 1512 UT to 1647 UT.

Of interest in Figure 4.3a are two periodic type structures whose velocities are in almost opposite directions. In the interval 1519 UT to 1539 UT a wave, periodic over 5 cycles with a period of 5 minutes and a relative amplitude of 3%, had a horizontal trace velocity of 44 ms^{-1} towards the north-west. The velocity in the interval 1538 UT to 1558 UT was 77 ms^{-1} in an easterly direction. By finding the time lags between individual features in each of the 4-fields, it is also possible to estimate the drift velocity, and the velocities at 1549 UT and 1559 UT (pts A and B in Figure 4.3a) confirmed the eastward drift of this structure. The time lags of 1605 UT to 1647 UT were small and inconsistent suggesting that the intensity variations at this time may have been formed from the superposition of 2 or more structures travelling in different directions.

There are two interesting features in the power spectrum given by Figure 4.3b which are not obviously apparent in intensity variations in Figure 4.3a. A significant spectral peak occurs at a period of 19 minutes and a close examination of the intensity record in Figure 4.3a reveals that a wave of low amplitudes (1% to 2% relative amplitude) with a period of approximately 19 minutes was present throughout the length of the record. Using the criteria outlined in Section 4.1.2 a significant spectral peak also appears at a frequency of 1.05×10^{-2} Hz (95 second period).

4.2.3 VARIATIONS FOR 28 September, 1973, 1145 UT to 1320 UT

Intensity variations with corresponding drift velocities and the

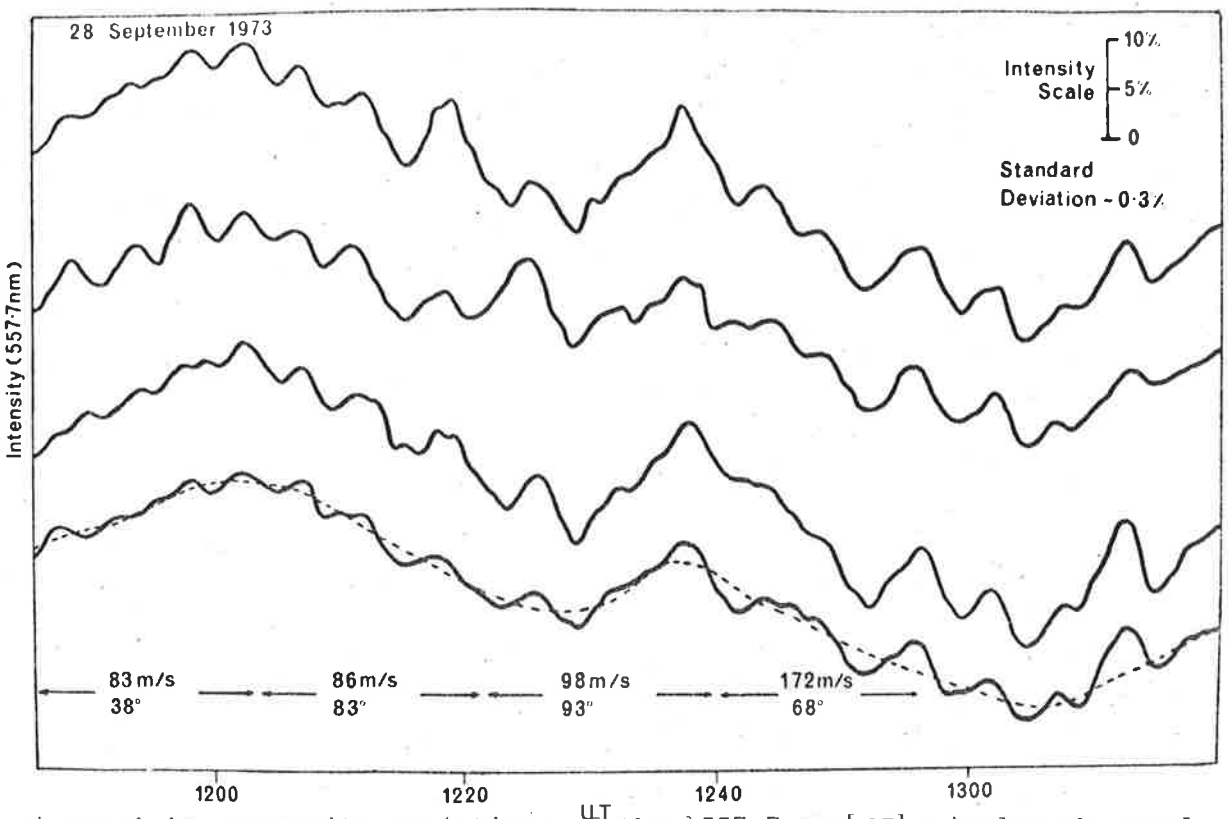

Figure 4.4a Intensity variations of the λ557.7 nm [OI] airglow observed on 28 September 1973 for 1145 UT to 1320 UT and associated drift velocities.

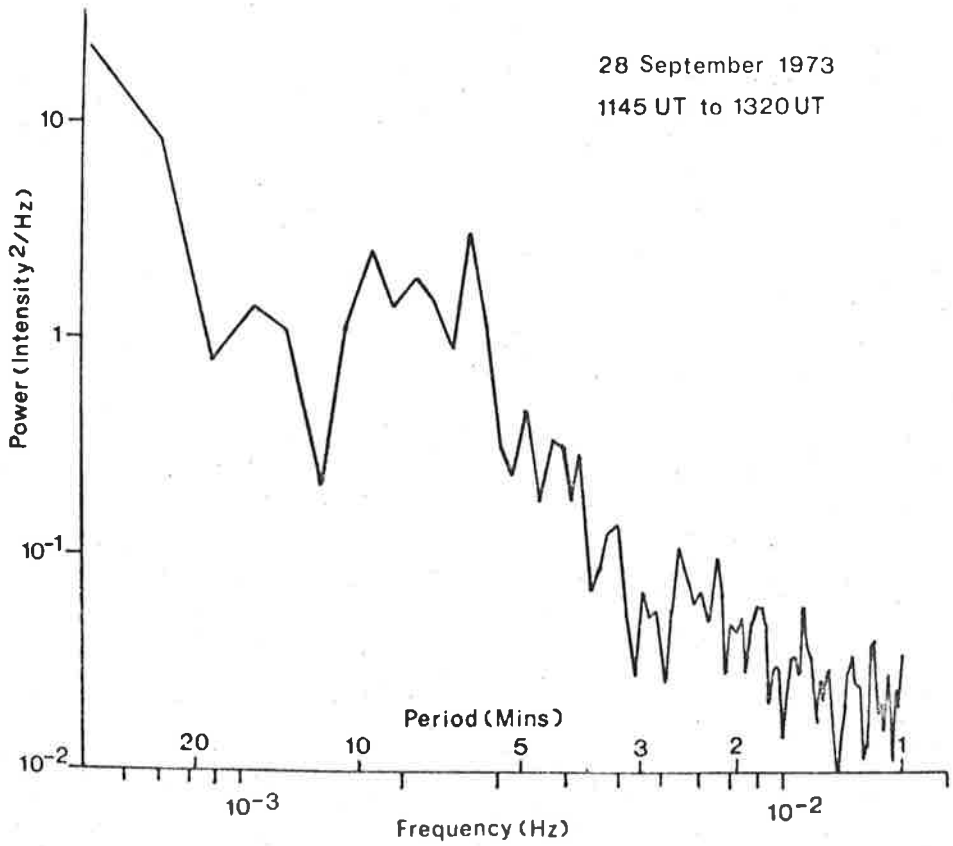

Figure 4.4b Power Spectrum of the intensity variations shown in Figure 4.4a

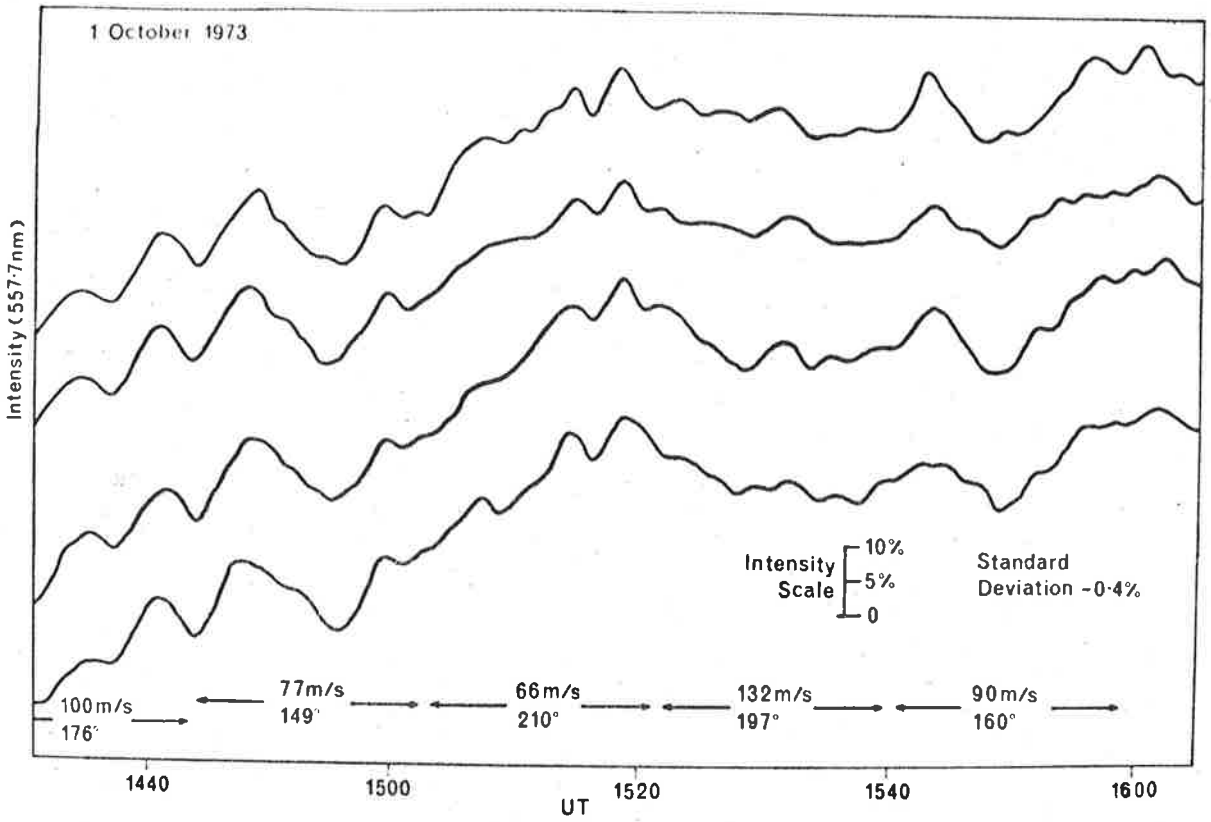

Figure 4.5a Intensity variations of the λ557.7 nm [OI] airglow observed on 1 October 1973 for 1430 UT to 1605 UT and associated drift velocities.

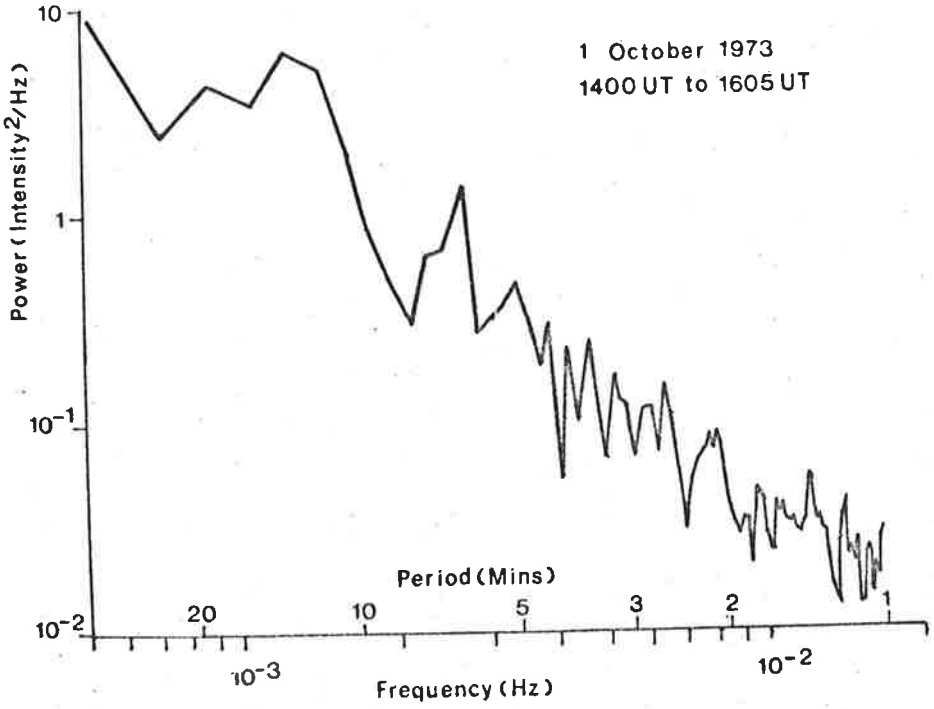

Figure 4.5b Power Spectrum of the intensity variations shown in Figure 4.5a

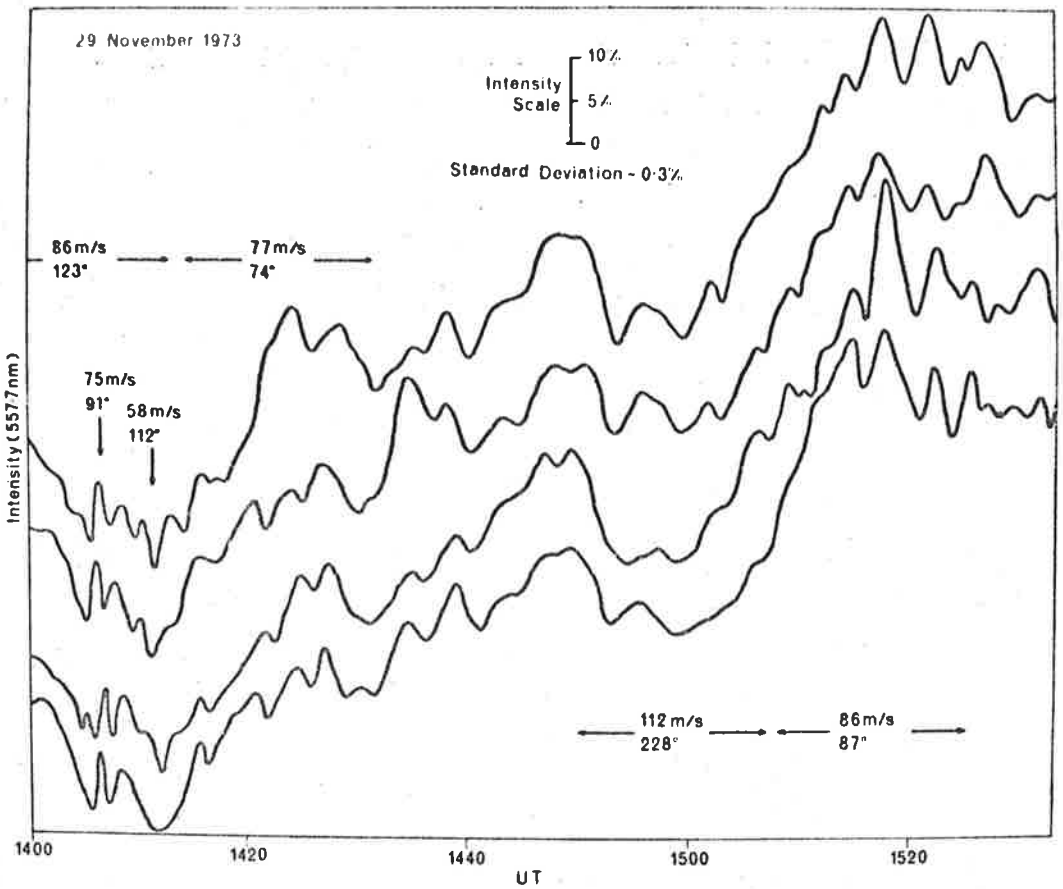

Figure 4.6a Intensity variations of the λ557.7 nm airglow observed on 29 November 1973 from 1400 UT to 1435 UT and associated drift velocities.

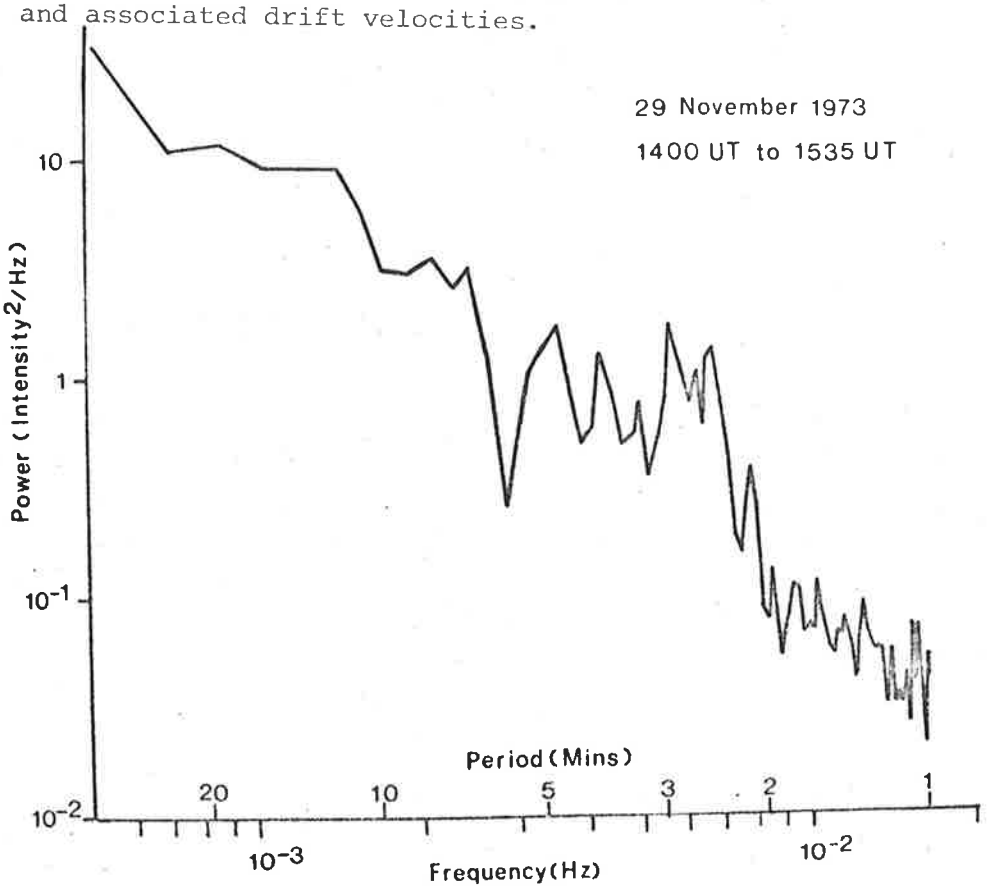

Figure 4.6b Power Spectrum of the intensity variations shown in Figure 4.6a

power spectrum for 28 September, 1973, 1145 UT to 1320 UT are given in Figures 4.4a and 4.4b respectively. The drift velocities in this interval are predominantly in an eastward direction. Much of the spectral power is concentrated in a region corresponding to periods between 6 minutes and 11 minutes. As can be seen in the intensity trace this structure is superimposed on a longer period structure with a period of around 45 minutes.

4.2.4 VARIATIONS OF 1 October, 1973, 1430 UT to 1605 UT

Intensity variations with drift velocities and the power spectrum for the above time interval are given in Figures 4.5a and 4.5b. The drift velocities are in a generally southward direction. A broad spectral peak is centred at a period of 14 minutes and another statistically significant peak occurs at 7 minutes.

4.2.5 VARIATIONS ON 29 November, 1973, 1400 UT to 1535 UT

Intensity variations with drift velocities and the power spectrum of the intensity variations during this interval are presented in Figures 4.6a and 4.6b. The drift velocities were in a predominantly westward direction although in the interval 1451 UT to 1509 UT, a drift velocity towards the north-east was observed. Spectrally the intensity record is composed of a very long period trend on which a wave of period of around 55 minutes was superimposed. On this, short period fluctuations with periods extending to nearly 2 minutes were in turn superimposed.

4.3 Drift Velocities of 557.7nm(OI) Intensity Variations

Drift velocities obtained on six nights using the 4-field Photometer were plotted in the form of scatter plots and are presented in Figures 4.7 to 4.12. Also on two nights (28 September, 1973 and 1 October, 1973) wind velocities, found by measuring the Doppler shift of the 557.7nm (OI)

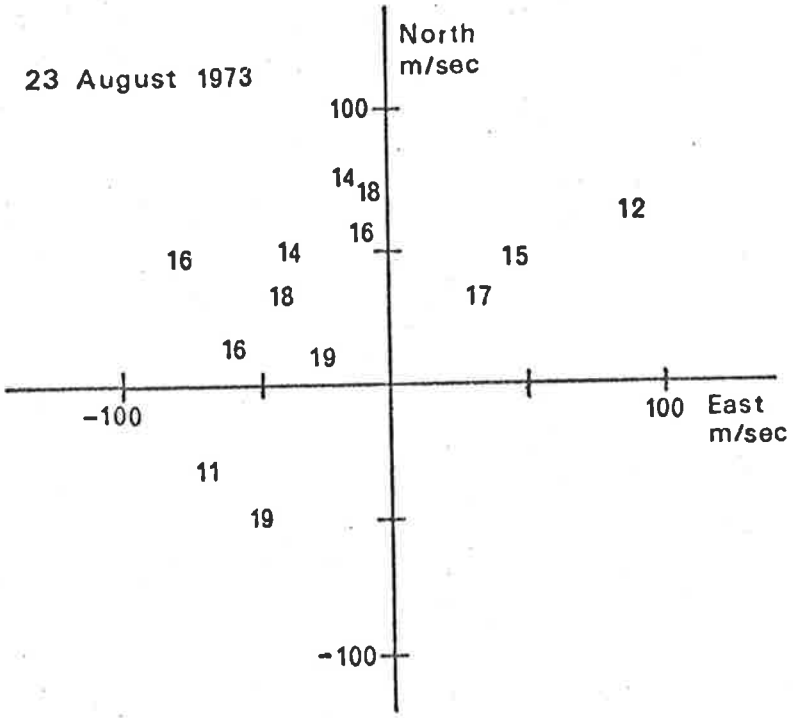

Figure 4.7 Scatter plot of the [OI] λ 557.7 nm drift velocities observed on the 23 August 1973. The time in UT(hours) is indicated.

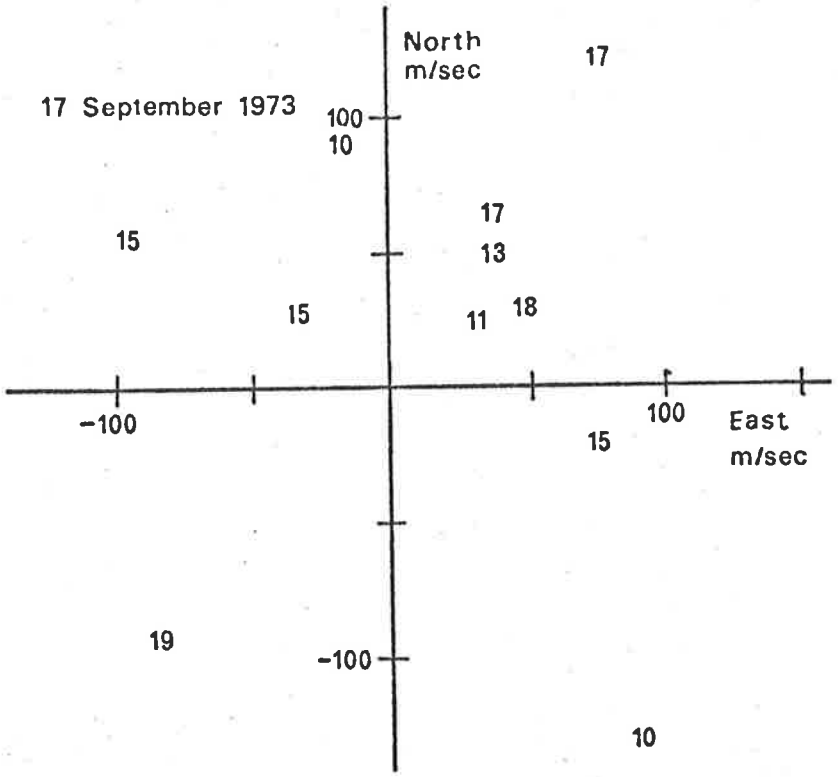

Figure 4.8 Scatter plot of the [OI] λ 557,7 nm drift velocities observed on the 17 September 1973. The time in UT (hours) is indicated.

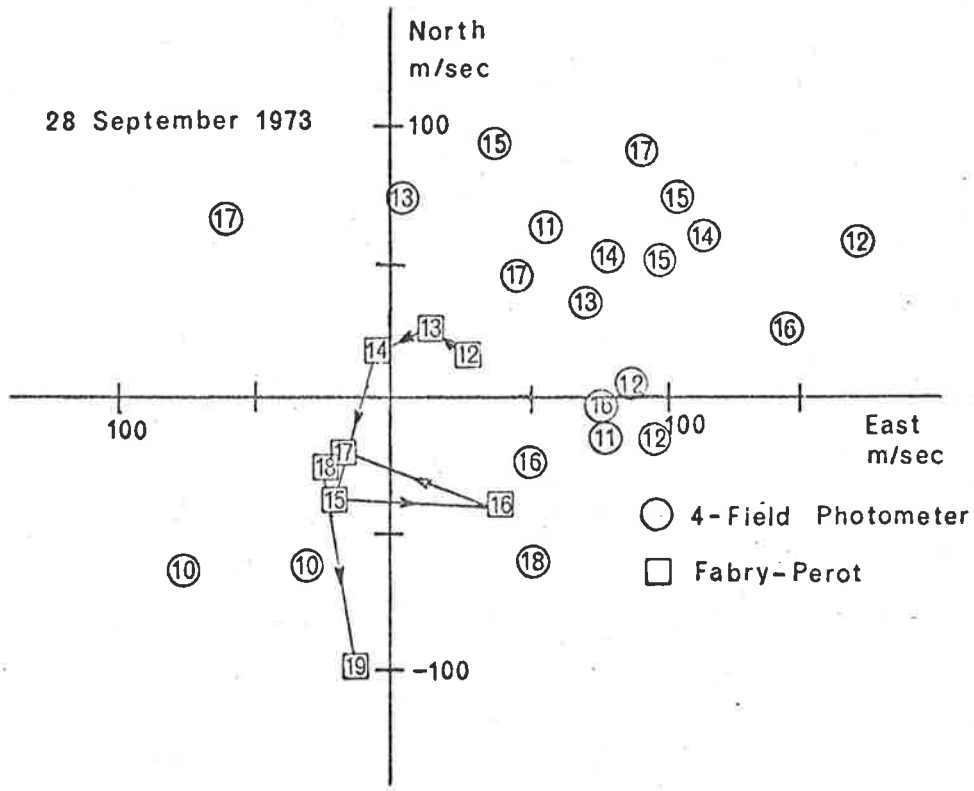

Figure 4.9 Scatter plot of the [OI] λ 557.7 nm drift velocities and the wind velocities found by measuring the Doppler shift of the [OI] λ 557.7 nm line using a Fabry-Perot Interferometer. The time (UT in hours) is indicated.

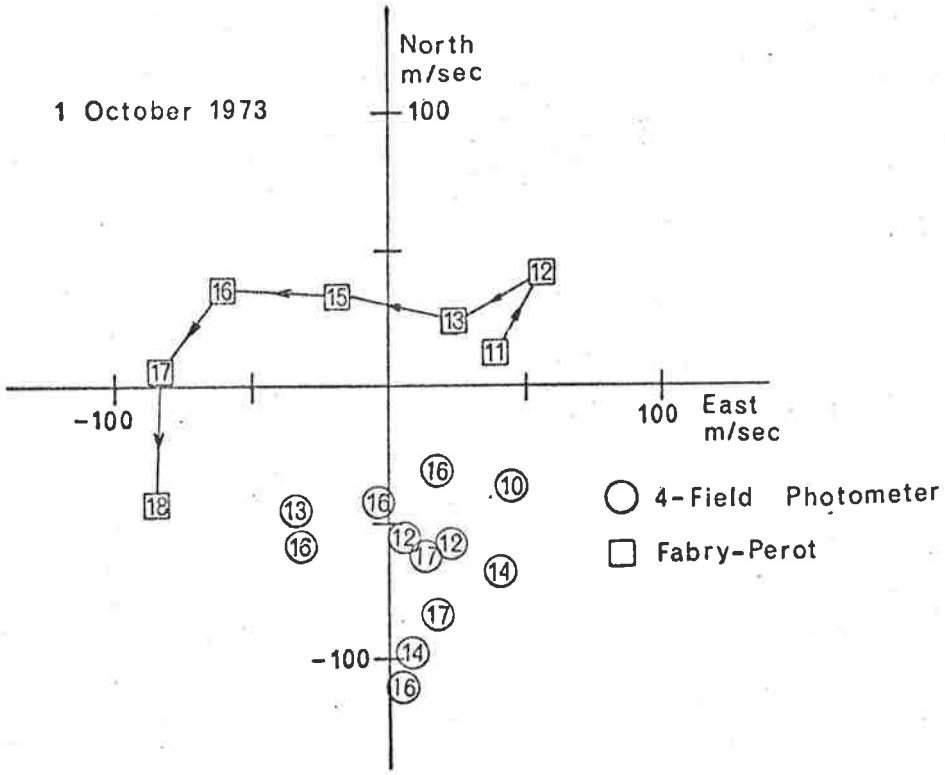

Figure 4.10 Scatter plot of the [OI] λ 557.7 nm drift velocities and the wind velocities found by measuring the Doppler shift of the [OI] λ 557.7 nm line using a Fabry-Perot Interferometer. The time (UT in hours) is indicated.

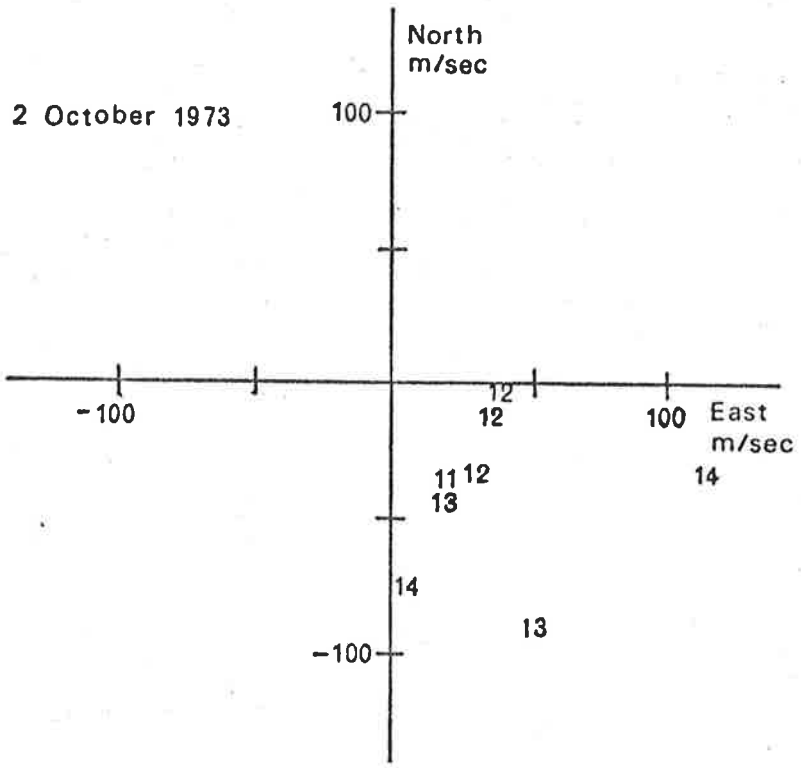

Figure 4.11 Plot of [OI] λ 557.7 nm drift velocities observed on 20 October 1973.

The time (UT in hours) is indicated.

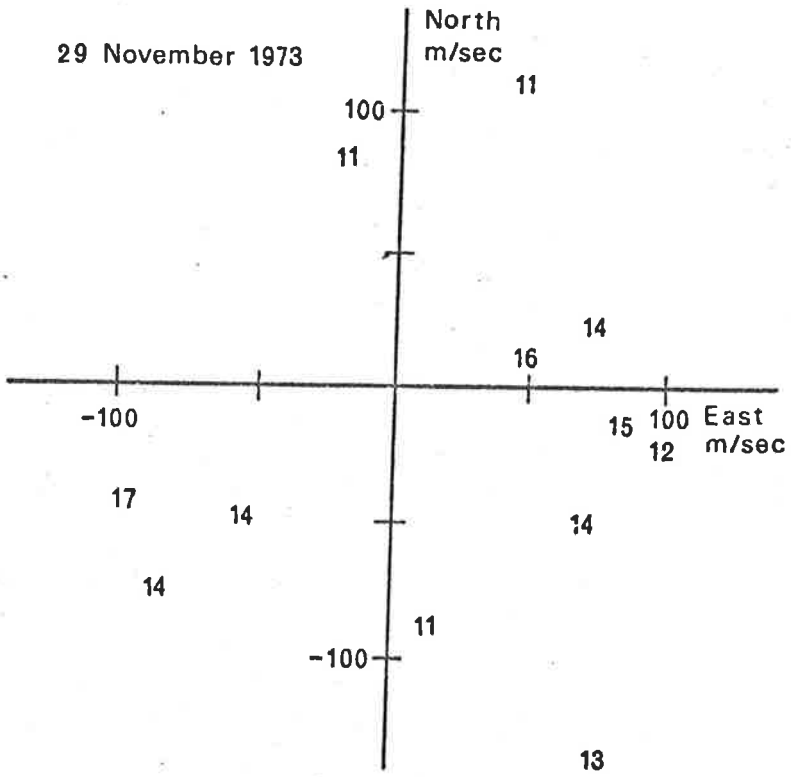

Figure 4.12 Plot of [OI] λ 557.7 nm drift velocities observed on 29 November 1973.

The time (UT in hours) is indicated.

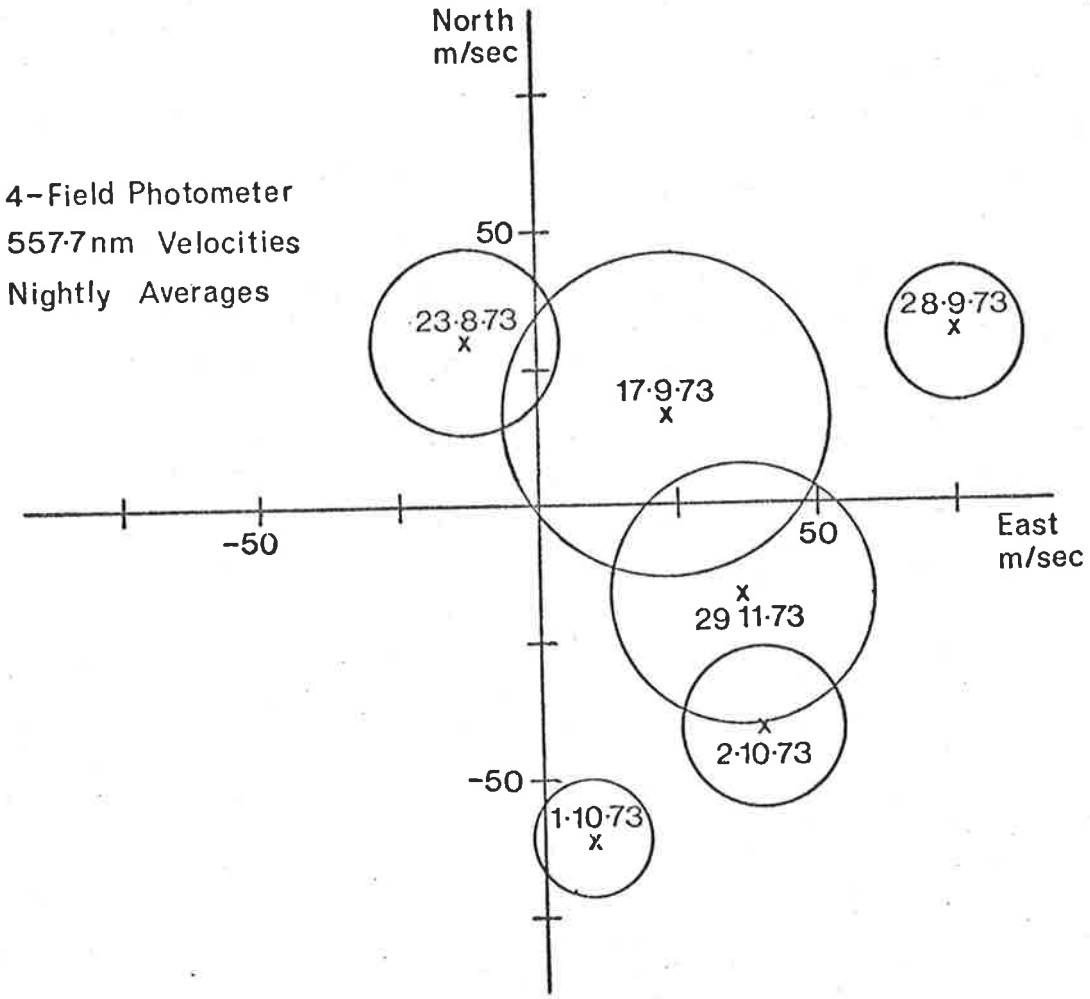

Figure 4.13 Plot of the mean drift velocity and the standard error in the drift velocity for each night of observation.

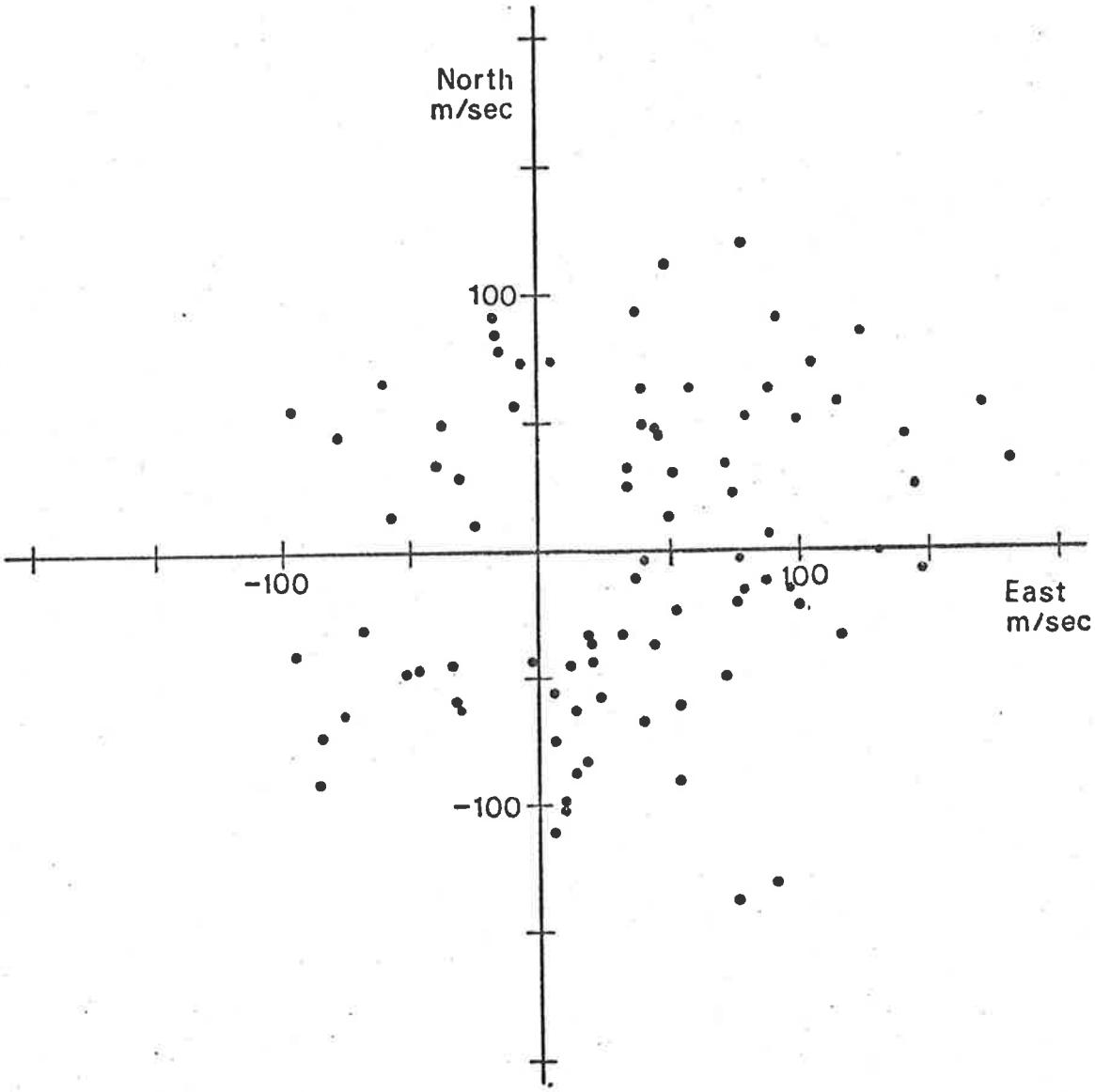

Figure 4.14 Scatter plot of the drift velocities of the [OI] λ 557.7 nm variations observed on the 6 nights.

line using a Fabray-Perot Interferometer, were available, and the hourly average winds were plotted in Figures 4.9 and 4.10.

The general pattern of the wind is an anticlockwise rotation in agreement with ionospheric drift velocities at that height which have been obtained by Stubbs (1973). There is no tendency for the 557.7nm irregularities to "drift" along with the background wind and in fact there appears to be little correlation between the drift velocities and the winds at that altitude. Any trends with time of the drift velocities are also not apparent.

However, there is a tendency on all nights for the drift velocities to be anisotropic. This has been summarized in Figure 4.13 where the mean value of the drift velocity on each night has been plotted. The radius r of the circle around each value was calculated using the relation

$$r = \left[\frac{1}{N(N-1)} \sum_{i=1}^{N} (u_i-\bar{u})^2+(v_i-\bar{v})^2\right]^{\frac{1}{2}} \qquad (4.10)$$

where $(\bar{u},\bar{v})$ are the zonal and meridional components of the mean velocity, (u_i,v_i) are the respective components of the individual observations and N is the number of observations on that night. Statistically, this circle represents the magnitude of the standard error in the mean value of the velocity. On the 17 September, 1973, the degree of anisotropy is small, but on all other nights it is statistically significant.

Finally, Figure 4.14 consists of a scatter plot of the drift velocities obtained on all 6 nights. The mean drift speed was 32 ms^{-1} in a direction 94° i.e. towards the east.

4.4 Spectral Power of 557.7nm (OI) Intensities

Individual power spectra from five nights obtained in a manner outlined in Section 4.2.2 were averaged together to give a mean nightly

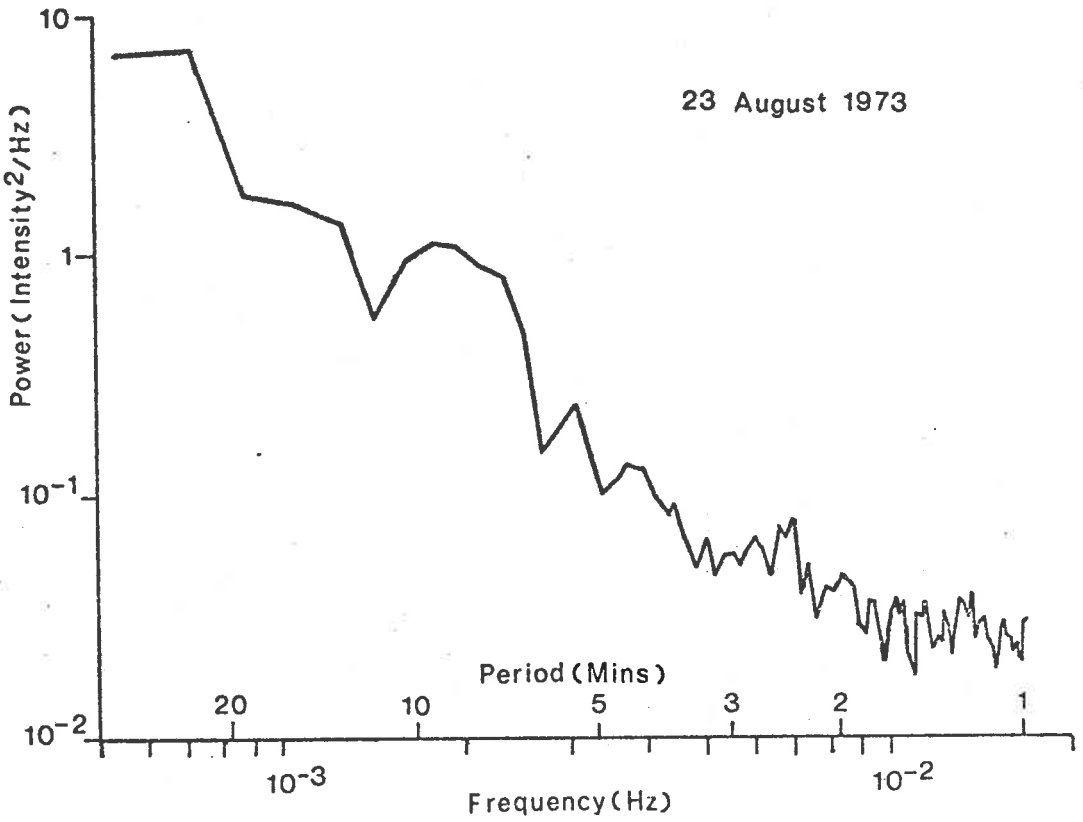

Figure 4.15 Mean power spectrum of the [OI] λ 557.7 nm intensity variations observed on 23 August 1973.

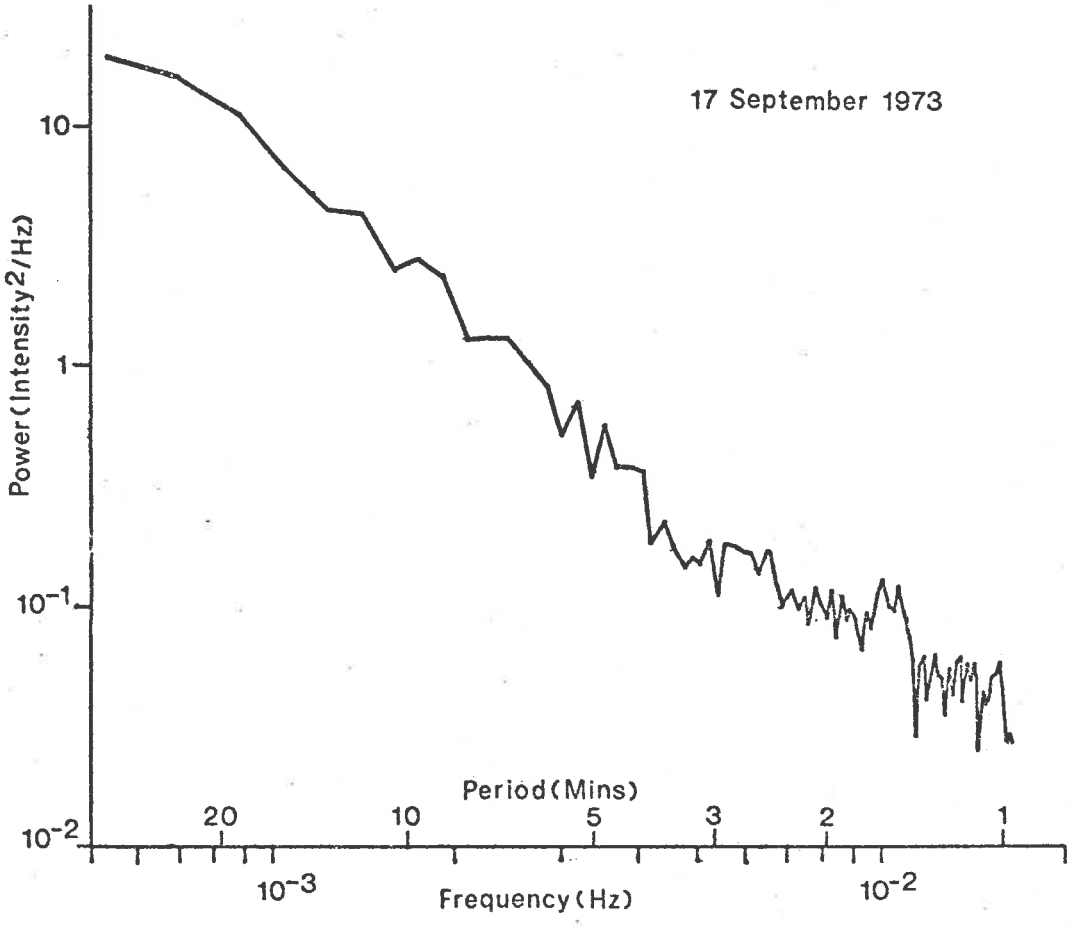

Figure 4.16 Mean power spectrum of the [OI] λ 557.7 nm intensity variations observed on 17 September 1973.

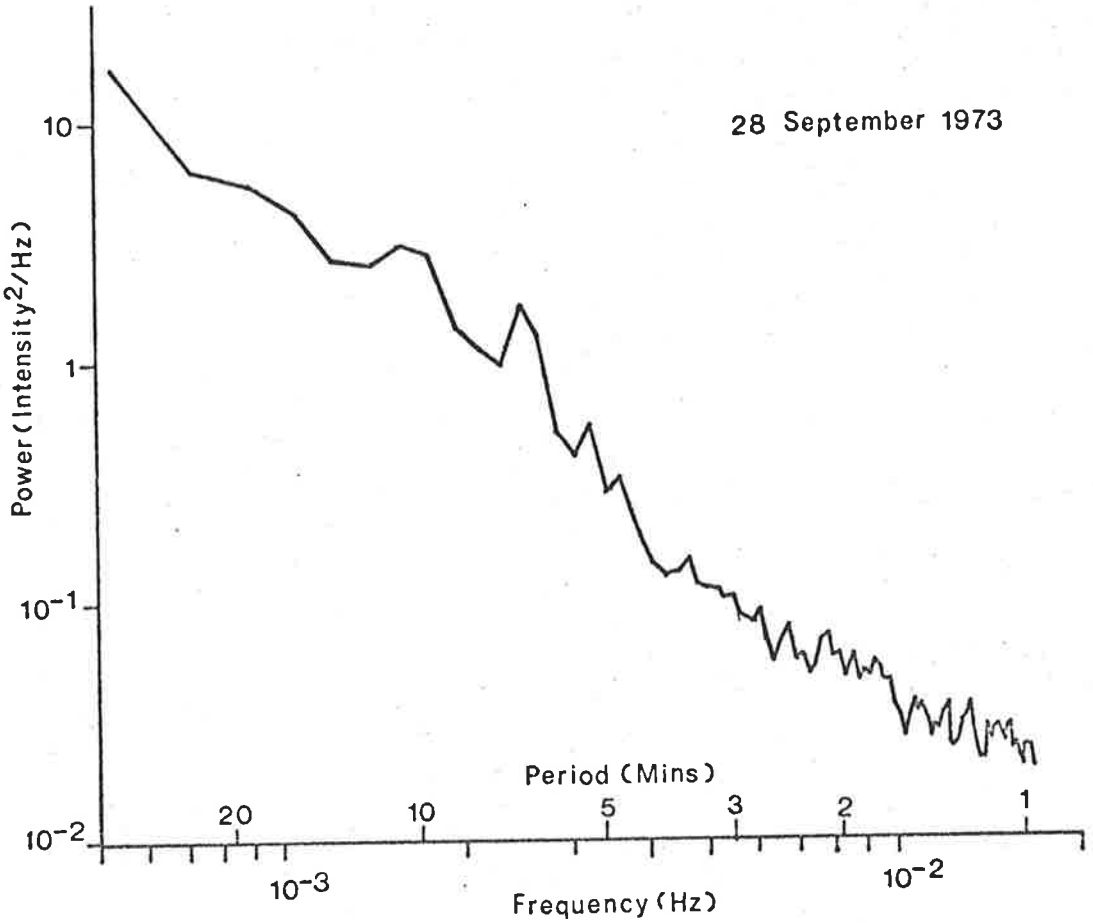

Figure 4.17 Mean nightly power spectrum of the [OI] λ 557.7 nm intensity variations observed on 28 September 1973.

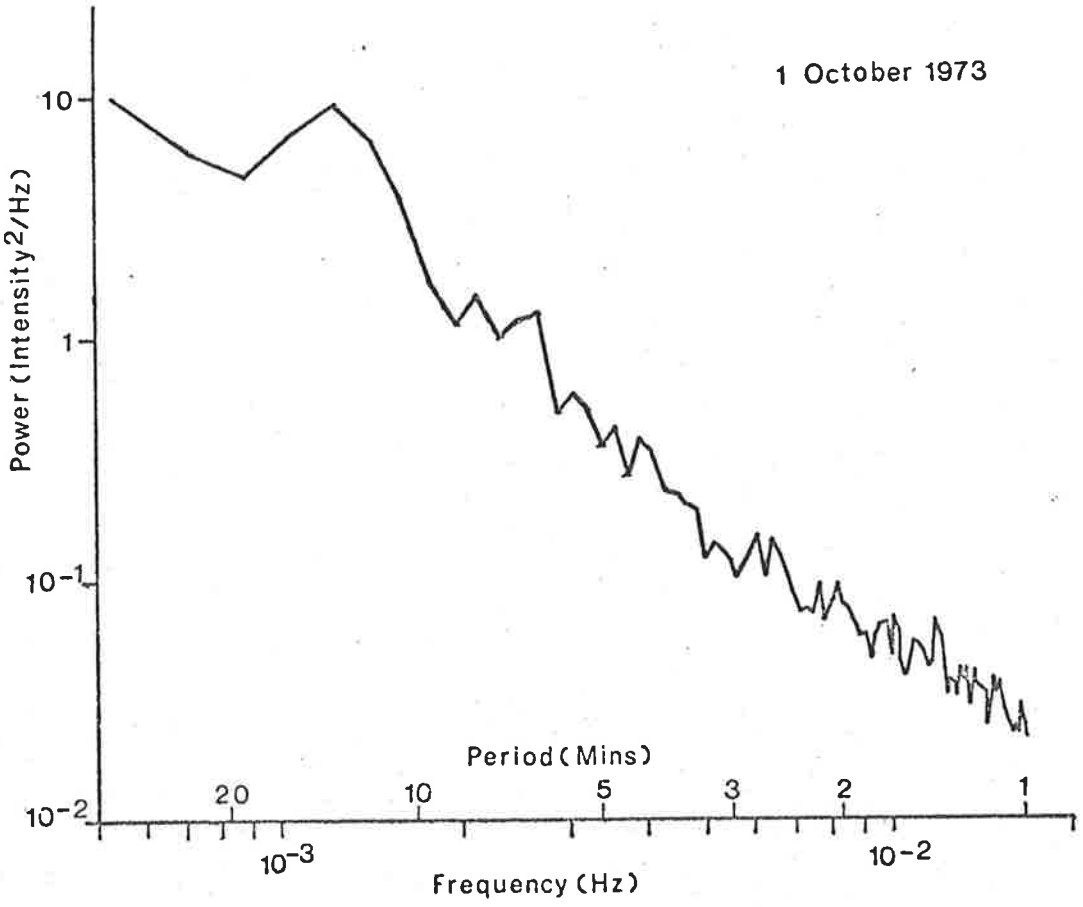

Figure 4.18 Mean nightly power spectrum of the [OI] λ 557.7 nm intensity variations observed on 1 October 1973.

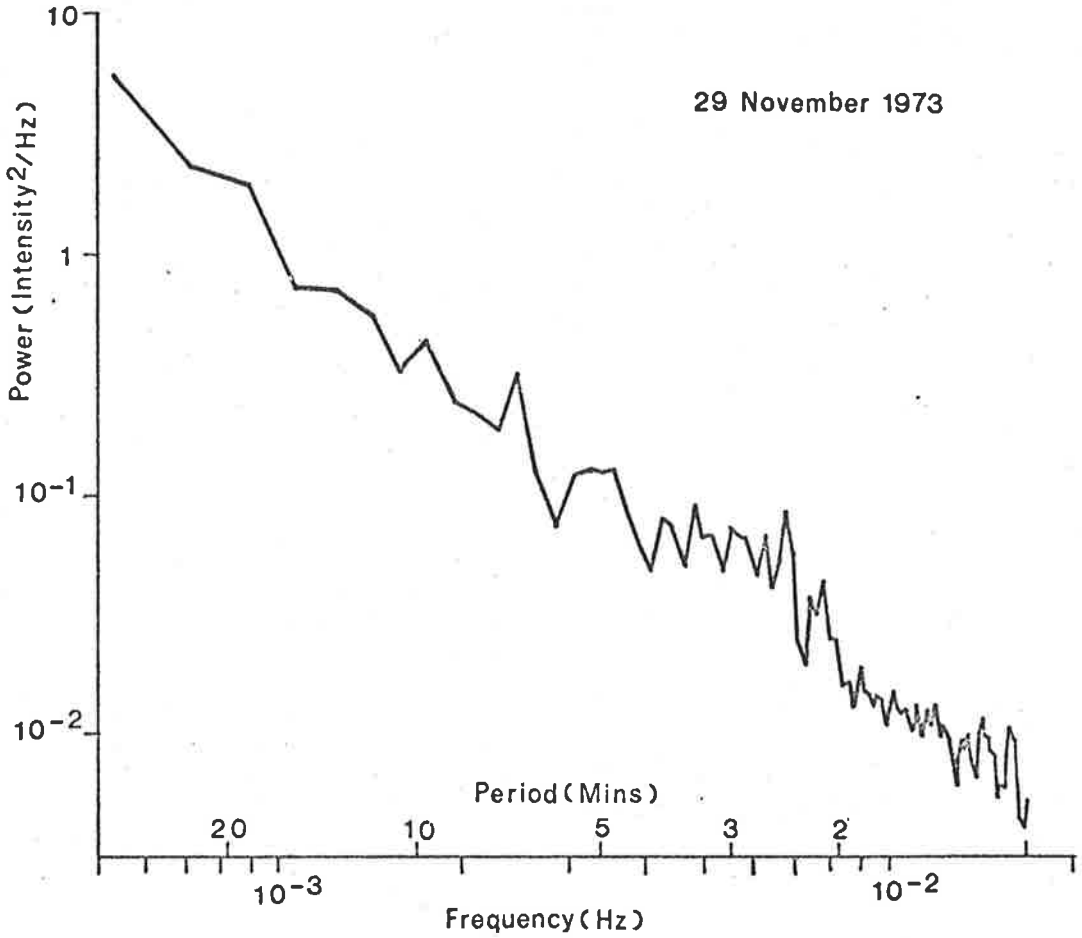

Figure 4.19 Mean nightly power spectrum of the [O I] λ 557.7 nm intensity variations observed on 29 November 1973.

power spectrum. These spectra obtained on 23 August 1973, 17 and 28 September, 1973, 1 October, 1973 and 29 November, 1973 are presented in Figures 4.15 and 4.19.

The fall-off of spectral power with frequency for each of the power spectra has been summarized in Table 4.1, where n is given by relation $P(f) \propto f^{-n}$, where P(f) is the spectral power at some frequency f. A general trend seems to be a change in fall-off in spectral power of roughly $f^{-2.2}$, at frequencies less than about 4×10^{-3} Hz to something around $f^{-1.3}$ for frequencies greater than this. On 29 November, 1973 there is a significant spectral power contribution extending to nearly 8×10^{-2} Hz. On 28 September, 1973 the fall-off between 5×10^{-3} Hz and 4×10^{-2} Hz is divided into two components.

On all nights there may be some spectral power at frequencies $> 4 \times 10^{-3}$ Hz for several reasons. White noise would exhibit a spectral power characteristic of f^{o} whereas it is typically f^{-1}. Also the spectral power at 4×10^{-3} Hz is an order of magnitude greater than the noise power estimate. (In Section 4.1.2 the spectral noise power was estimated to be $\sim 10^{-2}$ on the scale used in the Figures.) Further on the two nights 23 August, 1973 and 17 September, 1973 where the noise was greater than the other nights and therefore was greater than 10^{-2}, the Power Spectra flattens out at frequencies greater than 10^{-2} Hz suggesting that the spectral power has decreased to a limiting background level.

On the debit side, the field stop positions in the photometer were not always consistant and as the filter transmission coefficient is

Night	Frequency Range (Hz)		n
23 August 1973	5×10^{-3}	to 5×10^{-2}	-2.25
	5×10^{-2}	to 10^{-2}	-1.0
	10^{-2}	to 1.6×10^{-2}	-0.3
17 September 1973	5×10^{-3}	to 4×10^{-2}	-2.3
	4×10^{-3}	to 9×10^{-3}	-1.25
	1.1×10^{-3}	to 1.6×10^{-3}	0
28 September 1973	5×10^{-3}	to 2.5×10^{-2}	-1.7
	2.5×10^{-2}	to 4×10^{-2}	-3.0
	4×10^{-3}	to 10^{-2}	-1.5
	10^{-2}	to 1.6×10^{-2}	-0.9
1 October 1973	5×10^{-3}	to 4.5×10^{-2}	-2.1
	4.5×10^{-3}	to 1.5×10^{-2}	-1.3
29 November 1973	5×10^{-4}	to 4×10^{-3}	-2.2
	4×10^{-3}	to 7×10^{-3}	-0.3
	7×10^{-3}	to 9×10^{-3}	-3.5
	9×10^{-3}	to 1.6×10^{-2}	-1.6

Table 4.1 Fall-off Spectral Power of 557.7 nm [OI] Intensity Variations with frequency.

n is given by relation $P(f) \propto f^{-n}$ where P(f) is the spectral power at frequency f.

highly dependent on the exact position of the field stop, this could give rise to such an effect on the spectral power distribution.

CHAPTER 5

POSSIBLE CAUSES OF OBSERVED 557.7nm (OI) INTENSITY VARIATIONS

5.1 Introduction

Chamberlain (Aurora and Airglow, p. 550) attributes the patchiness in the green-line emission in the 100 km region to turbulent motion where a greatly increased rate of mixing may sufficiently modify the degree of dissociation at a given level to affect the rate of emission. Hines (1960) proposed that many of the winds and apparent motions in the ionosphere are manifestations of internal gravity waves. In the earth's atmosphere, the two phenomena are now thought to be intimately connected in the sense that turbulence may initiate internal gravity waves (Jordan, 1972) which in turn produce turbulence at other localities (Hodges, 1969; Hines, 1970).

5.2 Considerations Concerning Spectral Power

This section will be involved in establishing the effect which turbulence and internal gravity waves would be expected to have on the power spectra of 557.7nm (OI) intensity measurements.

5.2.1 TURBULENT SPECTRAL CHARACTERISTICS

In the Kolmogorov spectrum, the scale size of the irregularities or eddies in the region where turbulence exists is restricted to the range defined as the inertial subrange $k_0 < k < k_s$ where k_0 is the wave number of the largest eddy size corresponding to the scale size at which energy is introduced in the system and k_s refers to the scale size at which energy dissipation through molecular viscosity and heat conduction is

important. In the inertial subrange, the turbulent energy spectrum $\varepsilon(K)$ is given by

$$\varepsilon(K) = \alpha\epsilon^{3/2}k^{-5/3} \tag{5.1}$$

where α is a universal constant and is approximately 1.44, and ϵ is the dissipation rate of turbulent kinetic energy.

Zimmerman (1967) has shown from a study of chemical releases around the 100 km region that a Reynolds Number $Re_k \geq 3.4 \times 10^4$ is required for the spectral dependence to follow the -5/3 relation as specified by equation (5.1). However, Zimmerman (1973) finds this to contradict the results of Roper and Elford (1963) and Roper (1966) where their meteor studies exhibit this -5/3 power dependence for maximum horizontal scale sizes of not greater than 3 km. This corresponded to velocities of the order of 5 ms^{-1} and hence one would expect the time scale of the largest eddies to be about 60 seconds.

The variation of the turbulent energy spectrum with frequency is given by (Tennekes and Lumley, p. 277)

$$\psi(\omega) = \alpha^{3/2}\epsilon\omega^{-2} \ . \tag{5.2}$$

5.2.2 SPECTRAL CHARACTERISTICS OF ACCOUSTIC-GRAVITY WAVES

Accoustic-gravity waves are characterized by the existence of two frequency branches. In an isothermal atmosphere, the high frequency branch $(\omega > \omega_a)$ where ω_a, the accoustic cut-off frequency, is given by

$$\omega_a = c/2H \tag{5.3}$$

where c is the speed of sound and H the scale height.

The low frequency branch in the frequency range $\omega < \omega_b$ is designated the gravity branch where the high frequency cut-off ω_b known as the buoyancy frequency, is given by

$$\omega_b = \left(\frac{g(\gamma-1)}{\gamma H}\right)^{\frac{1}{2}} \qquad (5.4)$$

where γ is the ratio of specific heats and g is the gravitational field strength. If the atmosphere is non-isothermal, the buoyancy frequency ω_b becomes

$$\omega_b = \left(\frac{g\left(\gamma-1+\gamma\frac{dH}{dz}\right)}{\gamma H}\right)^{\frac{1}{2}} \qquad (5.5)$$

where $\frac{dH}{dz}$ is the height derivative of the scale height. In the frequency range $\omega_b < \omega < \omega_a$, there are no free waves.

In the accoustic-gravity wave spectrum, there may be preferred modes and this will be discussed in Section 5.4 in relation to filtering by wind profiles and ray tracing from sources.

5.2.3 DISCUSSION OF THE OBSERVED 557.7nm (OI) POWER SPECTRA

The value of ω_b at 96 km calculated from equation (5.5) where $\gamma = 1.4$, $g = 9.504$ m-sec^{-1}, $H = 6107$ metres and $\frac{dH}{dz} = 0.0835$ (Cospar, 1965) is 3.82×10^{-3} Hz which corresponds to a period of 262 seconds.

In section 4.4 with particular reference to Table 4.1, the spectral power variation with frequency on each night demonstrates a change in characteristics at a frequency near 4×10^{-3} Hz. On 29 November, 1973 a feature in the nightly power spectrum which did not appear on any other night consists of a shoulder at frequencies above this frequency with a further feature which could be interpreted as a cut-off frequency at 9×10^{-3} Hz.

An alternative way of viewing the power spectra of 557.7nm (OI) variations occuring on a particular night is by means of spectrograms as

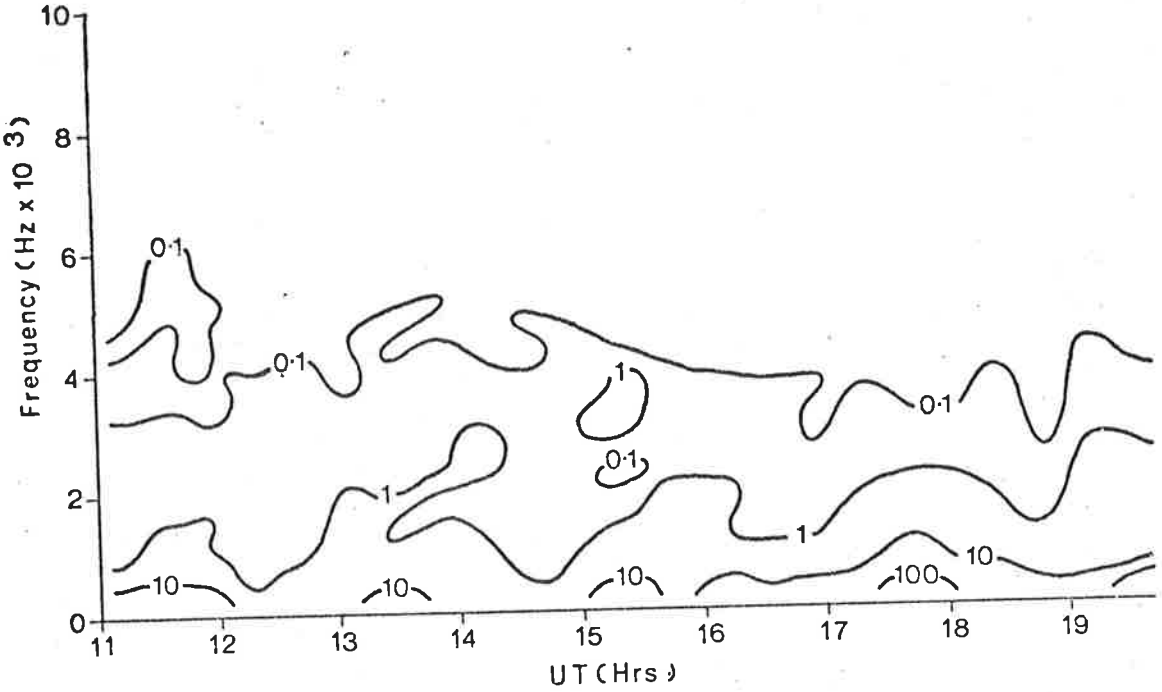

Figure 5.1 Spectrogram comprising contours of relative power (intensity^2/Hz) of [OI] λ 557.7nm intensity fluctuations observed on the 17 September 1973.

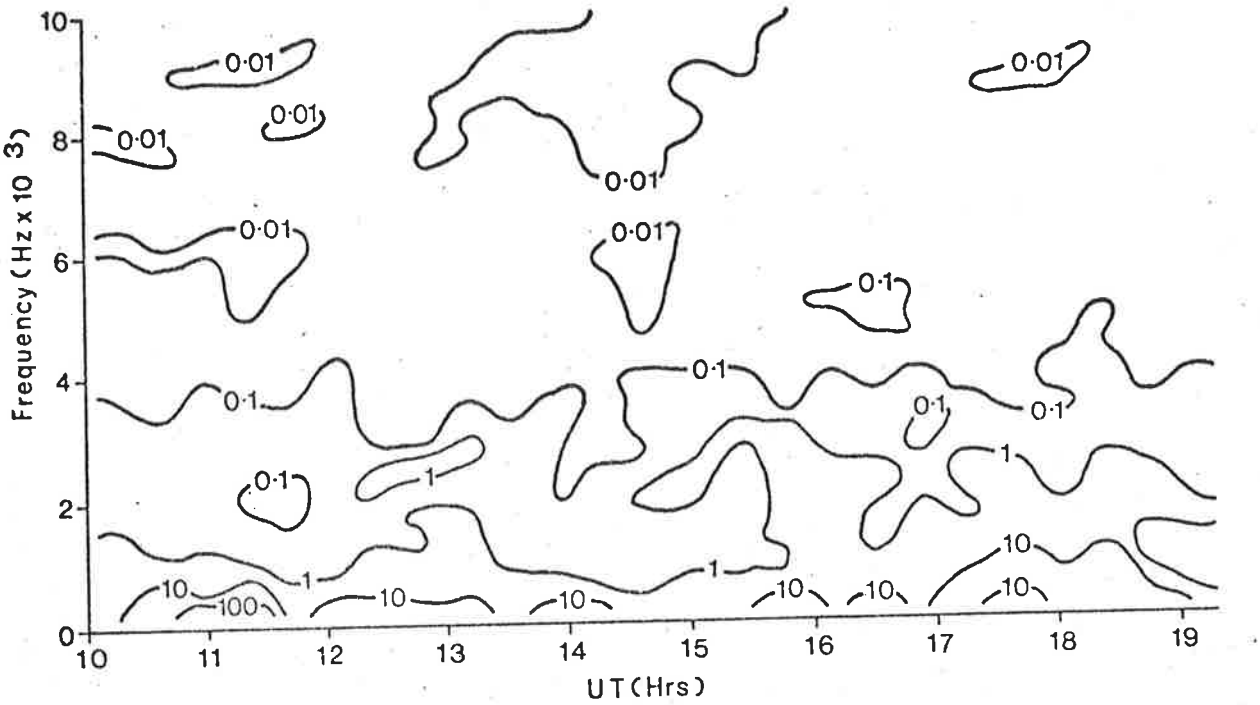

Figure 5.2 Spectrogram comprising contours of relative power (intensity^2/Hz) of [OI] λ 557.7nm intensity fluctuations observed on the 28 September 1973.

in Figures 5.1, 5.2 and 5.3 in which contours of constant spectral power are mapped against time on the horizontal axis and frequency on the vertical axis. The power spectra were found using the technique outlined in Section 4.1.2, successive data lengths being chosen such that the end of one data length coincides with the middle of the next data length. Treating each data length with a Hanning Window ensures that every data point contributes an equal weight. The length or period of each data block was about 23 minutes.

Spectrograms of 17 September, 1973 and 28 September, 1973 presented in Figures 5.1 and 5.2 reveal that at least in a relative sense, very little spectral power is present at frequencies greater than 4×10^{-3} Hz . Also the spectral power contour of value 0.1 does not deviate appreciably from this frequency value of 4×10^{-3} Hz. Higher spectral power values are less constrained to any one frequency level. This logically could be interpreted as the existence of a cut-off frequency at 4×10^{-3} Hz.

In the spectrogram of 29 November, 1973 appearing in Figure 5.3, significant spectral power during the second half was located at frequencies greater than 4×10^{-3} Hz and at one stage extended to at least 10^{-2} Hz. It is possible for gravity waves to be observed at frequencies less than the buoyancy frequency since the frequency viewed from the ground will be different to that of the wave frequency in the frame of reference of the wave in the presence of a background wind. If the horizontal wind velocity is v_0, the frequency shift of a wave is given by (YL, 32b)*

$$\omega' = \omega - \underset{\sim}{k} \cdot \underset{\sim}{v}_0 \qquad (5.6)$$

---

* (YL, 32b) refers to equation 32b in a review paper by Yeh and Liu (1974).

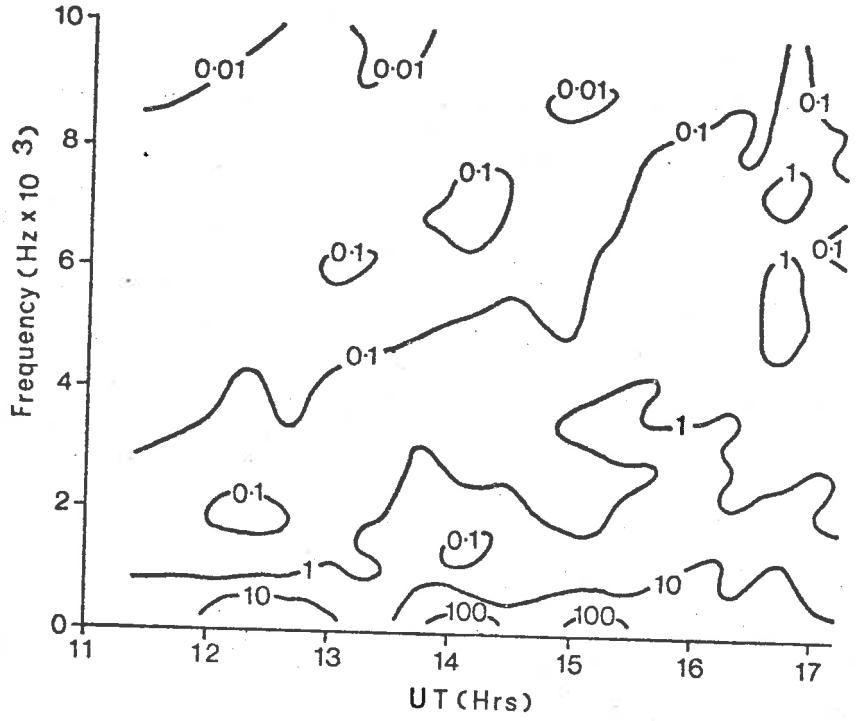

Figure 5.3 Spectrogram comprising contours of relative power (intensity^2/Hz) of [OI] λ 557.7nm intensity fluctuations observed on the night of 29 November 1973.

where ω is the apparent frequency of a wave in a stationary frame of reference, ω' is the wave frequency in the frame of reference of the wind and k is the wave number. A wave propagating in the direction of the wind will therefore have an increased frequency when observed from the ground. However, the required frequency shift would require circumstances such as a wave with a horizontal wavelength less than 20 km propagating with a wind with a velocity greater than 100 ms^{-1}.

Another possibility which could account for the spectral power characteristics of this night is that the 557.7 nm (OI) irregularities show wave breaking. This may arise when exponential wave growth with height is limited by dissipation. There are two features which could be significant in deducing whether wave breaking is a plausible alternative. Firstly, with reference to Figure 4.6a where intensity profiles of some of the relevent irregularities appear, the degree of correlation between the records of the four fields of view is not, at least in a qualitative sense, as great as that between the other irregularities appearing in Chapter 4 and this may have been a result of wave breaking. Also, as will be discussed later in this chapter, severe dissipation in a wave may arise when the wave amplitude reaches a certain level, and this might be the case here since the amplitude of the relevant irregularities is relatively large. However, the question exists as to whether wave breaking in gravity waves could result in spectral power of the magnitude observed at frequencies less than the buoyancy frequency.

Throughout this section the observed 557.7nm (OI) irregularities have been associated only with internal gravity waves. However, this does not exclude contributions from other causes, e.g. in Section 4.4 it was found that significant spectral power at levels above the estimated noise level existed at frequencies greater than 4×10^{-3} Hz on most

occasions.

5.2.4 ENERGY DISSIPATION OF GRAVITY WAVES

The wave equation of acoustic-gravity waves for plane waves is of the form (Hines, 1960)

$$\frac{\rho'}{\rho_0}, \frac{p'}{p_0}, u_x', u_y', u_z' \propto \exp \frac{z}{2H} \exp i(\omega t - k_x x - k_y y - k_z z) \qquad (5.7)$$

where ρ', p', u_x', u_y', u_z' are gravity wave induced variations of density, pressure and wind components superimposed on background values. The exponential growth term z/2H will be negated to varying extents by a dissipation term which can be represented by k_z'', the imaginary part of k_z computed approximately (Yeh and Liu, 1974) by using

$$k_z'' = \frac{W}{2\Gamma_z} \qquad (5.8)$$

where W is the time-averaged dissipation per unit volume and Γ_z is the vertical component of the energy flux represented by (Yeh and Liu, 1974)

$$\Gamma_z = \left|\frac{\rho'}{\rho_0}\right|^2 \frac{\rho_0 c^2 \left(\omega^2 - \omega_b^2\right) \omega k_z}{2\left(\left(\omega - \frac{g(\gamma-1)}{2H}\right)^2 + g k_z (\gamma-1)\right)^2} . \qquad (5.9)$$

Wave attenuation in a night time atmosphere at heights less than 96 km is mainly due to thermal conduction and viscous dissipation and may be represented by the complex imaginary wave numbers $(k_z'')_{tc}$ and $(k_z'')_{vd}$ respectively, their expressions being given by equations (46) and (47) of Yeh and Liu. These are related to the imaginary wave number k_z'' by

$$k_z'' = (k_z'')_{tc} + (k_z'')_{vd} . \qquad (5.10)$$

The thermal conduction κ is related to the kinematic viscosity ν by

$$\frac{\kappa}{\rho} = \frac{\gamma C_v \nu}{Pr} \qquad (5.11)$$

where Pr is the Prandtl number and is 0.74.

Hodges (1969), Hines (1970) have proposed a mechanism for a zero growth wave where the attenuation rate k_z'' is

$$k_z'' = -\frac{1}{2H} . \tag{5.12}$$

According to Hodges, a wave propagates upwards with near exponential growth until an instability, which may be indicated by the Richardson Number falling below a critical value, develops leading to turbulence and an enhanced attenuation rate and therefore increased extraction of energy from the wave. If the attenuation rate exceeds that of equation (5.12) the amplitude of the wave will decrease to a level where the instabilities will cease thus reducing the attenuation rate of the wave. The result is an equilibrium situation where the attenuation rate is represented by equation (5.12). The localization of these instabilities can be demonstrated from equation (C-8) in Appendix C where the local Richardson Number is shown to depend on the phase of the wave. In regions of turbulence, one would expect enhanced values of kinematic viscosity and thermal conduction. An adaptation of the calculation for the value of the kinematic viscosity associated with a zero growth wave as carried out by Hodges (1969) is presented in Appendix D, along with the energy dissipation rate of a wave with an amplitude of $\frac{\rho'}{\rho_0} = 0.01$ and an attenuation rate of $k_z'' = \frac{1}{2H}$.

The spectra of internal gravity waves being altered by self induced turbulence at altitudes around 96 km may very well be a real effect but the maximum amplitudes of waves will be governed by the presence of other gravity waves, tides etc. In Appendix C it is suggested that the maximum relative density amplitude of a zero growth wave is such that

$$\left|\frac{\rho'}{\rho_0}\right| \lesssim 0.2. \tag{5.13}$$

This is to say that a wave where $\left|\frac{\rho'}{\rho_0}\right|$ is nearing 0.2 would be expected to be in a condition approximating zero growth.

Referring back to equation (1.6) and the 4-field photometer intensity variations (Figures 4.2a-4.6a) one finds short period ($\leq$ 15 min.) gravity waves of amplitudes up to $\frac{I}{I_0} \sim 0.05$ corresponding to amplitudes in density of the order of $\frac{\rho'}{\rho_0} \sim 0.02$. By themselves it is still unlikely that they are capable of producing sufficient turbulence but when superimposed on a background of other waves, tides etc., waves of this amplitude could be in a situation of approximately zero amplitude growth. From Figures D-1 and D-2, the energy dissipation for a wave of this amplitude would be $\sim 10^{-7}$ watts-m^{-3} and the kinematic viscosity necessary for zero amplitude growth would be 10^4 m -sec^{-1} which are of the order of the dissipation rate of turbulent kinetic energy and the associated kinematic viscosity estimated by Zimmerman (1973) from the meteor trail data of Roper and Elford (1963). Therefore gravity waves would be a significant source of energy at this altitude.

5.3 Gravity Wave Propagation

In this section some characteristics of gravity waves which may be useful in establishing sources of such waves will be outlined. Brief descriptions of ray tracing and also the filtering of gravity waves in an atmosphere will also be included.

5.3.1 FILTERING BY WIND AND TEMPERATURE PROFILES

Reflection of gravity waves in an atmosphere will occur at boundaries where discontinuities in temperature, wind velocity and density exist.

A technique for the calculation of transmission coefficients of gravity waves through a vertically stratified atmosphere is outlined in Appendix E. The atmospheric layer considered is that between 20 km and 95 km and this has been divided into a series of thin layers with the horizontal wind velocity and temperature discontinuous at the layer boundary and constant within the layer and the density unchanged at the boundary but varying exponentially within the layer. Attenuation due to viscosity and thermal conduction within the layer has been included with the kinematic viscosity being set to 100 $m^2 sec^{-1}$ in each layer.

A plot of the particular wind and temperature profile used appears in Figure E-2 and Figures E.3a, b, c and d provide a summary of transmission coefficients for waves of different periods and horizontal phase velocities.

There are two main effects which reduce wave transmission evident in these Figures. Firstly, attenuation occurs in regions in which the wave becomes evanescent through the wave frequency becoming greater than the buoyancy frequency although there will be some leakage of wave energy through such regions. This results in a sharp decrease in the transmission for waves with periods less than 6 minutes. Also waves propagating in a direction opposite to that of the wind with a horizontal phase velocity less than or of the order of the maximum horizontal wind component in the direction of the horizontal wave number may also have their transmission coefficients reduced through having an imaginary vertical wave number in some regions.

Secondly, waves are not transmitted through critical layers i.e. regions where the horizontal wind component in the direction of the horizontal wave vector exceeds the horizontal phase velocity. It is found that upon inclusion of the attenuation factor, the transmission coefficient is significantly reduced whenever the horizontal wind component exceeds

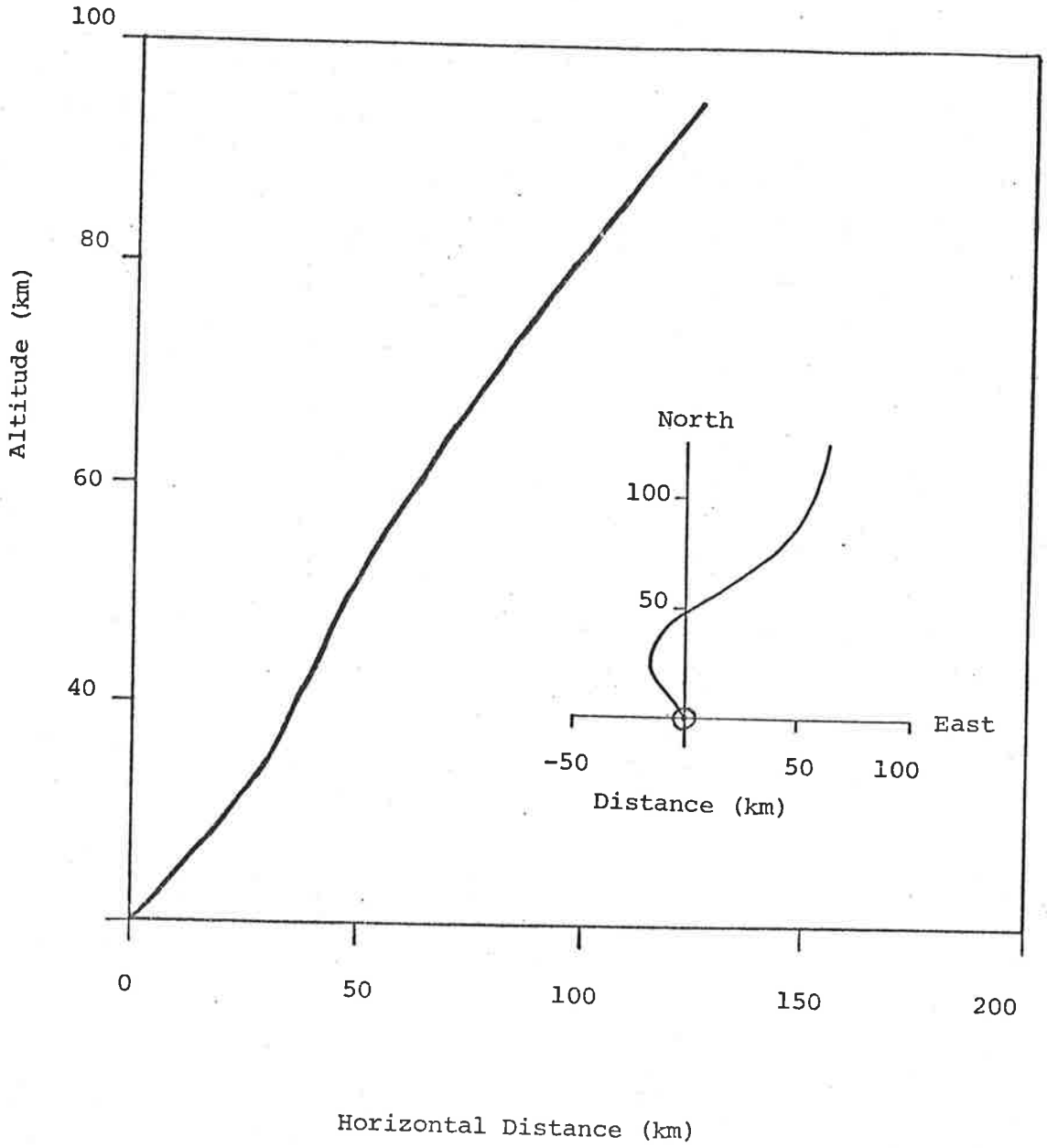

Figure 5.4 Plot of the ray path of an upwardly propagating gravity wave with period = 10 minutes, horizontal phase velocity = 50 $m\text{-}s^{-1}$, $\psi = 0^{o}$. The direction of the horizontal phase velocity is due north.

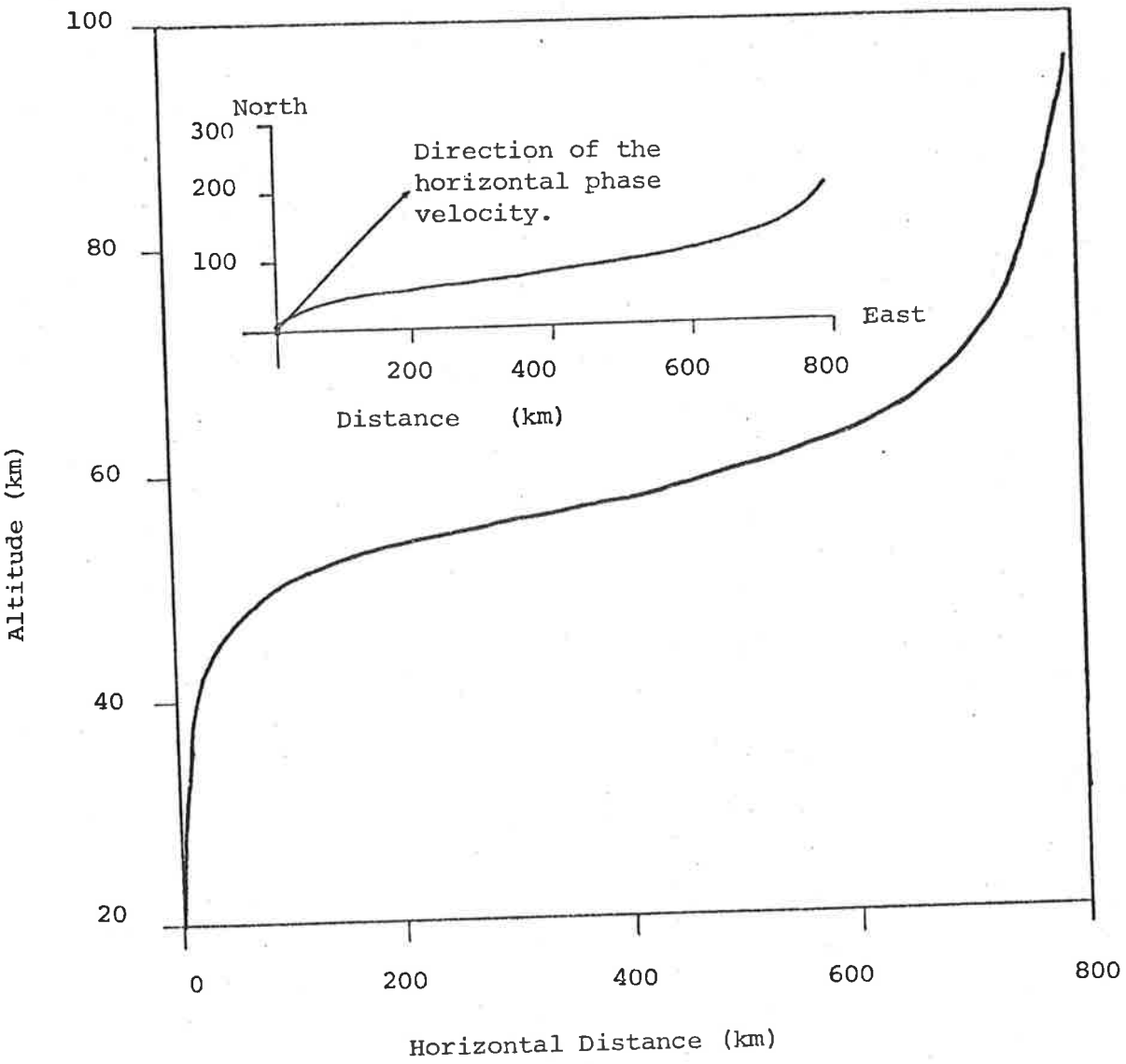

Figure 5.5 Plot of the ray path of an upwardly propagating gravity wave with period = 10 minutes, horizontal phase velocity of 50 $m\text{-}s^{-1}$ and $\psi = 45^{0}$.

0.6 of the horizontal phase velocity in the wind direction.

5.3.2 RAY TRACING

A simple ray tracing routine can be formulated using the multilayer approach outlined in the previous section. If the position of the wave is known at the base of a layer, computation of its group velocity allows one to find its position at the top of the layer. Calculation of frequency ω, vertical wave number k_z in the next layer allows one to repeat the process. This technique has been applied by Cowling et al (1971) for a model atmosphere with vertically stratified horizontal winds. This method has been adapted for ray tracing in the 20 km to 95 km region using the wind and temperature profiles of Figure E.2. The layer thickness was chosen such that in adjacent layers

$$\left(\frac{\omega_1}{\omega_2} - 1\right)^2 < 0.2 \qquad (5.14a)$$

and

$$\left(\frac{k_{z1}}{k_{z2}} - 1\right)^2 < 0.2 \qquad (5.14b)$$

where ω_1, ω_2 and k_{z1}, k_{z2} are the frequencies and vertical wave numbers in adjacent layers. Conditions (5.14a) and (5.14b) were over-ridden when the layer width was less than 10^{-2} km and the vertical wave number in the adjacent upper layer was imaginary. From equations (E.8) and (E.9) it is clear that at such a boundary where k_z is real on one side and imaginary on the other, $|R| = 1$ and therefore reflection occurs.

Examples of ray tracing are presented in Figures 5.4, 5.5, 5.6 and 5.7 for a 10 minute period wave and a horizontal phase velocity of 50 m-s^{-1} with $\psi = 0°$, 45°, 90° and 315° respectively (ψ is the direction of the horizontal wave number measured clockwise from the north). Two graphs are

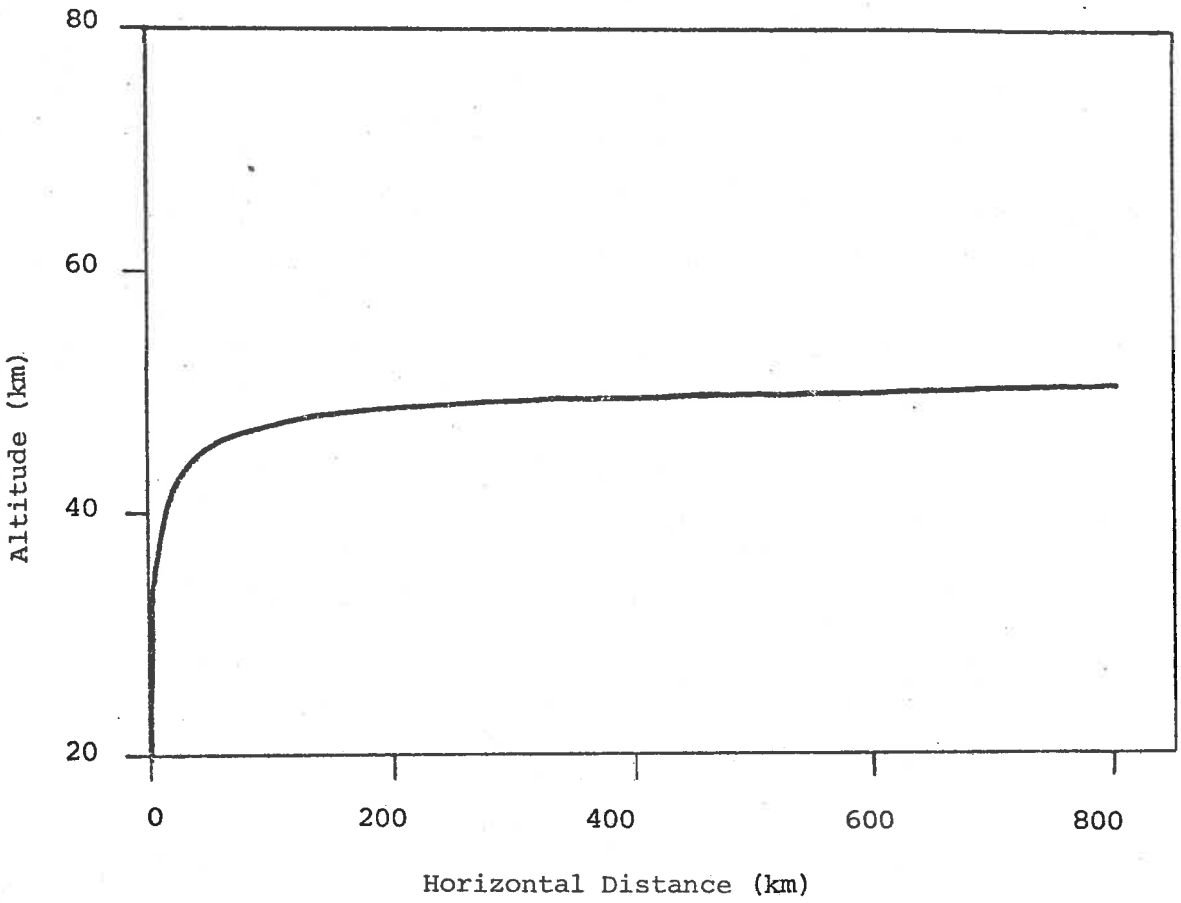

Figure 5.6 Plot of the wave path of an upwardly propagating gravity wave with period = 10 minutes, horizontal phase velocity = 50 $m\text{-}s^{-1}$, $\psi = 90^0$. The projection of the ray path on to a horizontal plane is not included since the wave propagates at all points in an eastward direction.

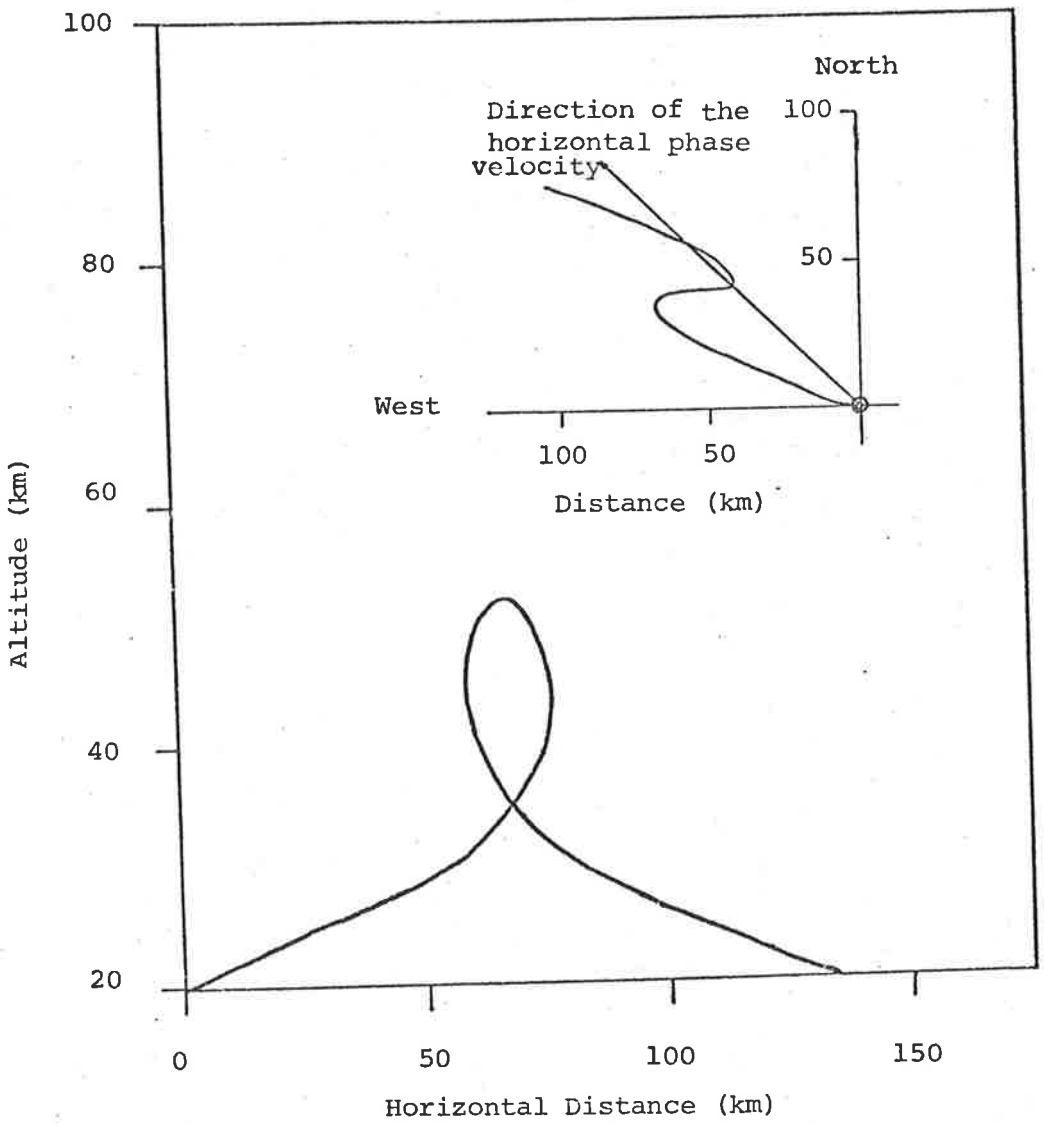

Figure 5.7 Plot of the ray path of an upwardly propogating wave with period = 10 minutes, horizontal phase velocity = 50 $m.s^{-1}$ and $\psi = 315^{o}$.

required to present a 3 dimensional picture, and in the Figures the height of the wave is plotted against the horizontal displacement in the first graph and the second shows the wave path superimposed on a horizontal plane.

In Figure 5.4 the horizontal phase velocity is at right angles to the eastward wind. This wave is not greatly affected by the wind although it is shifted from the N-S plane. The travel time for 20 km to 95 km is 55 minutes and the transmission coefficient as estimated in Appendix E is 0.88.

In Figure 5.6 where the horizontal phase velocity is in the direction of the wind, the frequency is doppler shifted to zero near 50 km and this level is termed the critical layer for the wave. With the attenuation factor used in Appendix E, the wave will be completely attenuated.

Figure 5.5 shows a wave which has neared a critical layer and is in fact carried along by the wind. The travel time is 3.9 hours and the transmission coefficient estimated in Appendix E is 0.007.

Fiture 5.7 shows a wave propagating partly into the wind and which is reflected. Referring to Appendix E, one finds that the transmission coefficient is 0.34 i.e. there is a significant leakage of energy through to 96 km.

To trace waves in the fashion of this section one needs to have an accurate knowledge of the wind profile and this may not always be practical. This section also demonstrates that the direction of the horizontal phase velocity and the trace velocity does not always provide an accurate indication of the direction of the source of the wave.

5.3.3 RESONANT FREQUENCY APPROXIMATION

To be used with caution since the direction of the trace velocity

is not always indicative of the position of the wave source, a simple technique for deducing the approximate position of the source using the observed frequency and the horizontal trace velocity direction exists since the observed frequency may be related to the source by the relation (Yeh and Liu, 1974)

$$\omega = \frac{\omega_b z}{r} \tag{5.15}$$

where z is the observation height and r is the distance from the source to the point of observation.

5.3.4 WAVE GENERATION

Small short period fluctuations in pressure have been frequently reported by meteorologists. Jordan (1972), using an array of micro-barographs and anemometers, identified the sources of low velocity gravity waves with periods in the range 3 to 24 minutes to be wind shears associated with jet streams, mountain slopes and cold fronts. Thunder-storms also acted as a pulse source for gravity waves.

Hines (1967) from observations on noctilucent clouds found that cold fronts may be a source of wave-like patterns which are frequently characteristic of these clouds.

Yeh and Liu (1974) have reviewed ionospheric observations of gravity waves and possible sources include nuclear explosions, auroral disturbances which may give rise to large scale travelling ionospheric disturbances and siesmic waves. Medium scale travelling disturbances are also frequently observed without any satisfactory explanation being offered for their existence.

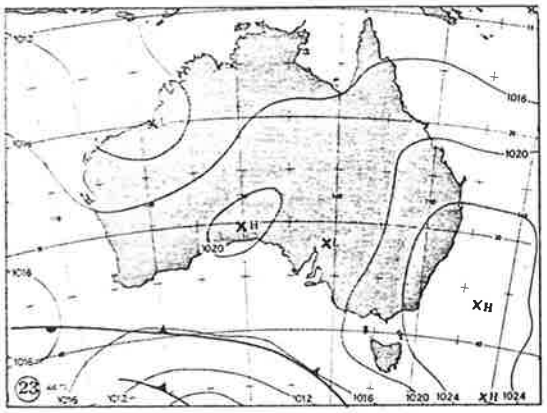

23.8.73

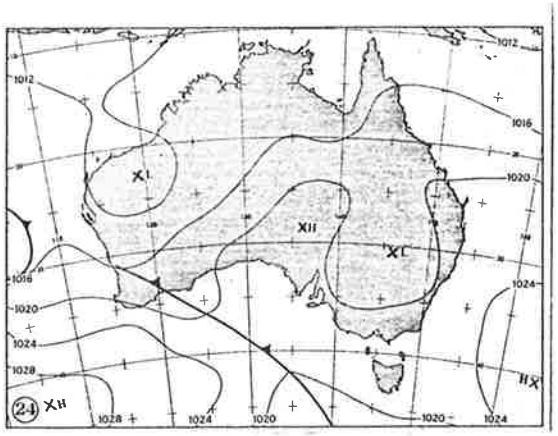

24.8.73

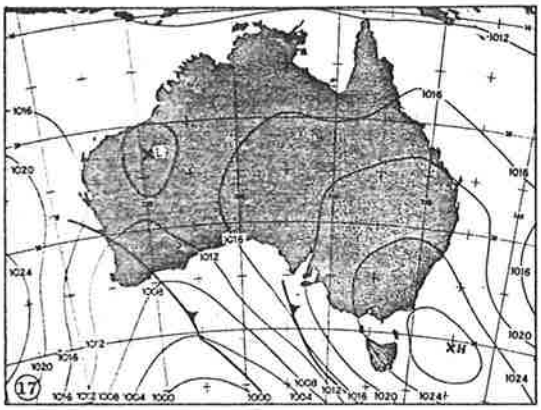

17.9.73

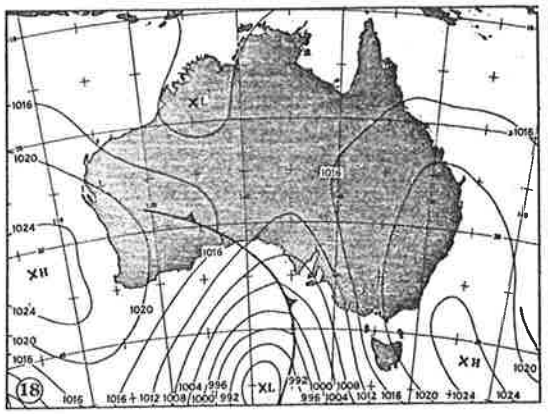

18.9.73

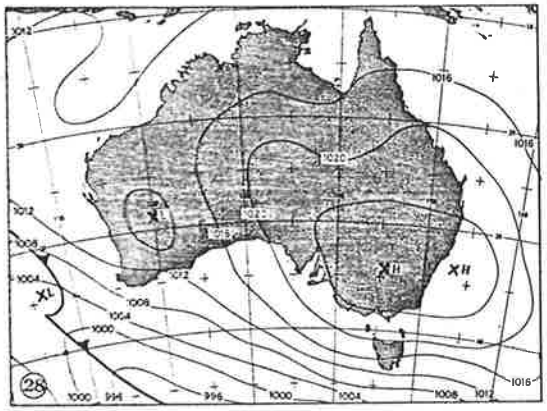

28.9.73

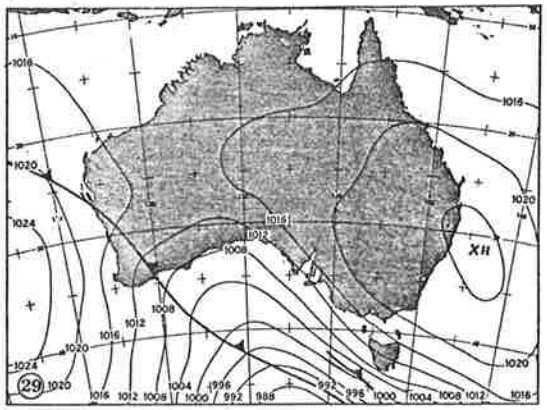

29.9.73

Figure 5.8a Daily weather maps compiled at 0900 EST (2300 G.M.T.)

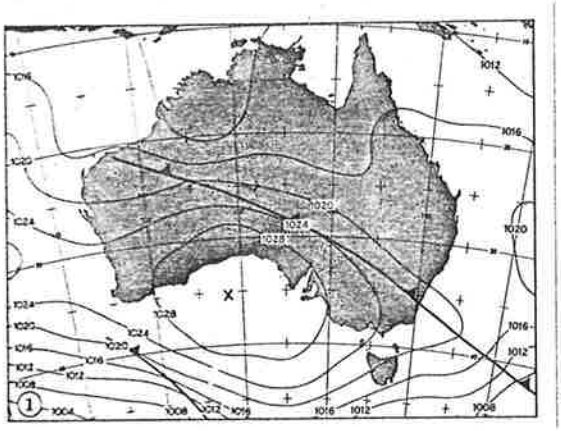

1.10.73

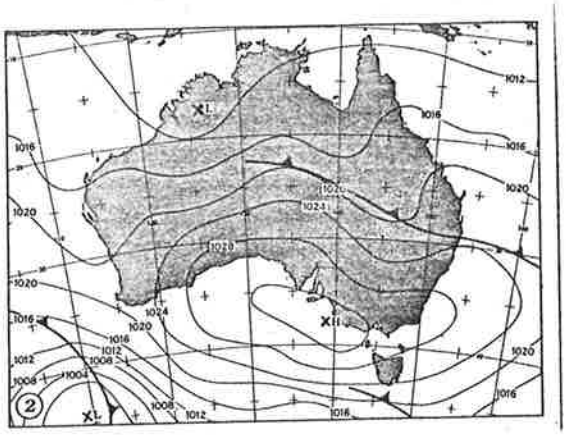

2.10.73

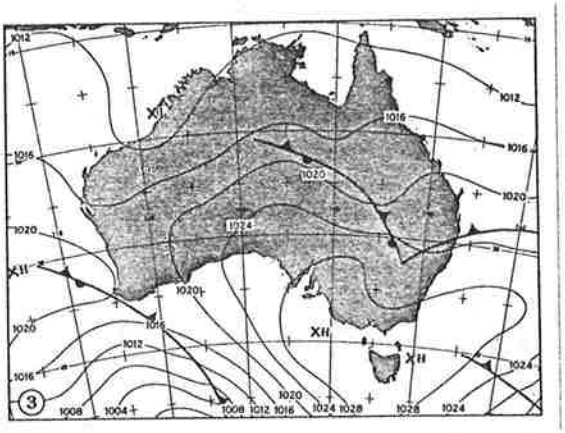

3.10.73

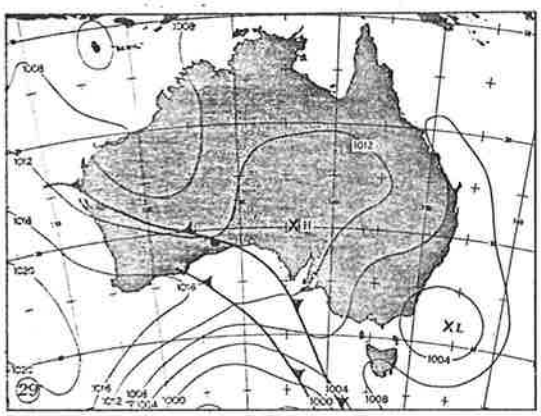

29.11.73

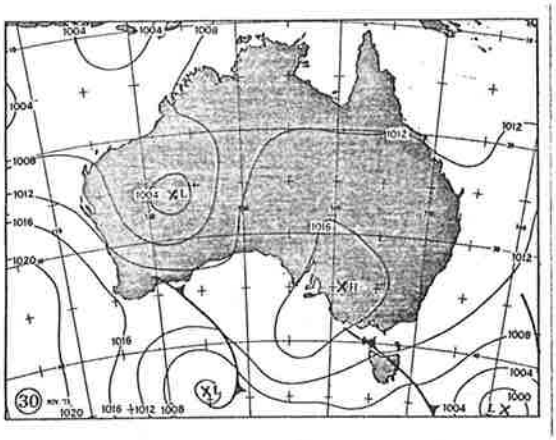

30.11.73

Figure 5.8b Daily weather maps compiled at 0900 EST (2300 G.M.T.)

5.4 A possible Source for Waves observed in the 557.7nm (OI) Airglow

Two reasons may now be offered for the anisotropic nature of the trace velocities observed e.g. with reference to Figure 4.13. A substantially isotropic distribution could be filtered by a significant background wind at some level to give rise to a more uneven distribution at a higher altitude in the manner described in Section 5.3.1. Or alternatively, the distribution may be due to some isolated source and the techniques of Sections 5.3.2 and 5.3.3 could be used to find its position. More likely the waves observed arise at some source, but the spectrum observed may be significantly affected by favourable wind, temperature and perhaps density profiles.

A likely source of gravity waves is cold fronts, and it is the object of Table 5.1 to illustrate that some degree of correlation exists between the position of ground level cold fronts and the observed spectral characteristics. The presence of long period gravity waves has already been noted in Sections 4.2.3 and 4.2.5 and their period and their relative spectral power (in paranthesis) appear in column 3 of this table. They were obtained by grouping the longest possible continuous lengths of λ 557.7nm (OI) intensity data together, the times for which appear in columns 1 and 2, and finding the spectral power by treating the data with a Hanning Window and using FFT. The expected period of gravity waves due to cold fronts has been calculated using the technique of Section 5.3.3. The distance r was set equal to the length of a perpendicular drawn from the cold front to Mt. Torrens for local midnight. The relevant weather maps featuring the cold fronts appear in Figure 5.8. As the weather maps were compiled at 08.30 local time, it was necessary to estimate the position of the cold front at local midnight. This is not easy to accomplish as cold fronts tend to change shape, move in a non-linear fashion

Date	Time (UT)	Measured spectral peak period (in minutes) and relative power	Resonant Period (in minutes)	Direction to cold front
23. 8.73	1322 → 2022	32(.08), 28(.28), 23(.11), 21(.055) 10(.035), 7(.025)	48	SW
17. 9.73	1048 → 1502	18(.12), 14(.07), 10(.05), 7.5(.035), 6(.03)	43	SSW
	1502 → 1909	49(1.2), 28(.12), 18(.14), 9(.06)		
28. 9.73	0950 → 1922	82(.33), 52(.075)	78	SSW
1.10.73	1003 → 1702	84(.029, 47(.16), 32(.06), 18(.04), 14(.04)	47	NNE
2.10.73	1024 → 1415	75(.38), 32(.02), 17(.035), 10(.025)	54 104	NE SW
29.11.73	1110 → 1728	54(.79), 35(.18), 24(.14), 19(.20)	46	SW

Table 5.1 Summary of the relation between the observed characteristics of gravity waves and ground level cold front positions.

and it is typical of many fronts in the Great Australian Bight to slide away to the south. The fifth column provides a guide to position of the cold front from Adelaide. The directions of the drift velocities may be found in Chapter 4 e.g. Figure 4.13. However, it must be pointed out that those drift velocities were not the drift velocities of long period waves but rather for shorter period waves. This may not be very serious since the same source could produce waves at the observation point markedly different than those which would be predicted by Section 5.3.3. Also it could be postulated that long period gravity waves in a state of self dissipation as described in Section 5.2.4 could produce waves of a shorter period but which would propagate in a similar direction to their parent.

Although not conclusive there is sufficient correlation between the position of cold fronts and the characteristics of the observed gravity waves to be significant e.g. between the expected and observed periods on 28 September, 1973, 1 October, 1973 and also between the mean drift velocity directions plotted in Figure 4.13 and the cold fronts position e.g. a cold front on 1 October, 1973 situated NNE of Adelaide and the southward propogating drifts.

APPENDIX A

LAG TIME UNCERTAINTY

The lag time between signals observed in a speed receiver network has been defined in Section 1.3.2, and in Section 3.2.3 it is required that the error in lag time be estimated when a signal of a given amplitude and frequency is observed. The signal considered will be that of a sinuosoidal signal superimposed on a large D.C. level such that

$$I(t) = a_1 + a_2 \sin(a_3 t + a_4) \qquad \text{A.1}$$

where I(t) represents the the overall signal, a_1 the D.C. level, a_2 the amplitude of the time varying signal, a_3 its frequency and a_4 some phase angle.

Experimentally from each detector, n data points each with N_i signal counts will be collected and a function such as equation A.1 could be fitted using a grid search least squares routine. The goodness of the fit of the function to the data is represented by

$$\chi^2 = \sum_n \frac{1}{\sigma_i^2} |N_i - I(t_i)|^2 \qquad \text{A.2}$$

where N_i represents the number of signal counts measured at some time t_i and σ_i is the standard deviation of the population from which N_i is assembled. The value of the standard deviation for each parameter is given by the relation (Bevington, 1969, p. 245)

$$\sigma a_j^2 = \frac{2}{\partial^2(\chi)^2/\partial a_j^2} . \qquad \text{A.3}$$

On differentiating χ^2,

$$\frac{\partial^2(\chi)^2}{\partial a_4^2} = \sum \frac{2a_2}{\sigma_i^2} \left[(N_i - a_1)\sin(a_3 t_i + a_4) + a_2 \cos^2(a_3 t_i + a_4) - a_2 \sin^2(a_3 t_i + a_4) \right] . \qquad \text{A.4}$$

Since $I(t_i)$ is the fitted function to the data points N_i, then $N_i \simeq a_1 + a_2 \sin(a\, t_i + a_4)$ and the standard deviation of a_4 represented by σa_4 will be approximately

$$\sigma a_4^{\,2} \approx \frac{1}{a_2^{\,2} \sum_n \frac{1}{\sigma_i^{\,2}} \cos^2(a_3 t_i + a_4)} \,. \qquad \text{A.5}$$

Since we are concerned with a small time varying signal superimposed on the D.C. background i.e. $a_1 >> a_2$, then $\sigma_i \simeq \bar{\sigma}$ where $\bar{\sigma}$ represents the mean standard deviation. The term $\sum_n \cos^2(a_3 t_i + a_4) \simeq \frac{n}{2}$ as the average value of $\cos^2(a_3 t_i + a_4) = \frac{1}{2}$. Equation A.4 can be written in the form

$$\sigma a_4^{\,2} = \frac{2\sigma^2}{a_2^{\,2} n} \,. \qquad \text{A.6}$$

The mean number of signal counts $\bar{N}$, the variance $\bar{\sigma}^2$ and the parameter a_1 are all approximately equal. A parameter α representing the relative amplitude of the time varying signal will be defined as

$$\alpha = a_2/a_1 \qquad \text{A.7}$$

and equation A.5 can be rewritten as

$$\sigma a_4 = \frac{1}{\alpha} \sqrt{\frac{2}{\bar{N} n}} \,. \qquad \text{A.8}$$

Equation A.1 may be written in the alternative form

$$I(i\Delta t) = a_1 + a_2 \sin \frac{2\pi}{T} (i-j)\Delta t \qquad \text{A.9}$$

where the intensity is sampled at intervals Δt, T is the period of the intensity variation and $j\Delta t$ will be related to the phase angle a_4 by

$$j\Delta t = - \frac{T a_4}{2\pi} \,. \qquad \text{A.10}$$

The standard deviation of $j\Delta t$, $\sigma j\Delta t$ will represent the error in

time in fitting the function to the data points and will be given by

$$\sigma j\Delta t^2 = \sigma a_4{}^2 \left[\frac{\partial(j\Delta T)}{\partial a_4}\right]^2 + \sigma T^2 \left[\frac{\partial(j\Delta t)}{\partial T}\right]^2 . \qquad \text{A.11}$$

Finding σa_3 in a similar fashion to σa_4 and since $a_3 = \frac{2\pi}{T}$, the standard deviation of the period σT is given by the relation

$$\sigma T^2 = \frac{3T^4}{2\pi^2 \alpha^2 n^3 \Delta t^2 \bar{N}} \qquad \text{A.12}$$

and on combining A.10 and A.11,

$$\sigma j\Delta t^2 = \sigma a_4{}^2 \frac{T^2}{4\pi^2} \left| 1 + \frac{3a_4{}^2 T^2}{4\pi^2 n^2 \Delta t^2} \right| . \qquad \text{A.13}$$

The term $n\Delta t$ represents the time interval T_L over which data is collected. The magnitude of the phase angle $|a_4| \leq \pi$ and the average value of $|a_4| = \frac{\pi}{2}$. The second term in equation A.12 is therefore neglible if $T << T_L$ and the standard deviation of $j\Delta T$ is

$$\sigma j\Delta t \simeq \frac{T}{\pi\alpha(2\bar{N}n)^{\frac{1}{2}}} . \qquad \text{A.14}$$

This approximation is useful whenever $T \lesssim T_L$ since the contribution of the second term in equation A.13 to $\sigma j\Delta t$ is not large.

The value $\sigma j\Delta t$ may be related to the instrumental component in the standard deviation of time lag σtP where two curves with uncertainty in time $\sigma j\Delta t$ are compared either visually or by cross-correlation techniques by

$$\sigma tP = \sqrt{2}\, \sigma j\Delta t. \qquad \text{A.15}$$

APPENDIX B

RESPONSE OF A CIRCULAR FIELD OF VIEW

In photometry it must be remembered that a finite area of sky is being observed and the response of the photometer will decrease when the scale size of the irregularities is of the order of size of the field of view of the instrument. The nature of the irregularity considered here will be that of a wave type structure travelling horizontally in the x-direction extending infinitely in the y direction, i.e. a two dimensional plane wave. This restriction may not be too serious as much of the 557.7nm intensity variations at 96 km would be expected to be due to internally propagating gravity waves.

Assuming a wavelength λ, the intensity I(x) is thus

$$I(x) = \sin \frac{2\pi}{\lambda} (x-vt) \ . \qquad \text{B.1}$$

From Figure B.1 the response of a section dx of the field of view with diameter d is found to be

$$dI = 2\left[\left(\frac{d}{2}\right)^2 - x^2\right]^{\frac{1}{2}} \sin \frac{2\pi}{\lambda} (x-vt)dx. \qquad \text{B.2}$$

Integrating along the x-coordinate

$$I = 2 \int_{-\frac{d}{2}}^{\frac{d}{2}} \left[\left(\frac{d}{2}\right)^2 - x^2\right]^{\frac{1}{2}} \sin \frac{2\pi}{\lambda} (x-vt)dx. \qquad \text{B.3}$$

This integral is of the form

$$I = 2 \int_{-a}^{a} (a^2-x^2)^{\frac{1}{2}} \sin(bx \pm c)dx \qquad \text{B.4}$$

$$= 2 \int_{-a}^{a} (a^2-x^2)^{\frac{1}{2}} \sin bx \cos c \, dx \pm 2 \int_{-a}^{a} (a^2-x^2)^{\frac{1}{2}} \cos bx \sin c \, dx. \qquad \text{B.5}$$

The first part of the integral in B.5 is an odd function of x and hence

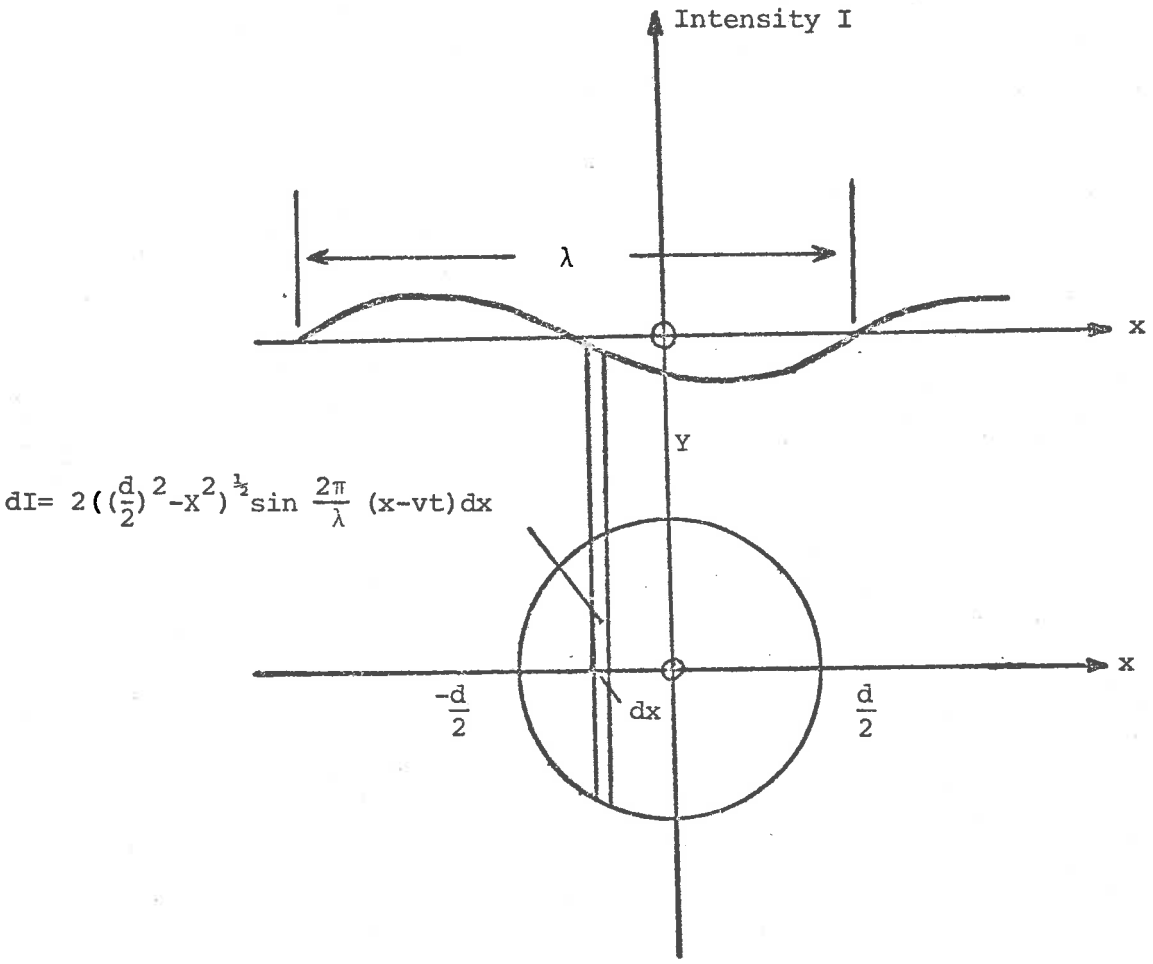

Figure B.1 Geometry of a sinusoidal intensity variation of wavelength λ propagating in the x-direction with velocity v across a field of view of diameter d.

vanishes and the second part integrates to

$$I = \frac{d\lambda}{2} \sin \frac{2\pi vt}{\lambda} J_1\left(\frac{\pi d}{\lambda}\right) \qquad \text{B.5}$$

where J is the first order Bessel function. In B.5 for $\frac{\pi d}{a} << 1$,

$I = \frac{\pi d^2}{4}$, i.e. the response would be that of a infinitely small field of view. If I_0 is defined as $I_0 = \frac{\pi d^2}{4}$ then

$$\frac{I}{I_0} = \frac{2J_1\left(\frac{\pi d}{\lambda}\right)}{\frac{\pi d}{\lambda}} . \qquad \text{B.6}$$

The criterion for the useful response of the photometer will be that of $I = I_0/e$ which occurs when $\lambda \simeq 1.2d$.

APPENDIX C

TURBULENCE FROM INTERNAL GRAVITY WAVES

Hodges (1970) concluded from his paper (Hodges, 1969) that the amplitude required for gravity waves to create super-adiabatic instabilities, was of a magnitude where significant non-linearities were not introduced into the wave equation.

Turbulence is generally associated with a Richardson's number less than a critical value, this number for the maintainance of turbulence generally being estimated to be about 0.25 (Tennekes and Lumley, 1972, p. 97). Richardson's number R_i is defined as

$$R_i = \frac{\omega_b^2}{(du/dz)^2} \qquad C.1$$

where $\frac{du}{dz}$ is the vertical gradient of the horizontal wind, and ω_b is the buoyancy frequency which can be written in the form

$$\omega_b^2 = \frac{(\gamma-1)^2 g}{c^2} + \frac{g}{c^2}\frac{dc^2}{dz} \qquad C.2$$

where $\frac{dc}{dz}$ is the vertical gradient of the speed of sound and using $c^2 = \frac{\gamma p}{\rho}$ where p is the pressure and ρ the density, equation C.2 becomes

$$\frac{dc^2}{dz} = \frac{\gamma}{\rho}\frac{dp}{dz} - \frac{c^2}{\rho}\frac{d\rho}{dz} . \qquad C.3$$

Small gravity wave induced perturbations p' and ρ' in the pressure p and density ρ such that $p = p_0 + p'$ and $\rho = \rho_0 + \rho'$ where p_0 and ρ_0 are the background values of pressure and density are given by (Yeh and Liu, 1974)

$$p' = \rho' c^2 \alpha, \qquad C.4$$

$$V_x' = \frac{\rho' \alpha k_x c^2}{\rho_0 \omega} \qquad C.5$$

where

$$\alpha = \frac{\omega^2 - \omega_b^2}{\omega^2 - \frac{g(\gamma-1)}{H} + ig(\gamma-1)k_z}$$

and V_x' is the value of the horizontal wind introduced by the gravity wave. The phase relation between ρ' and p' and V_x' is arg α such that

$$\arg \alpha = \phi = \arctan\left(- \frac{g(\gamma-1)k_z}{\omega^2 - \frac{g(\gamma-1)}{2H}} \right) . \qquad C.7$$

The pressure perturbation ρ' may be written in the form

$$\rho' = |\rho'| e^{i\theta} \qquad C.8$$

where θ varies as time and p' will be related to ρ' by the relation

$$p' = |\rho'| c^2 |\alpha| e^{i(\theta+\phi)} . \qquad C.9$$

Therefore the real parts of ρ', p' may be expressed as $|\rho'|$ cos θ and $|\rho'| c^2 |\alpha|$ cos$(\theta+\phi)$ respectively.

The real part of V_x' may be expressed in a similar fashion.

Using the differential $\frac{\partial}{\partial z} = \frac{1}{2H} - ik_z$ for gravity waves and the real parts of ρ', p' and V_x', a localized Richardson's number induced by gravity waves becomes

$$R_i = \frac{\frac{(\gamma-1)g^2}{c^2} + g\left|\frac{\rho'}{\rho_0}\right| \left(\frac{1}{2H} - ik_z\right) \left(\gamma|\alpha|\cos(\theta+\phi) - \cos\theta\right)}{\left(\left|\frac{\rho'}{\rho_0}\right| \frac{|\alpha| k_x c^2}{\omega} \left(\frac{1}{2H} - ik_z\right) \cos(\theta+\phi)\right)^2} \qquad C.10$$

where $\left|\frac{\rho'}{\rho_0}\right|$ is the amplitude of the density fluctuation. The amplitude of $\left|\frac{\rho'}{\rho_0}\right|$ grows as the wave propagates upwards until a situation is reached where for some θ, Ri is less than some critical Richardsons number Ri_0.

Calculations indicate that for Ri = ¼, $\left|\frac{\rho'}{\rho_0}\right| \gtrsim 0.2$ for all θ and all frequencies except for small and large values of K_z.

Zimmerman et al (1972) have found using rocket borne pitot tubes and chemical puff releases over the altitude interval 85 km to 125 km that turbulence occurs for measured Richardson's numbers up to 10. For Ri = 10, $\left|\frac{\rho'}{\rho_0}\right| \lesssim 0.2$ for all θ and frequencies other than $\omega_b > \omega > 1.15\ \omega_b$.

There is therefore some justification for predicting that gravity waves will initiate turbulence when $\left|\frac{\rho'}{\rho_0}\right| \lesssim 0.2$. Equation C.10 does not predict turbulence for $\left|\frac{\rho'}{\rho_0}\right| \lesssim 0.2$ if turbulence only occurs when Ri $\lesssim$ ¼. However equation C.10 fails to take into account non-linear terms. If turbulence occurs for values of Ri up to 10 as Zimmerman suggests then equation C.10 predicts that turbulence will be produced by waves in which $\left|\frac{\rho'}{\rho_0}\right| \lesssim 0.2$. However the degree of turbulence especially when ¼ < Ri < 10 may not be severe enough to attenuate the wave sufficiently to produce a wave of constant amplitude.

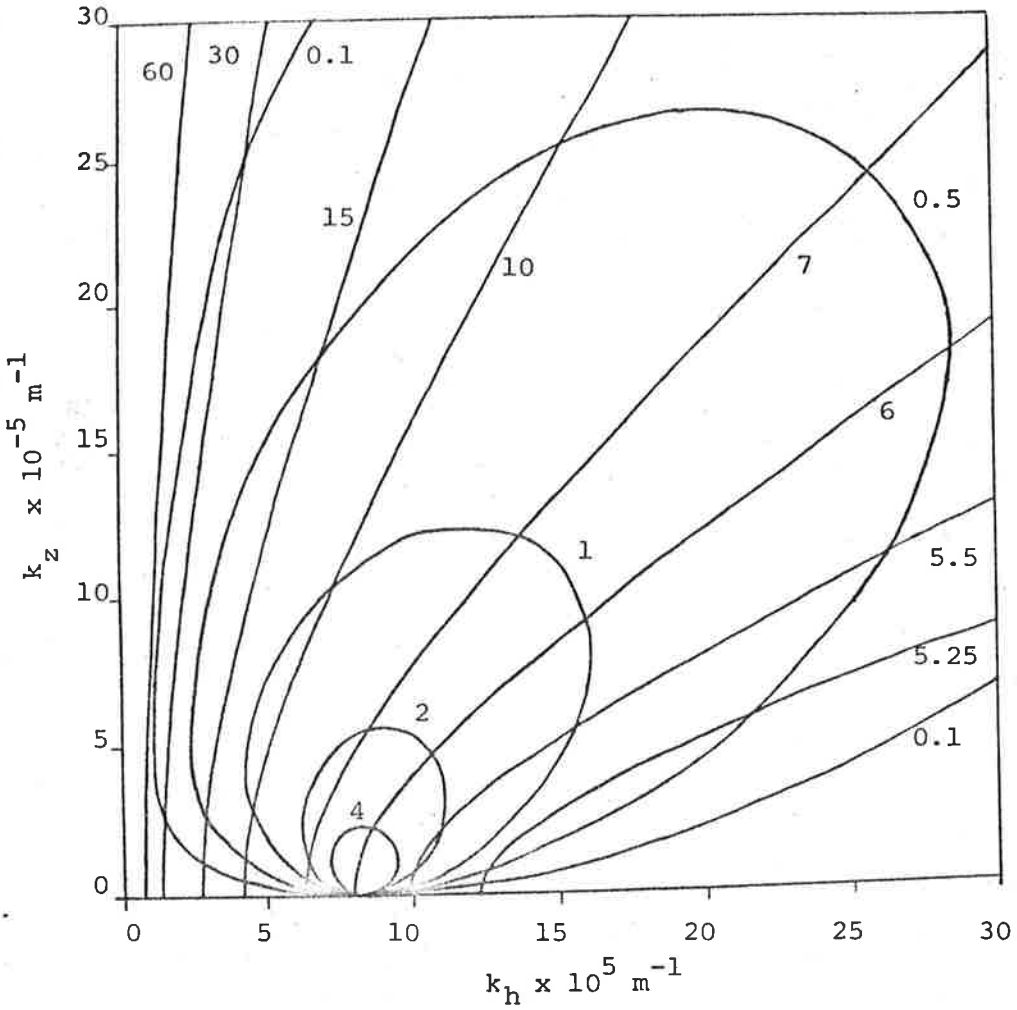

Figure D.1 Plot of the dispersion surfaces of internal gravity waves at 96 km for different periods (in minutes) and contours of the energy dissipation rate (in $W\text{-}m^{-3}$ x 10^7) for a constant amplitude wave at a relative density amplitude of 1%. The hyperbolic curves represent the dispersion surfaces.

APPENDIX D

ENERGY DISSIPATION RATE AND THE KINEMATIC VISCOSITY IN A ZERO AMPLITUDE GROWTH WAVE

This appendix enlarges on aspects of a zero-growth wave previously discussed in Section 5.2.4 and a technique will be outlined to calculate the energy dissipation rate at various amplitudes in a zero-growth wave and the value of the eddy kinematic viscosity required to produce an energy dissipation rate which will maintain the wave at a constant amplitude. These will only be average values throughout the wave whereas as noted in Section 5.2.4, instabilities with associated turbulence, where the energy dissipation rate and the eddy viscosity value would be large, would occur at localized regions within the wave.

The energy dissipation rate W for a constant amplitude wave can be calculated using the equation

$$W = \frac{\Gamma_z}{H} \qquad \text{D.1}$$

where Γ_z is the energy flux, H is the scale height. In equation (5.9), Γ_z is provided as a function of density and therefore it is possible to calculate the dissipation rate at any amplitude of zero growth or constant amplitude wave.

Dispersion surfaces calculated using (Hines, 1960),

$$k_h^2\left(1 - \frac{\omega_b^2}{\omega^2}\right) + k_z^2 = k_0^2\left(1 - \frac{\omega_a^2}{\omega^2}\right) \qquad \text{D.2}$$

have been plotted in Figure D.1 using a model atmosphere (CIRA, 1965) for various periods and also contours of the energy dissipation rate of constant amplitude waves at a relative density amplitude of 1% have been mapped.

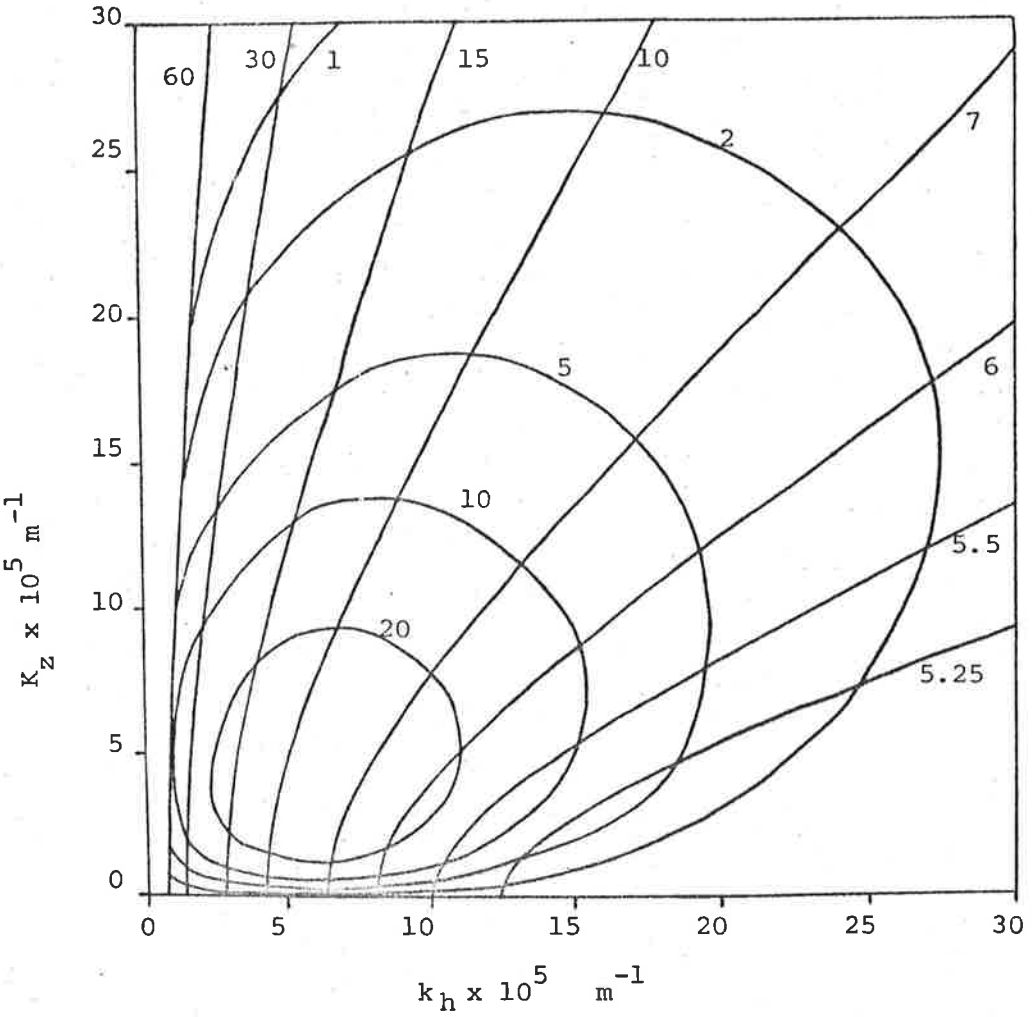

Figure D.2. Plot of the dispersion surfaces of internal gravity waves at 96 km for different periods (in minutes) and contours of constant kinematic viscosity (in $m^2\text{-}sec^{-1} \times 10^{-4}$) associated with a wave of constant amplitude. The hyperbolic curves represent the dispersion surfaces.

Equations (5.11) and (5.12) allow one to write k_z'' in the form

$$k_z'' = \nu\left(f_1(\omega,k)+f_2(\omega,k)\right) \qquad \text{D.3}$$

where $f_1(\omega,k)$ and $f_2(\omega,k)$ may be deduced from equations (46) and (47) of Yeh and Liu (1974). Therefore it is possible to calculate the kinematic viscosity which is associated with a wave having an attenuation rate k_z''. In Figure D.2 as in Figure D.1 dispersion surfaces have been plotted and also contours of kinematic viscosity produced by a constant amplitude wave where $k_z'' = -\frac{1}{2H}$ have been mapped.

APPENDIX E

GRAVITY WAVE TRANSMISSION

This appendix is referred to in Section 5.3.1 and will be concerned with the determination of the transmission of a gravity wave through a horizontal stratified atmosphere with respect to wind and temperature. McKenzie (1972) has calculated the reflection and transmission coefficients of a wave at a boundary where there are temperature, wind and density discontinuities. Hines and Reddy (1967) used a multilayer approach where the vertical temperature and horizontal wind profiles remained unchanged in a given layer and were discontinuous at the boundary between adjacent layers with the amplitudes of the upgoing and downgoing wave in adjacent layers being compared. The present approach will follow the concept of Hines and Reddy (1967) using the reflection coefficients of McKenzie (1972). The density will be assumed to vary in a continuous fashion within a layer and also to be continuous at boundaries between layers.

As is shown in Figure E.1a, $A_m^{(i)}$ is the amplitude of the incident upward directed wave at a discontinuity separating layers m and m+1, and $A_m^{(r)}$ and $A_{m+1}^{(t)}$ are the amplitudes of the reflected and transmitted components respectively. They are related to $A_m^{(i)}$ by the following relationships

$$A_m^{(r)} = R_u A_m^{(i)} \text{ and } A_{m+1}^{(t)} = \frac{\omega_{m+1}}{\omega_m}\left(1+R_u\right) \qquad \text{E.1a}$$

where R_u is the reflection coefficient of an upwardly directed wave of the particular discontinuity and ω_m, ω_{m+1} are the respective wave frequencies in the adjacent layers. In Figure E.1b the transmitted

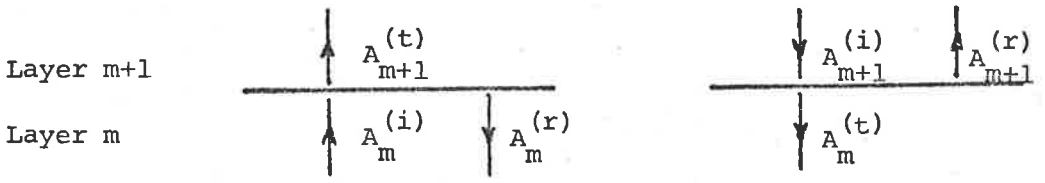

Figures E.1 a & b $A_m^{(i)}$ is the amplitude of an upgoing wave incident at a boundary with $A_{m+1}^{(t)}$ and $A_m^{(r)}$ its transmitted and reflected components. $A_{m+1}^{(i)}$ is a downgoing wave incident at a boundary with $A_m^{(t)}$ and $A_{m+1}^{(r)}$ its transmitted and reflected components.

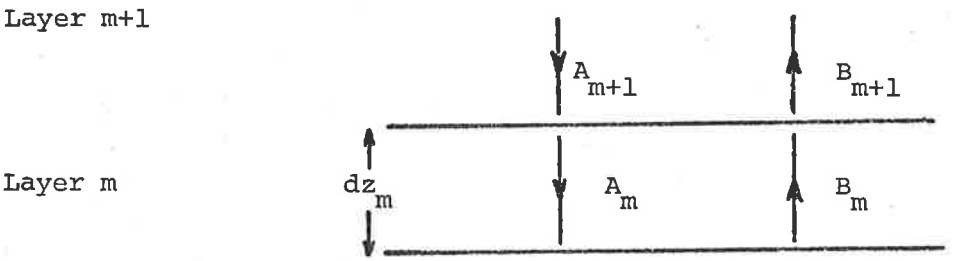

Figure E.1c B_m, B_{m+1} are the amplitudes of the upgoing waves in adjacent layers and A_m, A_{m+1} are the amplitudes of the downgoing waves. The thickness of the layer m is dz_m.

amplitude $A_m^{(t)}$ and the reflected amplitude $A_{m+1}^{(r)}$ are related to a downgoing incident amplitude $A_{m+1}^{(i)}$ by

$$A_{m+1}^{(r)} = R_d A_{m+1}^{(i)} \text{ and } A_m^{(t)} = \frac{\omega_m}{\omega_{m+1}} (1+R_d) A_{m+1}^{(i)} \qquad \text{E.2}$$

where R_d is the reflection coefficient of a downwardly directed wave at the discontinuity.

Referring to Figure E.1c, in which A_m and B_m are the respective downgoing and upgoing amplitudes of the wave in the m-layer and A_{m+1} and B_{m+1} are the corresponding amplitudes in the m+1 layer, quantities α_m and α_{m+1} may be defined as follows

$$\alpha_m = \frac{B_m}{A_m} \text{ and } \alpha_{m+1} = \frac{B_{m+1}}{A_{m+1}} . \qquad \text{E.3}$$

Then it follows on combining equations E.1, E.2, and E.3 that

$$A_{m+1} = R_d B_{m+1} + \frac{\omega_{m+1}}{\omega_m} (1+R_u) A_m , \qquad \text{E.4}$$

$$B_m = R_u A_m + \frac{\omega_{m+1}}{\omega_m} (1+R_u) A_m . \qquad \text{E.5}$$

On eliminating A_{m+1}, B_{m+1},

$$\alpha_m = \frac{B_m}{A_m} = e^{i2k_{zm}d_m} \left(R_u + \frac{(1+R_d)(1+R_u)\alpha_{m+1}}{1-\alpha_{m+1}R_d} \right) \qquad \text{E.6}$$

where α_m is now, by the introduction of the exponential term, the amplitude ratio at the bottom of the m-layer, the layer having thickness d_m and the wave having a vertical wave-number k_{zm} within the layer. Setting $\alpha = 0$ at the highest level one can iterate down through a number of thin layers to a lower level. The transmission coefficient T through a series of layers is given by

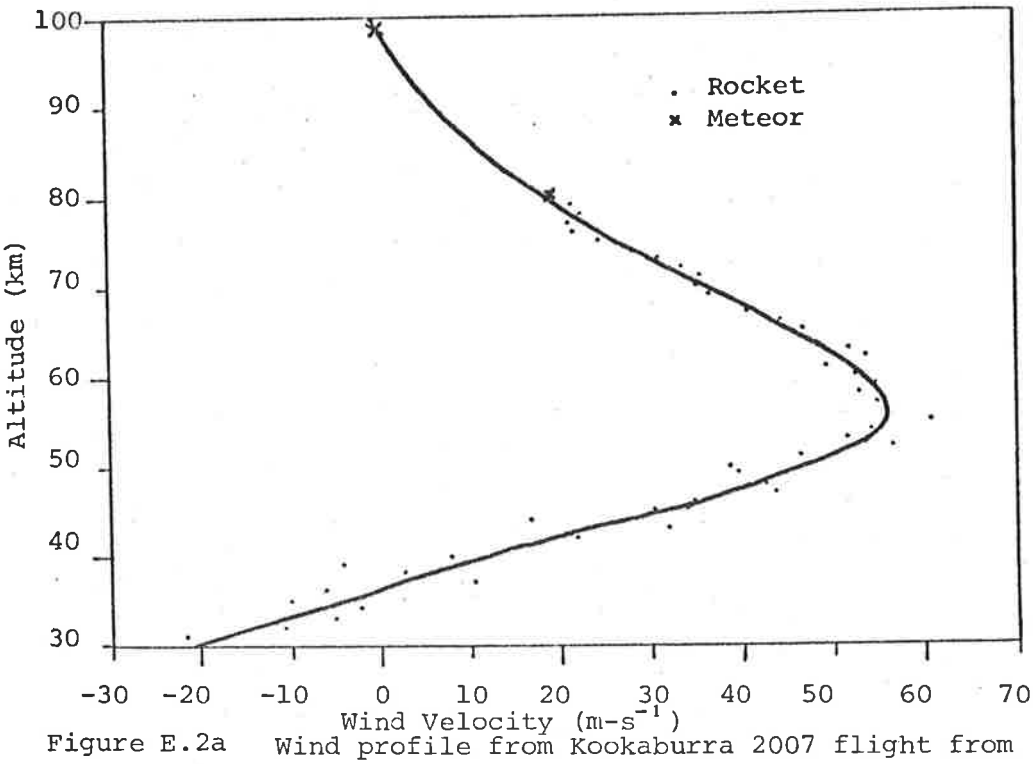

Figure E.2a Wind profile from Kookaburra 2007 flight from Woomara on 19 September 1973 at 09.17 UT (30km to 80km) and Adelaide Meteor Wind Data (80 km to 100 km)

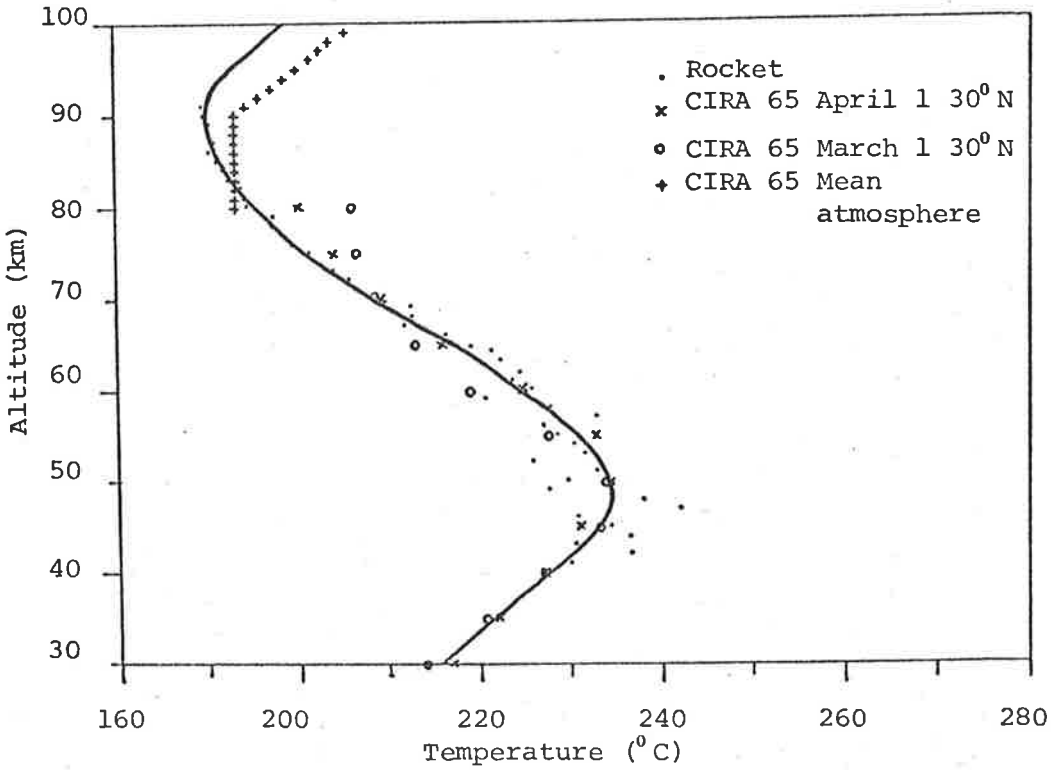

Figure E.2b Temperature profile from Kookaburra 2007 flight from Woomera on 19 September 1973 at 09.17UT and from CIRA 65 Model Atmosphere.

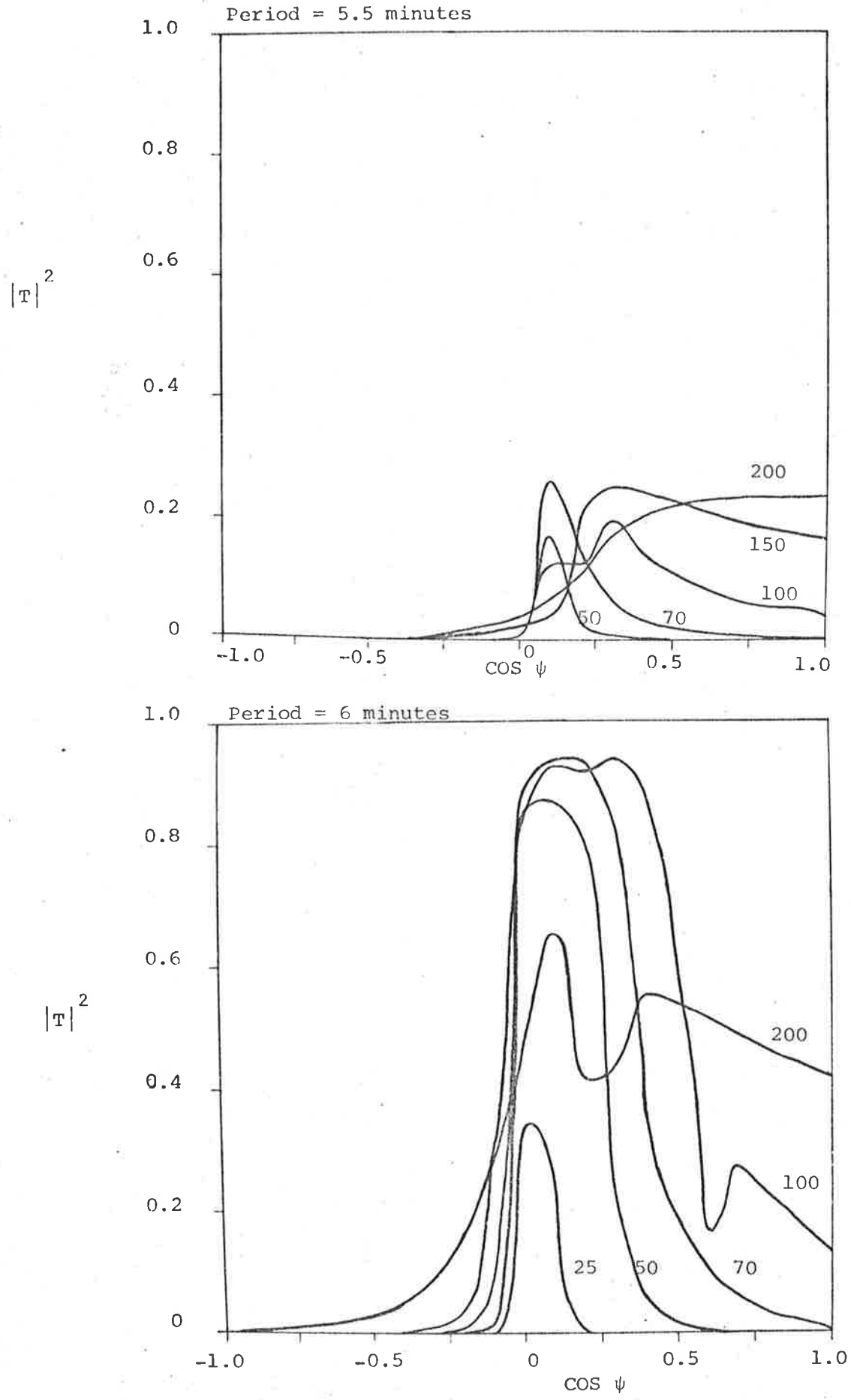

Figures E.3a (top) and E.3b Plots of transmission coefficients through layer 20 km to 95 km for various horizontal phase velocities (in m. s^{-1}) and periods.

$$T = 1 - |\alpha_0|^2 \qquad \text{E.7}$$

where α_0 is the amplitude ratio in the lowest layer.

With the density continuous at the interface, the reflection coefficient R is given by (McKenzie, 1972)

$$R = \frac{\left(\omega_1 p^{(i)} - ig\right) - \left(\omega_2 p^{(t)} - ig\right)}{-\left(\omega_1 p^{(r)} - ig\right) + \left(\omega_2 p^{(t)} - ig\right)} \qquad \text{E.8}$$

where

$$p = \frac{\omega^2 - \omega_b^2}{\omega\left(k_z + i\omega_a(\gamma - Z)/\gamma C\right)} \qquad \text{E.9}$$

with ω_1 and ω_2 being the respective frequencies of the incident and transmitted waves. The frequency in an adjacent layer is determined using the Galilean transformation given in equation (5.7). The layer thickness is set using the criterion (Vincent, 1969) that the thickness is less than 1/10th the vertical wave length.

Transmission coefficients have been calculated using a wind and temperature profile obtained from a falling sphere experiment conducted at Woomera on 19 September, 1973 at 0917 UT. Data from a model atmosphere (CIRA, 1965) has been used to extend continuity of these profiles from 20 km to 100 km and these appear in Figure E.2. Transmission coefficients of waves through the atmospheric layer of 20 km to 95 km have been plotted in Figure E.3 for periods (in a stationary frame) of 5.5, 6, 7.5 and 30 minutes and horizontal phase velocities of 25, 50, 70, 100 and 200 $m\text{-}s^{-1}$. The angle between the horizontal wave number which by Snell's Law is invariant in a horizontally stratified atmosphere and an eastward wind is represented by ψ. Attenuation due to viscous damping and heat conduction has been included through the imaginary component of the vertical wave number using the expression of equation (5.11). The kinematic viscosity has been set to a constant 100 $m^2\text{-}sec^{-1}$. Webb (1972)

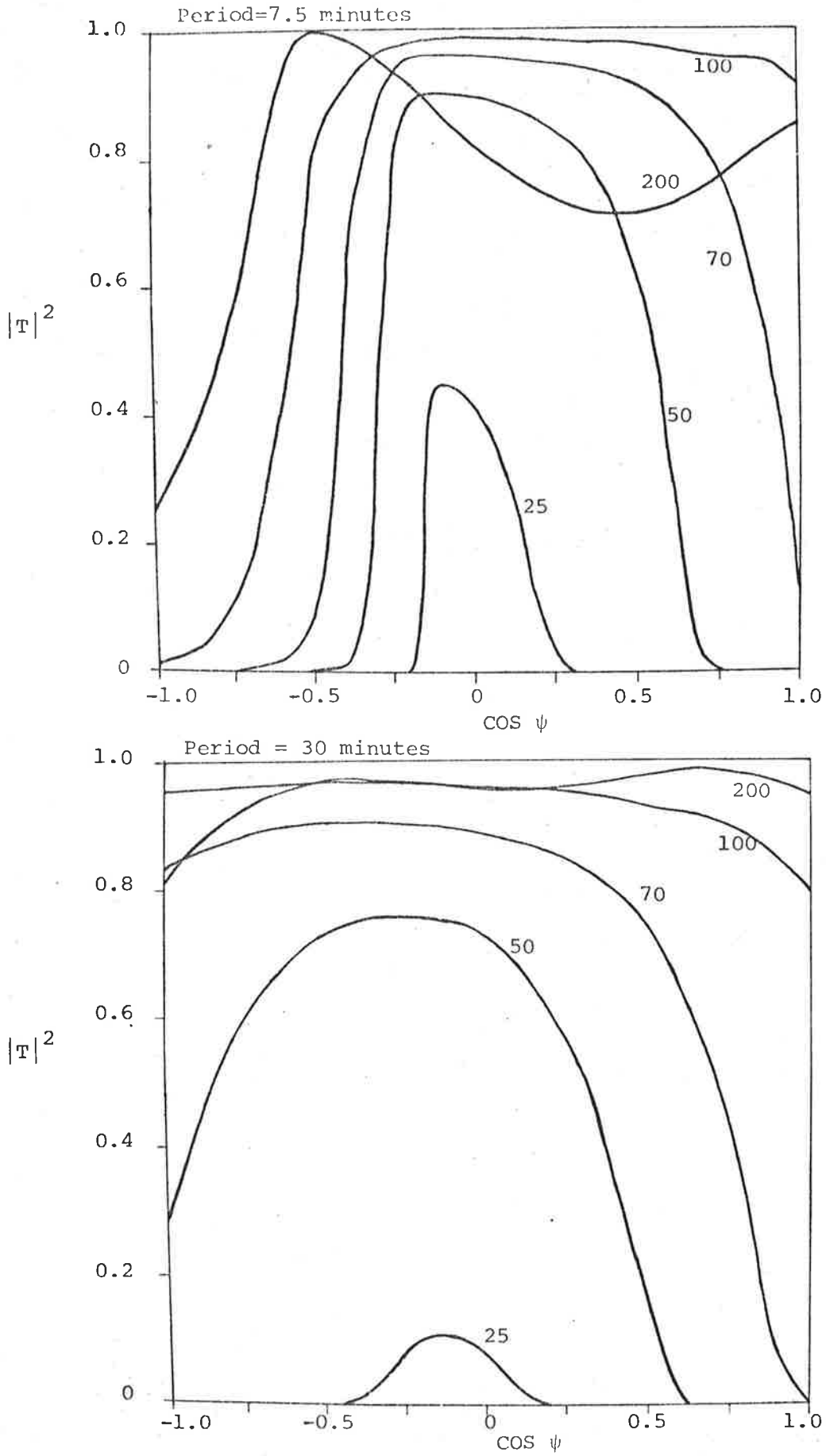

Figures E.3c (top) and E.3d Plots of transmission coefficients through layer 20 km to 95 km for various horizontal phase velocities (in $m\text{-}s^{-2}$) and periods.

has estimated that eddy transport coefficient will be somewhat greater for heights greater than 50 km and less for heights below this.

Hines and Reddy (1967) showed that a wave is not transmitted through a region where it has its frequency doppler shifted to zero. As can be demonstrated in equation (5.6) this occurs when the component of the wind in the direction of the horizontal wave number is equal to the horizontal phase velocity. On inclusion of the dissipation term, the transmission is neglible when the wind component is greater than 0.6 of the horizontal phase velocity.

BIBLIOGRAPHY

Armstrong, E.B., Variations in the width of the OI λ 557.7 line in the night airglow, *Planet Space Sci.*, 16, 211, 1968.

Baltanar, E. and Pardo, G., Observation on airglow green cells, *Ann. Geophys.*, 28, 731, 1972.

Barat, J., Blamont, J.-E., Petitdidier, M., Sidi, C., and Teitelbaum, H., Mise en evidence experimentale d'une structure inhomogene a petite echelle dans la couche emissive de l'oxygene atomique a 557.7 Å, *Ann. Geophys.*, 28, 145, 1972.

Barth, C.A. und Hildebrandt, A.F., The 557.7 Å airglow emission mechanism, *J. Geophys. Res.*, 66, 985, 1961.

Briggs, B.H., On the analysis of moving patterns in geophysics, *J. Atmos. Teor. Phys.*, 30, 1777, 1968.

Bevington, P.R., *Data reduction and error analysis for the physical sciences* (McGraw Hill, 1969).

Buckley, R., *Some notes on practical digital power spectra, auto- and cross correlations using the Fast Fourier Transform* (University of Adelaide, Department of Physics, October 1971, Internal Publication).

Chamberlain, J.W., *Physics of the Aurora and Airglow* (Academic Press, 1961).

Chiplonka, M.W. and Tillu, A.D., The F-layer component of the 5577 Å emission of the nightglow at Poona, *Ann. Geophys.*, 26, 213, 1970.

Cowling, D.H., Webb, H.D. and Yeh, K.C., Group rays of internal gravity waves in a wind-stratisfied atmosphere, *J. Geophys. Res.*, 76, 213, 1971.

Cutrona, L.T., Recent developments in coherent optical technology. *Optical and Electro-optical Information Processing*, edited by J.T. Tippet et al., MIT press, 1965.

Danekar, B.S., Study of the [OI] green line at Mount Abu, *J. Atmos. Terr. Phys.*, 27, 245, 1965.

Donahue, T.M., Guenther, B. and Thomas, R.J., Distribution of atomic oxygen in the upper atmosphere deduced from Ogo 6 airglow observations, *J. Geophys. Res.*, 78, 6662, 1973.

Eather, R.H. and Reasoner, D.L., Spectrophotometry of faint light sources with a tilting filter photometer, *Applied Optics*, 8, 227, 1969.

Fedor, L.S. and Plywaski, W., The interpretation of ionispheric radio drift measurements. IV. The effect of signal coupling among spaced sensor channels, *J. Atmos. Terr. Phys.*, 34, 1285, 1972.

Fooks, G.F., Ionispheric drift measurements using correlation analysis; method of computation and interpretation of results, *J. Atmos. Terr. Phys.*, 27, 979, 1965.

Garstang, R.H., Energy levels and transition probabilities in P^2 and P^4 configurations, *Mon. Notic. Roy. Astron. Soc.*, 111, 115, 1951.

Golley, M.G. and Rossiter, D.E., Some tests of methods of analysis of ionispheric drift records using an array of 89 aerials, *J. Atmos. Terr. Phys.*, 32, 1215, 1970.

Henriksen, K., The excitation of the oxygen green line in the night glow and aurora, *Physica Norwegica*, 17, 57, 1973.

Hinder, G.W. and Iredale, P., The image quality of an image intensifier expressed in terms of its equivalent quantum efficiency, *Adv. Elect. & Elect. Phys.*, 29B, 639, 1972.

Hines, C.O., Internal atmospheric gravity waves at ionispheric heights, *Can. J. Phys.*, 38, 1441, 1960.

Hines, C.O., *Physics of the Earth's Upper Atmosphere*, edited by C.O. Hines, I. Peghis, T.R. Hartz, J.A. Tejer (Prentice-Hall, 1965).

Hines, C.O. and Reddy, C.A., On the propagation of atmospheric gravity waves through regions of wind shear, *J. Geophys. Res.*, 72, 1015, 1967.

Hines, C.O., A possible source of waves in noctilucent clouds, *J. Atmos. Sci.* 25, 937, 1967.

Hines, C.O., Eddy diffusion coefficients due to instabilities in internal gravity waves, *J. Geophys. Res.*, 75, 3937, 1970.

Hines, C.O., Propagation velocities and speeds in ionispheric waves; A review, *J. Atmos. Terr. Phys.*, 36, 1179, 1974.

Hodges Jr., R.R., Eddy diffusion coefficients due to instabilities in internal gravity waves, *J. Geophys. Res.*, 74, 4087, 1969.

Hodges Jr., R.R., Eddy diffusion coefficients due to instabilities in internal gravity waves, *J. Geophys. Res.*, 74, 4087, 1970.

Hunich, M.J. and Clay, C.S., The application of the discrete Fourier Transform in the estimation of power spectra, coherence and bispectra of geophysical data, *Rev. Geophys.*, 6, 34, 1968.

Iredale, P. and Ryden, D.J., On the quality of photographic images recorded with the use of image intensifiers, *Adv. Elect. & Elect. Phys.*, 28B, 965, 1969.

Jacchia, L.G., Revised static models of the thermosphere and exosphere with empirical temperature profiles, *Spec. Rep.* 332, Smithsonian Austrophys. Obs., Cambridge, Mass., 1971.

Jordan, A.R., Atmospheric gravity waves from winds and storms, *J. Atmos. Sci.*, 29, 445, 1972.

Korobeynikova, M.P. and Nasinov, G.A., Research of the emission at 5577 Å in the period of 1958-1967 in Ashkhabad, *Ann. Geophys.*, 28, 483, 1972.

McGee, J.D., *Photo electronic Imaging Devices*, edited by Biberman, Nudelman (N.Y., Academic Press, 1972).

McKenzie, J.F., Reflection and amplification of acoustic-gravity waves at a density and velocity discontinuity, *J. Geophys. Res.*, 77, 2915, 1972.

Offerman, D. and Drescher, A., Atomic oxygen densities in the lower thermosphere as derived from in situ 5577-Å night airglow and mass spectrometer measurements, *J. Geophys. Res.*, 78, 6690, 1973.

Roach, F.E., Tandberg-Hanssen, E. and Megill, L.R., The characteristic size of airglow cells, *J. Atmos. Terr. Phys.*, 13, 113, 1958.

Roach, F.E. and Smith, L.L., *Aurora and Airglow*, edited by B.M. McCormac, p. 29, Reinhold Publ. Co., New York, 1967.

Roper, R.G. and Elford, W.G., Seasonal variation of turbulence in the upper atmosphere, *Nature*, 197, 963, 1963.

Roper, R.G. Atmospheric turbulence in the meteor region, *J. Geophys. Res.*, 71, 5785, 1966.

Schaeffer, R.K., PhD thesis (University of Adelaide, 1970).

Schiff, H.I., Neutral reactions involving oxygen and nitrogen, *Can. J. Chem.*, 47, 1903, 1969.

Sears, R.D., Versatile family of modern aurora and airglow photometers, *App. Optics*, 12, 1349, 1973.

Sears, R.D. and Evans, J.E., A photometric technique for detecting upper atmosphere winds and wave-like motions, *Am. Geophys. Un.*, 55, 684, 1974.

Slanger, T.G. and Black, G., O(1S) quenching profile between 75 and 115 km, *Planet Space Sci.*, 21, 1757, 1973.

Stubbs, T.J., The measurement of winds in the D-region of the ionisphere, *J. Atmos. Terr. Phys.*, 35, 909, 1973.

Tennekes, H. and Lumley, J.L., *A First Course in Turbulence* (MIT Press, 1972).

Vincent, R.A., A criterion for the use of the multilayer approximation in the study of acoustic-gravity wave propagation, *J. Geophys. Res.*, 74, 2996, 1969.

Vincent, R.A., Ionispheric irregularities in the E-region, *J. Atmos. Terr. Phys.*, 34, 1881, 1972.

Wilksch, P. and Bower, A., Private Communication.

Yeh, K.C. and Liu, C.H., Acoustic-gravity waves in the upper atmosphere, *Rev. Geophys. Space Phys.*, 12, 193, 1974.

Zimmerman, S.P. and Rosenberg, N.W., Wind energy deposition in the upper atmosphere, *Space Res.*, 12, 623, 1972.

Zimmerman, S.P., Meteor trails and atmospheric turbulence, *J. Geophys. Res.*, 78, 3927, 1973.

Zimmerman, S.P., Addendum and correction to parameters of turbulent atmospheres, *J. Geophys. Res.*, 72, 5153, 1967.

ADDENDUM

CHAPTER 6

CONCLUSIONS AND SUGGESTIONS FOR FURTHER WORK

6.1 Introduction

The thesis can be roughly divided into the following sections - instrumentation, methods of analysis of results, the results and immediate conclusions which may be drawn from these results and finally a study of the propagation in and the effects of gravity waves on the atmosphere. The structure of this conclusion will be based on the above divisions.

6.2.1 Image-intensifier system

Although a program of observations was carried out using the image intensifier-film system, the "sky pictures" obtained did not yield significant results. However it is shown in Chapter 2 that useful results (e.g. which will provide the spatial spectral distribution of low amplitude gravity waves) may be obtained if a satisfactory data recording device which spatially detects and records photons is used. Photographic film will perform this function although it is difficult to efficiently retrieve the stored information.

6.2.2 4-field of view photometer

The 4-field photometer proved adequate although there is considerable scope for improvement in any future photometer. Primarily the photometer should be designed to ensure that the angle of incidence of the central ray from each field of view is normal to the interference filter. Rotating or tilting the filter synchronously with moving the field stop, using a rotating prism in front of the objective or using separate filters are

obvious solutions. Equations A.14 and A.15 indicate the relation between the photon counting rate, the standard deviation in the lag time observed at the two fields of view and aspects of the airglow pattern, e.g. period and the relative intensity variation, and should be used as a guide in designing future photometers.

6.3 Methods of analysis

Of the methods of estimating the velocity of pattern movement, the "similar fades" method and the dispersion analysis method appear to compliment each other with the "similar fades" method offering good time resolution and the second method indicating the variation of velocities with frequency. However only the velocities calculated using the "similar fades" method are reported in this thesis. Spectral analysis carried out included the mapping of spectral power with time (c.f. Spectrograms in Figures 5.1 to 5.3) and also searching for the presence of longer period waves (c.f. Table 5.1) using date continuous over at least several hours. At least the above four methods of analysis should be used in conjunction with the observation program.

6.4 Direct conclusions from 557.7 nm results

The results as presented in Chapters 4 and 5 are all highly suggestive that a major portion of the intensity structure in the 557.7 nm airglow is produced by gravity waves. This statement is supported by the following evidence. The sinusoidal nature of the intensity variations extending over a number of cycles (Figures 4.2a to 4.6a), adjacent wave-type structures propogating in different directions (Figure 4.3a), the lack of correlation between the background wind and the drift (or apparent) velocities (Figures 4.9 and 4.10) and the anisoropy of the velocities (Figure 4.13). Also, although not reported earlier in the thesis, the full correlation analysis

which produces the "true" velocity was used in conjunction with the "similar fades" method, but did not, in many instances, provide meaningful results. (By comparing the velocities obtained using the above two methods with the velocity obtained by finding the time lag between dientical features at the different fields of view, it was assessed that "true" velocity underestimated the velocity by a greater degree than the drift (or apparent) velocity may have overestimated the velocity.) Therefore it is likely that differences in the intensity pattern as observed from the different fields is not, in the main, due to random changes and therefore these differences may have resulted from wave patterns travelling in different directions. The basic assumption in the full correlation analysis is that the changes in the pattern are random.

In frequency cut-off around 4×10^{-3} Hz and the spectral peaks are also indicative of the presence of gravity waves. From Table 4.1, the spectral power variation with frequency over certain frequency ranges varies approximately as f^{-2} which is a characteristic of the turbulent energy spectrum (equation 5.2). However this f^{-2} variation occurs near the buoyancy frequency $(4 \times 10^{-3}$ Hz) and therefore may also be a characteristic of a gravity wave spectrum.

With respect to the nature of the 557.7 nm intensity variations, there is considerable scope for future work. This includes further substantiating the presence of gravity waves, looking for other causes which effect the intensity such as turbulence and accoustic waves. This work could only be carried out adequately using a photometer with an improved S/N ratio. Also it would be desirable to discover under what circumstances the type of variations observed on 29 November 1973 occur.